JOURNAL OF POWDER MATERIALS

Volume 31, Number 3 JUNE 2024

Special Articles: Papers in Subdivision of Materials Modeling/Artificial Intelligence/Advanced Characterization

Research Articles

kpmi
Korean Powder Metallurgy & Materials Institute

사단법인 한국분말재료학회
Unit 706, (635-4, Yeoksam-Dong)22, 7Gil, Teheran-Ro, Gangnam-Gu, 06130, Seoul, Korea
TEL + 82-2-539-4603 FAX + 82-0303-0947-4603
Homepage : http://www.kpmi.or.kr e-mail :kpmi@kpmi.or.kr

02
9 772799 852009
ISSN 2799-8525

Journal of Powder Materials
VOL. 31 NO. 3 / June 2024
Page 213-291
kpmi

ISSN 2799-8525 (Print)
ISSN 2799-8681 (Online)

한국분말재료학회지
Journal of Powder Materials

VOL. 31 NO. 3 / June 2024 Page 213-291

kpmi
Korean Powder Metallurgy & Materials Institute

Journal of Powder Materials

ISSN 2799-8525 (Print)
ISSN 2799-8681 (Online)

VOL. 31 NO. 3 (Total 164) / June 2024

Aims and Scope

Journal of Powder Materials is the official journal of The Korean Powder Metallurgy & Materials Institute (KPMI). Journal of Powder Materials publishes original articles, and reviews concerned with all aspects of powder metallurgy.
Journal of Powder Materials covers the whole fields of powder materials and processes, which includes powder production (including their precursor materials), milling, granulation, cold and hot compaction, sintering, cold and hot isostatic pressing, pulsed and other assisted consolidation, additive manufacturing, injection molding, as well as coating technology using powder. The characterization, testing, quality assurance and applications are also covered.
Journal of Powder Materials by bridging the gap between pure research and the more practical aspects of production and properties, will continue to provide a unifying medium for material scientists, technologists, engineers, designers and manufacturers.

ISO abbreviation of journal title

✓ Topic

Powder Materials
- Fe-based powders
- Non-ferrous powders
- Ceramic powders
- Particulate Composite
- Tool/Cemented Carbides
- Porous powders
- Electric/Electronic powders
- Bio materials
- Magnetic powders
- Energy conversion/storage powders
- Multi-functional powders
- Organic/inorganic powders

Powder Technology
- Powder synthesis
- Powder characterization/analysis
- Powder compaction
- Powder pretreatment
- Sintering
- Densification process
- PIM
- Post-treatment
- Novel powder technology
- Nanostructured powders
- Simulation of powder/process
- Powder test
- Powder business/industry

The official title of the journal is 'Journal of Powder Materials' and the abbreviated title is 'J. Powder Mater.'.

Year of launching (history)

Journal of Powder Materials was launched in 1993.

The frequency of publication

Journal of Powder Materials is published bi-monthly in February, April, June, August, October, and December. Supplementary issues are also published at times.

Availability of the full-text in the web, URL address

The published articles from the initial to the present issue are available free of charge at http://ejournal.kpmi.or.kr.

Index in database

The articles published in Journal of Powder Materials are indexed and/or abstracted in Google Scholar, KISTI, and KCI.

Fund support

"본 사업은 기획재정부의 복권기금 및 과학기술정보통신부의 과학기술진흥기금으로 추진하여 사회적 가치 실현과 국가 과학기술 발전에 기여합니다."
"This work was supported by the Korean Federation of Science and Technology Societies(KOFST) grant funded by the Korean government."

Subscription info

The annual subscription fee for this journal is Korean Won ₩50,000 (US$ 50.00 or equivalent). Back issues are available on request. The number of circulated print copies is 600. Full published papers from the initial to the present issue are available free of charge at http://ejournal.kpmi.or.kr. Correspondence concerning business matters should be addressed to Ms. Youn-Ho Kim, Manager, The Korean Powder Metallurgy & Materials Institute, Unit 706, (635-4, Yeoksam-Dong) 22, 7Gil, Teheran-Ro, Gangnam-Gu, Seoul 06130, Korea (Tel: +82-2-539-4603, Fax: +82-0303-0947-4603, e-mail: kpmi@kpmi.or.kr).

kpmi
Korean Powder Metallurgy & Materials Institute

Submission
Manuscripts should be submitted via the online Manuscript Central website (https://submit.powdermat.org). Other correspondence can be sent by e-mail (ktkim@kims.re.kr or kpmi@kpmi.or.kr) to the Editor-in-Chief, Dr. Kyung Tae Kim, Korea Institute of Materials Science, Changwon, Gyeongnam 51508, Korea. All manuscripts are peer-reviewed.

Contact info (Editorial office)
The Korean Powder Metallurgy & Materials Institute Unit 706, 22, 7Gil, Teheran-Ro, Gangnam-Gu, Seoul 06130, Korea
Tel: +82-2-539-4603, Fax: +82-0303-0947-4603, E-mail: kpmi@kpmi.or.kr

Printed by M2PI
#805, 26 Sangwon 1-gil, Seongdong-gu, Seoul 04779, Korea
Tel: +82-2-6966-4930, Fax: +82-2-6966-4945, E-mail: support@m2-pi.com, Homepage: http://m2-pi.com

Editorial Board

Journal of Powder Materials

Contents

Journal of Powder Materials

VOL. 31 NO.3 / June 2024

Special Articles: Papers in Subdivision of Materials Modeling/Artificial Intelligence/Advanced Characterization

Research Articles

Contents

Journal of Powder Materials

VOL. 31 NO.3 / June 2024

Special Articles: Papers in Subdivision of Materials Modeling/Artificial Intelligence/Advanced Characterization

Research Articles

Special Article

pISSN 2799-8525 · eISSN 2799-8681
J Powder Mater 2024;31(3):213-219

Journal of Powder Materials

Trends in Materials Modeling and Computation for Metal Additive Manufacturing

Seoyeon Jeon, Hyunjoo Choi*

School of Materials Science and Engineering, Kookmin University, Seoul 02707, Republic of Korea

Additive Manufacturing (AM) is a process that fabricates products by manufacturing materials according to a three-dimensional model. It has recently gained attention due to its environmental advantages, including reduced energy consumption and high material utilization rates. However, controlling defects such as melting issues and residual stress, which can occur during metal additive manufacturing, poses a challenge. The trial-and-error verification of these defects is both time-consuming and costly. Consequently, efforts have been made to develop phenomenological models that understand the influence of process variables on defects, and mechanical/ electrical/thermal properties of geometrically complex products. This paper introduces modeling techniques that can simulate the powder additive manufacturing process. The focus is on representative metal additive manufacturing processes such as Powder Bed Fusion (PBF), Direct Energy Deposition (DED), and Binder Jetting (BJ) method. To calculate thermal-stress history and the resulting deformations, modeling techniques based on Finite Element Method (FEM) are generally utilized. For simulating the movements and packing behavior of powders during powder classification, modeling techniques based on Discrete Element Method (DEM) are employed. Additionally, to simulate sintering and microstructural changes, techniques such as Monte Carlo (MC), Molecular Dynamics (MD), and Phase Field Modeling (PFM) are predominantly used.

Keywords: Metal; Additive manufacturing; Computation; Modeling; Trends

Received: June 11, 2024
Revised: June 18, 2024
Accepted: June 20, 2024

***Corresponding author:**
Hyunjoo Choi
TEL: +82-2-910-4287
FAX: +82-2-910-4320
E-mail: hyunjoo@kookmin.ac.kr

1. Introduction

Additive Manufacturing (AM) is a process that fabricates products by manufacturing materials in accordance with a three-dimensional model, enabling the creation of complex three-dimensional shapes that are impossible to achieve with traditional solidification or machining methods. As a result, multiple parts can be consolidated into a single complex component, significantly reducing the number of parts used and the manufacturing processes involved. Furthermore, AM allows for the intricate and precise construction of heterogeneous materials and the flexible creation of composite or hybrid structured materials, facilitating product and business innovation. In addition, compared to traditional metal processing methods, AM can contribute to carbon neutrality by reducing energy consumption and CO_2 emissions and promoting the recycling of waste materials. It represents a manufacturing process innovation by enabling the production of finished products in a single step without the need for the fabrication and assembly of numerous parts. This capability affords self-sufficiency in the production, repair, and reuse of parts, even in challenging environments such as outer space, polar regions, or remote areas where the distribution and assembly of parts are difficult [1, 2]. Due to these remarkable advantages that were previously unimaginable using conventional processes, AM is hailed as a revolution in the manufacturing industry. It is being explored for various applications, including the medical field [3], aerospace components [4], and more.

Additive Manufacturing (AM) is widely utilized across various material fields, including polymers [5-7], ceramics [8], metals [9-11], and composites [12, 13]. As shown in Fig. 1(a), the Precedence research predicts that the global market size of metal additive manufacturing will continue to expand. Corre-

https://doi.org/10.4150/jpm.2024.00150

spondingly, as depicted in Fig. 1(b), the number of research articles on metal additive manufacturing has also been increasing year by year. (The data for 2024 is collected as of May 2024, showing fewer numbers compared to 2022.) This aggregates the number of papers from 2015 to 2024 on ScienceDirect (Keyword: Metal additive manufacturing).

According to ASTM F2792-12a by the American Society for Testing and Materials (ASTM), terms previously known as RP or rapid prototyping technologies have been standardized to 3D printing or additive manufacturing technologies. They classified the manufacturing methods into the following seven categories: Material Extrusion (ME), Material Jetting (MJ), Binder Jetting (BJ), Sheet Lamination (SHL), Vat Photo Polymerization (VPP), Powder Bed Fusion (PBF), and Direct Energy Deposition (DED) [14-18].

In metal additive manufacturing, various defects can occur that distort the shape and degrade the quality of the product, such as melting defects, porosity, and residual stress [19]. These defects can be minimized by controlling various experimental factors such as the type and power of the heat source, scan speed and pattern, hatch spacing, and solidification and cooling conditions [20-22]. Currently, to fabricate additive manufacturing products that are free of defects, structurally robust, and reliable, different process conditions are validated through experimental trial and error, which is time-consuming and costly. Therefore, over the past two decades, efforts have been made to develop phenomenological models that quantitatively understand the influence of process variables on defects, distortions, residual stresses, microstructures, and mechanical/electrical/thermal properties of geometrically complex products. By understanding the metallurgical correlation between alloy elements, processes, microstructures, and properties, it is possible to design process variables that achieve the desired properties. Additionally, computer modeling plays a crucial role in additive manufacturing compared to other manufacturing processes because it allows for the rapid optimization of process parameters, considering both productivity (layering speed and product size) and technical compatibility (residual stress and deformation).

Therefore, this paper aims to introduce various modeling techniques that can simulate the powder additive manufacturing process for prominent metal additive manufacturing methods such as Powder Bed Fusion (PBF) and Direct Energy Deposition (DED), as well as the increasingly popular Binder Jetting (BJ).

2. Result

2.1. Modeling of Beam-Based Metal Additive Manufacturing

As shown in Fig. 2, PBF and DED are representative additive manufacturing processes used in metal additive manufacturing [20]. The Powder Bed Fusion (PBF) method involves spreading thin layers of metal powder, typically tens of micrometers thick, across a powder bed using a powder delivery system. A heat source then selectively fuses the powder according to the design, layer by layer. On the other hand, the Direct Energy Deposition (DED) method employs a heat source to create a molten pool on a metal substrate into which metal powder is fed. The heat source and the powder delivery nozzle move together following the design to build the 3D structure in this manner.

Both PBF and DED can be further classified based on the type of heat source used, such as Laser Beam (L), Electron Beam (EB), Gas Tungsten Arc (GTA), Plasma Arc (PA), and

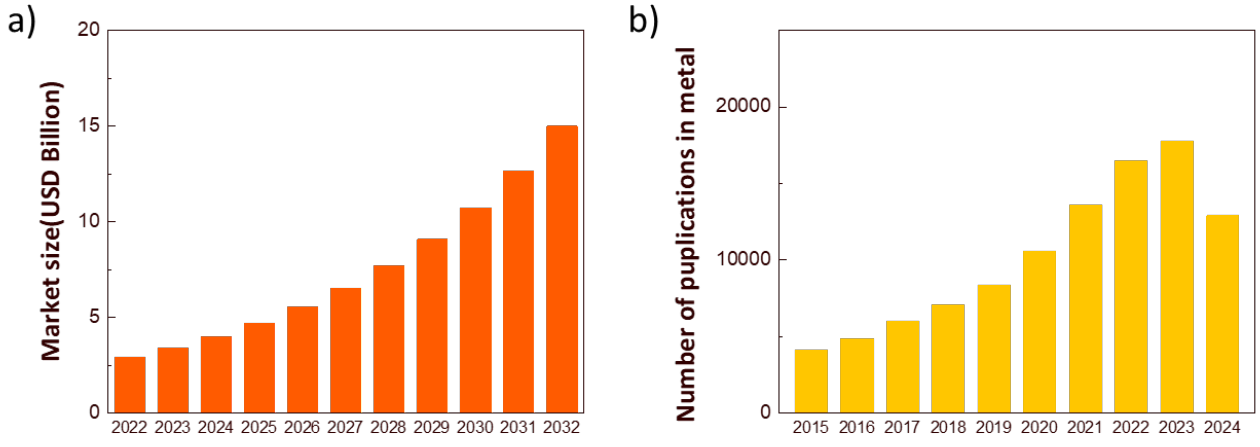

Fig. 1. (a) Market share of materials used in additive manufacturing and (b) the number of research papers on metal additive manufacturing.

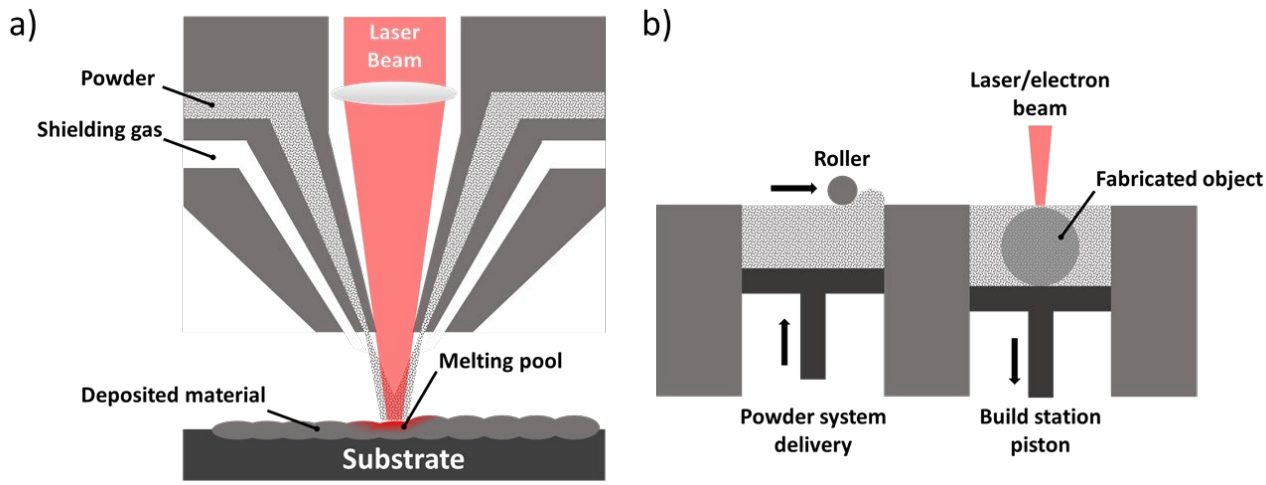

Fig. 2. Schematic illustrations of (a) direct energy deposition (DED) and (b) powder bed fusion (PBF).

Gas Metal Arc (GMA). In the PBF process, only powder can be used as the feedstock, whereas in the DED process, both powder and wire can be used. In beam-based metal additive manufacturing, various complex physical phenomena occur simultaneously, including heat absorption and transfer, molten pool formation, and solidification in the deposited material and substrate. To understand the correlations between the process, microstructure, and properties during these stages, various modeling techniques have been developed.

2.1.1. Modeling of Material Classification Process

Rain-drop modeling and Discrete Element Method (DEM) are representative modeling techniques used to simulate the classification process of powder materials. The Rain-drop model disregards the individual distribution process of particles and focuses solely on predicting the packing density of particles [21]. This method is primarily used in the PBF process to calculate the packing density of the powder bed [22]. In this model, the first contact of each particle is calculated following the selection of each particle's random horizontal position, then the particle is rotated in the direction that minimizes potential energy to compute the next contact point. Through this series of steps, the packing density of the powder in the powder bed can be calculated. However, the Rain-drop model has limitations in simulating the flow issues of powders and the pore structures formed within the powder layer during the powder classification process. Therefore, DEM is increasingly being applied instead of Rain-drop modeling for the modeling of material classification processes.

As shown in Fig. 3, DEM, first developed by Cundall and

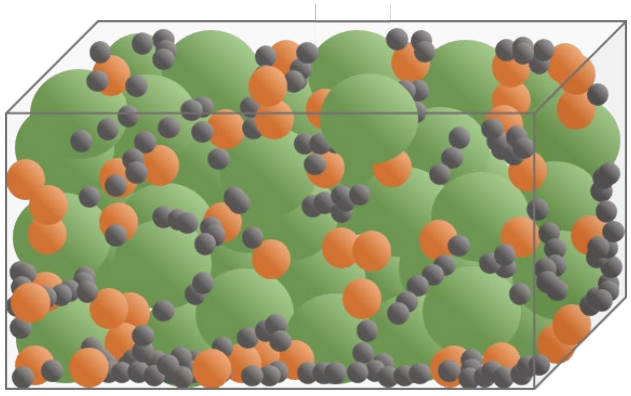

Fig. 3. Schematic illustration of discrete element method (DEM) simulation of particles mixing.

Strack [23], is a numerical analysis technique that mechanically calculates and simulates the motion and collision of particles to model particle and granular flow. Unlike the Finite Element Method (FEM), which assumes the entire system as a continuum and derives integral solutions for continuous equations, DEM treats individual elements as discrete entities. It calculates the forces exerted on each particle at each time step under the assumption that interactions between particles occur independently, allowing for the tracking of the motion of all individual particles that make up the granular system.

In DEM, contact forces based on contact mechanics are key elements in the interactions between particles. The time response history and energy loss of particle material are determined by the time integration of these contact forces. Contact force models generally employ a combination of the nonlinear

Hertz model and Mindlin's shear model, or simplified models in the form of linear springs. With DEM modeling, it is possible to analyze the impact of various process parameters, particle-particle interactions, particle size, and shape on the spatial distribution of the powder bed (e.g., bed porosity, thickness, and surface roughness) during the powder classification process.

2.1.2. Modeling of Thermal Stress

To manufacture integrated products from classified powders, the powder goes through processes of heating, melting, solidification, and cooling. To quantitatively calculate deformations and potential failures in the product during this series of steps, it is essential to model the regional thermal stress history. Given the similarities between the heating, melting, and solidification processes in additive manufacturing and traditional welding processes, modeling techniques used for welding processes are often extended or adapted for additive manufacturing simulations. In beam-based metal additive manufacturing, modeling deformation and failure due to thermal stress entails linking multidimensional modeling results, ranging from macro-level elements corresponding to the heat source and components to nano- and micro-level elements representing the microstructure. This holistic integration is a significant challenge in accurately capturing the effects of thermal stress on deformation and damage in the additive manufacturing process.

2.1.2.1. Mathematical Modeling of Heat Source

To quantitatively simulate the heat distribution within a material due to the heat source in metal additive manufacturing using a beam, accurate calculations for heat transfer considering the component's shape and material properties are crucial. Typically, in mathematical modeling of heat distribution from the heat source, the heat source is categorized as a point, line, area, or volumetric source. Point and line heat sources are often handled using the analytical solution of heat conduction equations, while area and volumetric heat sources require numerical modeling for heat transfer and fluid flow simulations.

Laser beams, electron beams, and arcs are generally assumed to be point heat sources. By knowing the material's thermal diffusivity and the distance from the heat source, the temperature at each point can be calculated using the Rosenthal solution [24]. However, these models typically consider only conduction and disregard convective heat transfer, leading to limitations in predicting excessive temperature gradients and cooling speeds. They also do not account for fluid flow changes due to reactions between the molten pool's surface and active elements like sulfur and oxygen.

In cases where heat transfer is dominant in one direction, extending the point-shaped heat transfer equations to line-shaped heat sources can be beneficial. Situations where a keyhole defect is formed, typically under high-power-density heat sources, can benefit from this extended line-shaped heat transfer modeling over point sources [25-27]. Energy density gradients in the diameter direction of the heat source are often assumed to follow a Gaussian distribution. In processes like Powder Bed Fusion (PBF), where the beam can penetrate deeply into the powder bed due to multiple reflections or in Directed Energy Deposition (DED) where preheating can occur along the beam path, three-dimensional volumetric heat source assumptions can be utilized for precise calculations.

Recently, the Double Ellipsoidal Model [28] has been used to simultaneously account for conduction and convection, allowing for swift calculations while approximating the energy density distribution based on experimental melt pool shapes as double ellipsoids.

2.1.2.2 Modeling of heat absorption

The amount of heat absorbed in metal layer manufacturing is influenced by various factors such as the type of heat source (laser, electron beam, arc, etc.), the type and shape of materials (powder, wire, etc.). In the case of DED, since the powder deposition and heat source irradiation occur simultaneously, the powder absorbs heat while moving from the nozzle to the substrate, with 15-20% of the heat source energy being lost during this process [29]. The amount of energy absorbed by the heat source in the process of forming a molten pool after the powder is deposited on the substrate varies depending on the type and energy of the heat source, surface roughness and reflectivity of the material, local temperature of the material, and the size of the molten pool [29]. In the case of PBF, the energy absorption rate can increase due to multiple reflections within the Powder Bed, which is influenced by the beam's irradiation angle, powder size distribution and packing density, and reflectivity [30].

2.1.2.3 Modeling of heat transfer and fluid flow

In metal layer manufacturing, heat transfer and fluid flow can be calculated based on equations related to mass, momentum, and energy conservation. The driving forces that induce fluid flow in the molten pool in this context include: i) Marangoni Force (fluid movement in the molten pool in the tangential direction of the surface due to surface tension gradients caused by temperature gradients), ii) Lorentz (Electromagnetic)

Force (movement of fluid by electromagnetic forces when using an arc or electron beam as the heat source), iii) Droplet/Powder Impact Force (force generated when sprayed powder in DED collides with the molten pool), iv) Buoyancy Force, v) Recoil Force (force driving the movement of molten metal downwards due to evaporation of alloying elements) [31]. To calculate the flow of heat and fluid during the metal layer manufacturing process, it is necessary to define the shape changes of the molten pool over time so that boundary conditions for heat and fluid transfer can be defined. Additionally, the temperature gradient on the surface of the molten pool calculated using the methods described in Sections 2.1.2.1 and 2.1.2.2 can be input as boundary conditions for heat and fluid flow during the manufacturing process, along with various driving forces for fluid flow as described above. By defining the shape of the molten pool (Fig. 4), inputting boundary conditions, and providing material information (thermal conductivity, specific heat, density, latent heat, viscosity, solidus and liquidus temperatures, etc.), the behavior of heat and fluid can be predicted as a function of time and space through finite element-based modeling.

2.1.3. Modeling of microstructure

To simulate changes in microstructure during metal layer manufacturing processes, phase field modeling (PFM), Monte Carlo (MC), and Cellular Automata (CA) are commonly used. Among these, MC and CA are suitable for modeling mesoscale microstructures, such as the sizes and aspect ratios of multiple crystallites formed after layering, while PFM is suited for modeling microscale microstructures like solute atom concentrations, precipitates, and grain boundaries. To integrate the results of macro-scale thermal-stress modeling mentioned in Section 2.1.2 with microstructure modeling, two main methods are typically employed: i) performing thermal-stress modeling first and using the results as input parameters for microstructure modeling, and ii) concurrently conducting thermal-stress modeling and microstructure modeling with mutual information exchange. The latter method provides more precise computational results but comes with limitations of high computational time and cost [32].

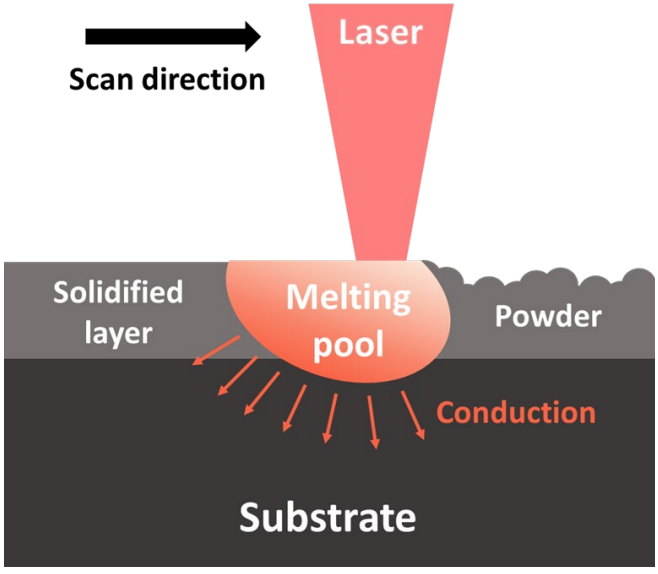

Fig. 4. Schematic illustration of melting pool phenomena in PBF process.

2.2. Modeling of metal layer manufacturing without a beam

Binder Jetting (BJ) is a representative process for metal layer manufacturing without a beam, where significant research has been conducted recently [33, 34]. In BJ, powder is selectively sprayed and manufactured by mixing it with a binder, followed by sintering to produce the final product. This section aims to introduce modeling techniques for calculating the shape and characteristics of products manufactured using this process.

2.2.1. Powder Behavior Modeling

In the BJ layering process, freshly deposited powder in the Powder Bed is spread out into a single layer by a roller or blade-type spreader. The interaction between the powder and spreader, as well as inter-particle interactions, are key factors determining powder movement, often modeled using Discrete Element Method (DEM). A DEM calculates the dynamics of particle motion and collisions and mechanically simulates the flow of particles and powder, tracking the motion of individual particles by calculating the contact forces acting on them at each time interval. This allows for the analysis of various process parameters (spreading speed, spreader shape) and interactions between powder particles, as well as powder size and shape, affecting the spatial distribution of the Powder Bed (porosity, thickness, surface roughness, etc.) during powder spreading and deposition. Generally, computational results show that larger roller diameters and thinner powder layers induce higher powder compaction by applying greater pressure to the powder. It has also been discovered that slower spreading speeds can induce higher powder compaction with roller-type spreaders compared to blade-type spreaders [35, 36].

2.2.2. Modeling of powder-binder interaction

As shown in Fig. 5, in Binder Jetting (BJ), after a layer of

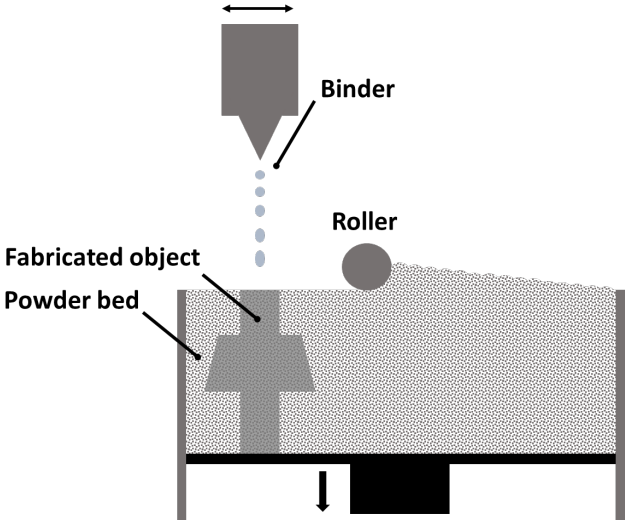

Fig. 5. Schematic illustration of binder jetting (BJ) printer.

powder is deposited, the binder is sprayed onto the desired locations. The sprayed binder collides rapidly with the powder and deeply penetrates into the Powder Bed, transferring its kinetic energy to the powder and causing rearrangement. The interactions between the binder and powder (liquid-solid interaction) and between powder particles (solid-solid interaction) need to be simultaneously calculated. Typically, to calculate interactions between liquid and solid, methods include calculating surface tension and equilibrium forces based on differences in wettability between liquid (binder) - solid (powder) - gas (air) interfaces (Static Modeling), as well as considering changes in binder shape, flow upon contact with the powder surface along with changes in wettability and surface tension (Dynamic Modeling). Several numerical methods are used to simulate powder-binder interactions and resulting powder movements, but due to the complexity associated with various physical phenomena involved, achieving accurate modeling remains challenging with current technology [37, 38].

The process of pore removal among powders and their coalescence during sintering, primarily driven by solid-state diffusion, is usually modeled using methods such as Monte Carlo (MC) or Molecular Dynamics (MD) [39, 40]. Recently, there has been progress in simulating sintering at the microscale using Phase Field Modeling (PFM) [41]. In PFM, a series of continuous field functions are employed to describe the microstructure, with each function representing specific physical quantities related to the microstructure (e.g., phase, chemical composition, crystal orientation). These functions calculate the evolution of microstructure over time and space based on the total free energy of the system, following Cahn-Hilliard or Allen-Cahn equations.

3. Conclusion

So far, various research trends in modeling techniques for simulating metal layer manufacturing processes have been introduced. Metal layer manufacturing is rapidly expanding in the market due to advantages like design freedom, high efficiency, and the possibility of producing complex-shaped products. To design optimal layering processes for different materials, various macroscopic and microscopic modeling techniques capable of simulating various physical phenomena have been proposed. Generally, Finite Element Method (FEM)-based modeling techniques are utilized to calculate thermal-stress history and resulting deformations. Discrete Element Method (DEM) modeling is used to simulate powder movement during deposition, while techniques like Monte Carlo (MC), Molecular Dynamics (MD), and Phase Field Modeling (PFM) are primarily employed to model sintering and microstructural changes. Up to now, research has mainly focused on steel-based materials, and there is a need for modeling technique studies that can be applied to a variety of metal materials. Additionally, real-time (in situ) analysis methods to validate the accuracy of models should be developed. Furthermore, research on multidimensional modeling techniques that can simultaneously calculate multidimensional physical phenomena from component-level to microstructure-level at a rapid pace is essential.

Conflict of Interest

H.Choi serves as an editor of the Science editing, but has no role in the decision to publish this article. Except for that, no potential conflict of interest relevant to this article was reported.

Author Information and Contribution

Seoyeon Jeon: MS/ Writing, Hyunjoo Choi: Professor/Supervision, review and editing.

Acknowledgments

This study was financially supported by the National Re-

search Foundation of Korea (NRF) grant funded by the Korean government (MSIP) (No. NRF-2022R1A5A1030054).

References

[1] H. Lipson and M Kurman, Indianapolis, Indiana: John Wiley and Sons, Inc, (2013)

[2] A. Bandyopadhyay, K. D. Traxel, M. Lang, M. Juhasz, N. Eliaz, and S. Bose: Mater. Today., **52** (2022) 207.

[3] J. Giannatisis and V. Dedoussis: Int. J. Adv. Manuf. Technol., **40** (2009) 116.

[4] S. C. Altiparmak, V. A. Yardley, Z. Shi, and J. Lin: Int. J. Lightweight Mater. Manuf., **4** (2021) 246.

[5] S. Wickramasinghe, T. Do, and P. Tran: Polymers., **12** (2020) 1529.

[6] K. Chatterjee and T. K. Ghosh: Ghosh., **32** (2020) 1902086.

[7] D. M. Nieto, V. C López, and S. I. Molina: Addit. Manuf., **23** (2018) 79.

[8] C. L. Cramer, E. Ionescu, M. G. Zajac, A. T. Nelson, Y. Katoh, J. J. Haslam, L. Wondraczek, T. G. Aguirre, S. Leblanc, H. Wang, M. Masoudi, E. Tegeler, R. Riedel, P. Colombo, and M. M. Joladan: J. Eur. Ceram. Soc., **42** (2022) 3049.

[9] S. Jeon, S Park, Y Song, J Park, H Park, B Lee, and H Choi: J. Powder Mater., **30** (2023) 463.

[10] S. Park, Y. Song, J. Yeo, S. Han, and H. Choi: J. Powder Mater., **30** (2023) 255.

[11] Y. Li and Q. Bai: Chin. J. Mech. Eng., **30** (2017) 515.

[12] W. S. Cai, H. Z. Lu, H. Z. Li, Z. Liu, H. B. Ke, W. H. Wang, and C. Yang: J. Mater. Sci. Technol., **138** (2023) 80.

[13] M. P. Behera, T. Dougherty, and S. Singamneni: Procedia Manuf., **30** (2019) 159.

[14] B. Kianian, Fort Collins, Colorado, USA: Wohlers Associates, Inc, (2016)

[15] L. Yang, K. Hsu, B. Baughman, D. Godfrey, F. Medina, M. Menon, and S. Wiener, Cham: Springer, (2017) 45.

[16] ASTM, ASTM International. (2012)

[17] J. W. Choi and H. C. Kim: J. Kor. Soc. Manuf. Process Eng., **14** (2015) 1.

[18] I. H. Lee, H. C. Kim, and D. G. Ahn: J. Kor. Soc. Precision Eng., **37** (2015) 929.

[19] T. DebRoy, H. L. Wei, J. S. Zuback, T. Mukherjee, J. W. Elmer, J. O. Milewski, A.M. Beese, A. Wilson-Heid, A. De, W. Zhang, and W. Zhang: Progress in Mater. Sci., **92** (2018) 112.

[20] V. Manvatkar, A. De, and T. DebRoy: J. Appl. Phys., **116** (2014) 124905.

[21] V. Manvatkar, A. De, and T. DebRoy: Mater. Sci. Technol., **31** (2015) 924.

[22] T. Mukherjee, H. L. Wei, A. De, and T. DebRoy: Comput. Mater. Sci., **150** (2018) 369.

[23] C. Körner, E. Attar, and P. Heinl: J. Mater. Process. Technol., **211** (2011) 978.

[24] B. de La Batut, O. Fergani, V. Brotan, M. Bambach, and M. El Mansouri: J. Manuf. Mater. Process., **1** (2017) 3.

[25] P. Burgardt and C. R. Heiple: Heiple: Welding J., **71** 341.

[26] R. T. Brown: J. Laser Appl., **20** (2008) 201.

[27] Y. Javid, M. Ghoreishi, and S. Shamsaei: Lasers in Engineering (Old City Publishing)., **22** (2012) 1.

[28] P. Farahmand and R. Kovacevic: Opt. Laser Technol., **63** (2014) 154.

[29] A. J. Pinkerton and L. Li: J. Eng. Manuf., **218** (2004) 363.

[30] X. Wang, T. Laoi, J. Bonse, J.-P. Kruth, B. Lauwers, and L. Froyen: Int. J. Adv. Manuf. Technol., **19** (2002) 351.

[31] T. DebToy and S. A. David: Rev. Mod. Phys., **67** (1995) 85.

[32] J. H. K. Tan, S. L. Sing, and W. Y. Yeong: Virtural and Physical Prototyping., **15** (2020) 87.

[33] L. Ming, D. Wenchao, A. Elwany, Z. Pei, and C. Ma: Manuf. Sci. Eng., **142** (2020) 090801.

[34] J. A. Gonzalez, J. Mireles, Y. Lin, and R. B Wicker: Ceram. Int., **42** (2016) 10559.

[35] C. Meir, R. Weissbach, J. Winberg, W. A. Wall, and A. J. Hart: J. Mater. Process. Technol., **266** (2019) 484.

[36] G. Miao, W. Du, Z. Pei, and C. Ma: Int. Manuf. Sci. Eng. Conf., **1** (2019)

[37] H. Tan: Chem. Eng. Sci., **153** (2016) 93.

[38] M. Uhlmann: J. Comput. Phys., **209** (2005) 448.

[39] L. R. Madhavrao and R. Rafagopalan: J. Mater. Res., **4** (1989) 1251.

[40] K. Mori, H. Matsubara, and N. Noguchi: Int. J. Mechanical Sci., **46** (2004) 841.

[41] W. Boettinger, J. Warren, C. Beckermann, and A. Karma: Annu. Rev. Mater., **32** (2002) 163.

Special Article

pISSN 2799-8525 · eISSN 2799-8681
J Powder Mater 2024;31(3):220-225

Journal of Powder Materials

316H 스테인리스 강 위에 적층 제조된 순수 니켈층의 원소 확산거리 연구

고의준[1], 이원찬[1], 신기승[2], 윤지현[2], 김정한[1,*]

[1]국립한밭대학교 신소재공학과
[2]한국원자력연구원 재료안전기술연구부

Study on the Elemental Diffusion Distance of a Pure Nickel Layer Additively Manufactured on 316H Stainless Steel

UiJun Ko[1], Won Chan Lee[1], Gi Seung Shin[2], Ji-Hyun Yoon[2], Jeoung Han Kim[1,*]

[1]Department of Materials Science & Engineering, Hanbat National University, Daejeon 34158, Republic of Korea
[2]Materials Safety Technology Research Division, Korea Atomic Energy Research Institute, Daejeon 34158, Republic of Korea

Molten salt reactors represent a promising advancement in nuclear technology due to their potential for enhanced safety, higher efficiency, and reduced nuclear waste. However, the development of structural materials that can survive under severe corrosion environments is crucial. In the present work, pure Ni was deposited on the surface of 316H stainless steel using a directed energy deposition (DED) process. This study aimed to fabricate pure Ni alloy layers on an STS316H alloy substrate. It was observed that low laser power during the deposition of pure Ni on the STS316H substrate could induce stacking defects such as surface irregularities and internal voids, which were confirmed through photographic and SEM analyses. Additionally, the diffusion of Fe and Cr elements from the STS316H substrate into the Ni layers was observed to decrease with increasing Ni deposition height. Analysis of the composition of Cr and Fe components within the Ni deposition structures allows for the prediction of properties such as the corrosion resistance of Ni.

Keywords: Molten salt reactor, Nickel, Directed energy deposition, Diffusion length

Received: June 14, 2024
Revised: June 17, 2024
Accepted: June 18, 2024

***Corresponding author:**
Jeoung Han Kim
TEL: +42-821-1240
Email: jh.kim@hanbat.ac.kr

1. Introduction

용융염 원자로(MSR, Molten Salt Reactor)는 핵연료 냉각제로 용융염을 사용하는 소형 원자로로 최근 국내에서도 지속적으로 개발이 이루어지고 있다[1-4]. 일반적인 경수로 방식의 원자로는 분열성 물질을 함유한 핵연료를 핵연료봉과 같은 핵연료 용기에 수용하고 있으며 핵분열로 발생한 열을 경수(물)를 사용하여 터빈으로 전달한다. 이에 반해 MSR은 경수 대신 $MgCl_2$ 또는 FLiNaK와 같은 액체 용융염을 냉각재로 사용한다. MSR 방식의 원자로에서는 중대사고 발생 시 용융염이 누출되더라도 통상적인 대기 환경에서는 금방 굳어버리기 때문에 지하수를 따라 오염수가 퍼지는 등의 2차 피해를 최소화할 수 있다. 따라서, 선진국을 중심으로 MSR 시스템에 대한 활발한 연구가 진행 중에 있다[5]. 이러한 연구개발에서 가장 핵심적인 기술은 부식성이 매우 높은 용융염 환경에서 견딜 수 있는 구조용 재료의 개발이다. 그러나, 현재까지는 600℃ 이상의 용융염 환경에서 내식성을 가지는 구조용 재료의 개발이 매우 어려운 상황이다. 예를 들어, Hastelloy-N은 부식성은 상대적으로 우수하나 중성자 취화가 크기 때문에 원자로에 적용이 어렵다는 문제가 있다[6]. 316H는 크리프 특성이 우수하고 중성자 취소 문제도 덜하지만 용융염 환경에서 내식성이 매우 낮다. 따라서 이에 대한 대안으로 스테인리스강 표면에 용융염 분위기에서 내식성이 우수한 순수 Ni을 클래딩하는 연구가 진행 중에 있다. 순수 니켈은 Fe, Cr 대비 높은 redox potential을 가지고 있어서 용융염 환경에

https://doi.org/10.4150/jpm.2024.00164

서도 비교적 안정적인 것으로 알려져 있다[7, 8]. 또한 순수 Ni은 MSR 열촉매와 반응성이 매우 적어 부식저항성에 대한 관심이 높아지고 있다[9, 10].

한편, Additive Manufacturing (AM) 공정은 금속 3D 적층 제조 기술로 기존에 사용되는 제조방식보다 복잡한 형상의 부품들을 더 정밀하게 제조할 수 있는 장점이 있다[11-15]. 적층 제조 기술 중 금속 소재를 이용하여 적층 제조하는 기술에는 Powder Bed Fusion (PBF) 방식과 Directed Energy Deposition (DED) 방식이 많이 사용되고 있다. PBF 방식은 10~40 마이크로미터 크기의 분말 재료를 분말 베드 위에 일정한 두께로 깔아 선택적으로 레이저를 조사하여 재료를 부분적으로 적층하는 공정이다. 한편, DED 방식의 경우 50~150 마이크로미터 크기의 분말 재료 혹은 wire 형태의 재료를 원료로 사용하며, 보호 가스와 함께 일정하게 주입하여 레이저를 조사하는 방식의 적층 공정이다. PBF 적층 공정의 경우 보다 정밀하고 세밀한 형태의 제품을 제작할 때 유리하지만 특정 형상의 경우 추가적인 지지대를 형성해야 하고 대형 부품을 만들기에 부적합하며 기판이 평면으로 제한된다는 한계가 있다[15]. 이에 반해 DED 적층 공정은 조건에 따라 적층 이후 표면 가공 등의 후처리가 필요하지만 대형 부품을 만들기 유리하며 기존 제품에 다양한 각도에서 금속을 적층할 수 있는 장점이 있다[14]. 그러나, DED를 이용해 표면에 Ni 클래드층을 적층할 경우 스테인리스강 Fe와 Cr 성분이 Ni층으로 확산될 수 있다. Fe와 Cr은 redox potential이 낮아 용융염 환경에서 부식을 초래할 가능성이 높아 통상적으로는 이러한 원소의 비율이 8%를 넘으면 안 되는 것으로 알려져 있다[16].

본 연구에서는 상용 구조재료인 STS316H 금속 기지 위 순수 Ni 분말을 DED 공정으로 적층조형하여 레이저 파워와 스캔 스피드에 따른 STS316H/Ni 계면의 미세조직과 조성 분석을 통해 특성 변화를 연구하였다. 이를 통해 316H 모재의 합금원소가 Ni층으로 확산되는 양을 8% 이하로 제어하고자 하였다.

2. Experimental

본 연구에서는 DED 기반의 금속 적층 조형 장비(장비제조;에이엠솔루션즈, Republic of Korea)로 STS316H 금속 기지 위에 Pure Ni 분말(공급사;Hoganas, Sweden)를 적층 제조 하였다. STS316H 금속 기판과 Pure Ni 분말의 조성은 표1에 나타내었다.

사용한 순수 Ni 분말의 경우 분말 입도 제어를 통해 50-150마이크로미터 크기의 분말을 사용하였다. 적층 조형 시 분말의 공급은 4.5g/min의 조건으로 공급하였으며 운송가스로 High purity Ar gas(5N, 99.999%)를 사용하였다. 분말 운송 가스와 동일한 Ar 가스를 레이저 조사 입구에서 800ml/min으로 melting pool을 보호가스로 분사하였다. 다이오드 레이저를 열원으로 사용하여 총 6개의 시편을 제작하였다. 각 시편제작에 적용된 레이저의 파워와 레이저 스캔 속도, 레이어 두께, 에너지 밀도는 표2에 정리되었다. 적층은 외각(Counter, C)와 내부(Face, F)가 CFCFC 패턴으로 조형되었으며 조형 시 레이저 스캔의 간격은 0.6mm로 설정하였다.

적층 제조가 완료된 시편의 기공과 미세조직 관찰을 위해 JEOL사의 JSM-IT500 장비 주사 전자 현미경을 이용하여 미세 조직 사진을 촬영하였으며 EDS 분석을 통해 시편 단면의 point, map 조성 분석을 진행하였다. 적층 된 시편의 기공률 측정은 Image-J 프로그램을 사용하여 측정하였으며 공정 조건을 기반으로 에너지 밀도(E)를 계산하였다.

$$E=(\alpha \times P)/(v \times h \times t) \quad (1)$$

E는 STS316H 합금 기판에 대한 레이저 에너지 밀도이며 레이저 파워 P와 흡수 계수 α에 정비례하고, 레이저 스캔스피드 v, 레이어 두께 t, 스캔 간격 h에 반비례한다. 다이오드 레이저를 이용한 STS 합금 기판의 흡수계수는 0.35으로 설정하였으며 스캔 간격은 0.6 mm 로 설정하였다.

Table 1. Chemical composition of as-received STS316H metal analyzed by SEM-EDS and inductively coupled plasma-optical emission spectrometer. (Weight %)

Component	Fe	Cr	Ni	Mo	Mn	V
STS316H	Bal.	17.07	10.06	2.16	0.7	0.04
Pure Ni powder	-	-	Bal.	< 0.01	< 0.002	-

Table 2. Summary of directed energy deposition process parameters for each samples

		Laser power (W)	Scan speed (mm/min)	Layer thickness (mm)	Energy Density 10^3 [J/cm^3]
First process	Sample 1	450	500	0.10	31.5
	Sample 2		850	0.08	23.2
	Sample 3	550	500	0.15	25.7
	Sample 4		850	0.10	22.6
Second process	Sample 5	550	750	0.13	19.7
	Sample 6		1000	0.10	19.3

3. Results and Discussion

첫 번째 적층 공정 시 sample #1-4는 2mm 높이로 적층 하였으며, 두 번째 적층 공정 시 sample #5-6은 1mm 높이로 적층 하였다. DED 공정으로 적층 조형한 샘플의 모식도와 거시사진은 그림 1에 나타내었다. Laser power가 비교적 낮은 sample #1과 #2의 경우 상단 표면이 체크무늬를 나타내는 것을 확인할 수 있었으며 이는 적층 조형 시 입열량 부족으로 인해 용융 풀 직경이 레이저 스캔 간격보다 작아 생기는 현상이다. 반면 sample #3과 #4의 경우 적층 상단에 체크무늬가 나타나지 않았으며 마지막 레이어 방향으로 일정한 용융 풀만 나타난 것을 확인하였다(그림 1). DED 적층 조형 시 레이저의 직경은 1 mm로 동일하였으나 sample #1과 #2의 경우 laser power가 낮아 레이저 스캔 간격(0.6mm) 이상으로 용융 풀을 형성하지 못한 것으로 판단된다. 첫 번째 적층 조건에서 낮은 레이저 파워 인가 시 니켈이 고르게 적층 되지 못하였고 이전 레이어의 형상이 그대로 나타나는 문제가 발생하였다. 두 번째 적층 조건은 높은 레이저 파워를 적용하여 적층 하였다. 두 번째 적층 시 550W의 레이저 파워를 인가하여 스캔 스피드 750, 1000mm/min 속도로 인가하였을 때 표면 형상은 안정적인 것을 확인하였다(그림 1).

첫 번째 Ni 적층 제조 시 레이저 파워가 낮은 적층 조건에서는 체크무늬 형상의 표면 적층 결함이 발견되는 것을 확인하였으며 이를 토대로 550W의 레이저 파워를 적용하고 레이저 스캔 스피드를 달리하여 두 번째 적층 제조를 진행하였다. 두 번째 적층 제조 시 sample #5와 #6은 sample #3과 #4와 같이 체크무늬 표면 결함이 발견되지 않았으며 균일한 표면 형상이 관찰되었다.

적층 시편의 단면 분석 결과 sample #1과 #2는 불완전 용융풀 생성으로 인한 Lack of fusion 형상의 기공이 확인이 되었으며 거시 사진에서 확인할 수 있는 체크무늬 형상의 적층 결함이 단면에서도 크랙 형태로 나타나는 것을 확인하였다(그림 2). Image J 프로그램을 사용하여 기공을 제외한 면밀도를 계산하였을 때 sample #1과 #2는 순서대로 99.8%, 99.5%의 면밀도를 갖는 것을 확인하였다. 반면 sample #3와 #4의 경우 단면 형상이 균일한 것으로 관찰되었으며 내부 기공이 관찰되지 않았다.

낮은 입열량 조건에서 합금 분말의 불완전 용융으로 인한 Lack of fusion, 체크 무늬 표면 결함은 레이저 파워가 450W인 sample #1과 #2에서 확인되었으며 계산된 에너지 밀도와 일치하지 않는 결과 값을 보여준다. 이는 레이어 두께로 계산된 에너지 밀도의 영향보다 낮은 에너지 인가로 인한 용융 풀의 크기 차이가 내부 결함의 큰 영향을 끼치는 것으로 판단된다.

표면이 균질하고 내부 기공이 관찰되지 않은 sample #3-6의 조성 맵핑 결과는 그림 3에 나타내었다. STS316H 기판에서의 주요 조성 성분인 Fe, Cr, Ni을 Mapping data로 나타내었으며 이에 기판에서 Ni 적층 조형체 방향으로 확산되어진 Fe과 Cr이 관찰되었다. Sample #3-6은 순서대로 550W의 레이저파워, 500, 850, 750, 1000mm/min의 레이저 스캔 속도로 적층 조형되었다. STS316H 합금 위에 Ni을 적층 조형 하였을 때 Fe 와 Cr 은 모두 Ni 적층 방향으로 확산이 이루어지며 레이저 조사 시 용융 풀을 형성하는 DED 적층 제조 공정 시 발생할 수 있는 한계로 판단된다.

적층 방향으로의 STS316H 원소 확산을 확인하기 위하여 적층 높이(거리)에 따른 Ni, Cr 그리고 Fe 원소의 point 조성 분석 그래프를 그림 4에 나타내었다. 적층 용융풀의 생성위치로부터 Fe 와

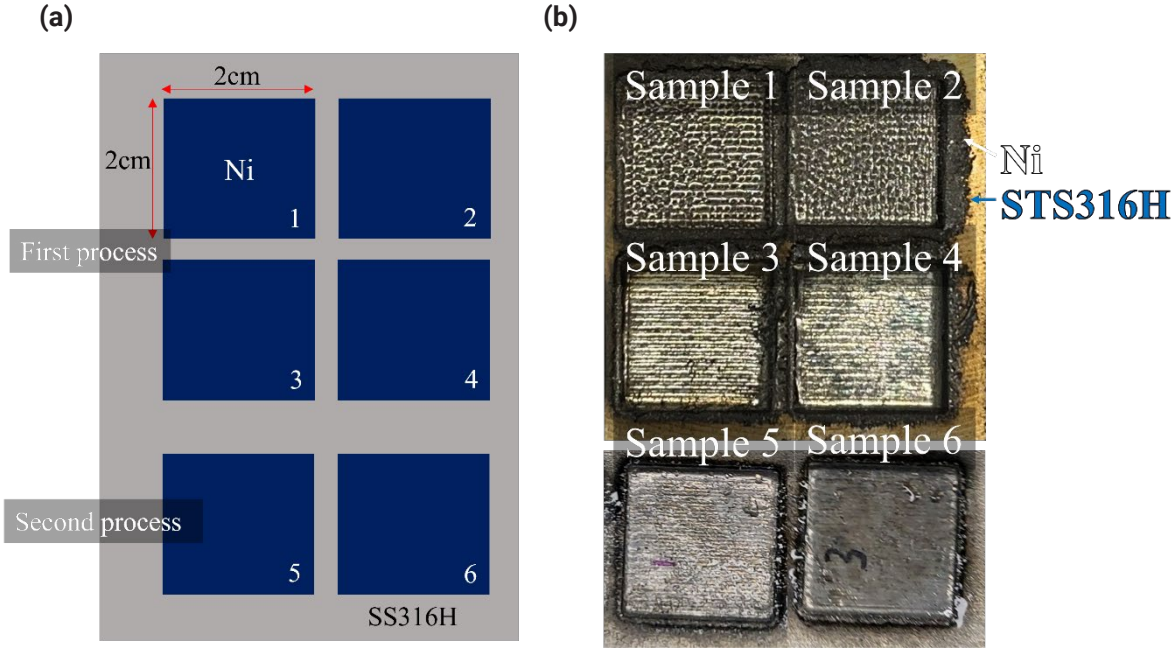

Fig. 1. (a) Schematic diagram of directed energy deposition and (b) macro photos of Ni DED samples built on STS-316H.

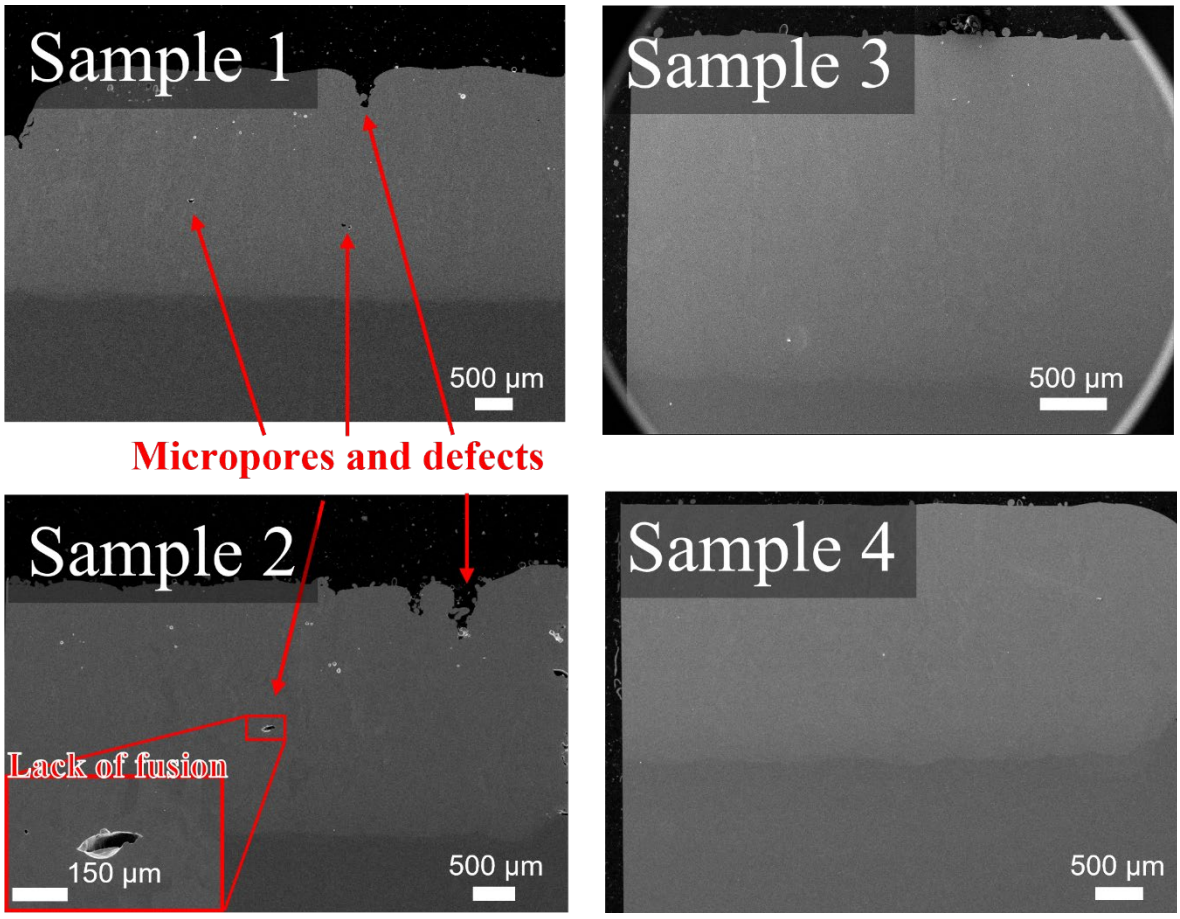

Fig. 2. SEM cross section images of samples (#1~4) fabricated via directed energy deposition.

Cr은 점차 감소하는 경향성을 보였으며 약 2mm 지점에서 99% 이상의 Ni 성분을 갖는 것을 확인하였다. Cr은 1.8 mm에서 Sample #3, #4에서 모두 검출되지 않았지만 Fe의 경우 각각 1.4, 1.9 wt% 나타나는 것을 확인하였다. 이는 STS316H 기판의 Fe, Cr 조성이 각각 70, 17wt%에 해당하기 때문에 원 조성 함량 차이에 따른 결과로 판단된다. 모든 조건에서 적층 높이 0.5 mm 지점에 Fe 함량은 20wt% 이내로 감소하였으며 Cr의 함량은 적층 높이 0.4 mm 지점에 5wt% 이내로 감소하였다.

레이저 파워 550 W, 스캔 스피드 1000mm/min 조건의 Sample #6 은 EDS 조성 분석 결과, 적층 높이 0.1mm에서 6 wt%의 Cr 함량을 나타내었다. 해당 조건에서 Fe 함량 또한 적층 높이 0.4mm 부근에서 17%로 다른 조건에서 보다 낮은 함량을 나타내었다. DED 공정에서 니켈의 함량은 적층 높이 0.5mm까지 Sample #6의 조건에서 가장 높으며 기판 조성 중 Cr과 Fe의 확산으로 인한 함량이 가장 낮은 것으로 나타났다.

일반적으로 용융염과 대면하는 Ni층에 Fe와 Cr성분이 8% 이상이 되면 용출로 인한 부식이 가속화된다. 본 연구에서는 여러 공정 조건의 변화에도 불구하고 Ni층의 두께를 2 mm 이상으로 하면 Fe, Cr 성분이 거의 검출되지 않았다. 따라서, 본 DED 조건을 활용할 경우 용융염 환경에서도 내식성을 유지할 수 있는 316H 기반 구조용 소재를 개발할 수 있을 것으로 판단된다.

4. Conclusion

본 연구에서는 STS316H 기판 위에 순수 Ni 분말을 DED 공정을 통해 적층 제조하였고 이 때 STS316H 소재 성분인 Fe와 Cr의 확산 조성을 분석하였다. 이에 따라 아래와 같은 결론을 얻었다.

1. 다이오드 레이저를 사용한 Pure Ni 적층 제조 시 낮은 레이저 파워는 체크 무늬 형상의 표면 결함과 Lack of fusion을 유발할 수 있으며 이는 적층 속도에 큰 영향을 끼친다.
2. SEM-EDS 조성 분석 결과 STS316H 소재에서 Fe와 Cr이 Ni 적층 방향으로 확산되었으며 적층 높이 0.5mm 지점에서 각각 평균 16.5, 4.2wt%의 조성을 갖는 것을 확인하였다.
3. Ni 조형체 내의 Fe, Cr 함량은 STS316H 조성에 따라 높은 함량을 갖고 있는 Fe 원소가 Cr 원소보다 높았으며, 적층 높이 2mm 지점에서 Fe는 1wt%이상 검출되었고, Cr은 검출되지

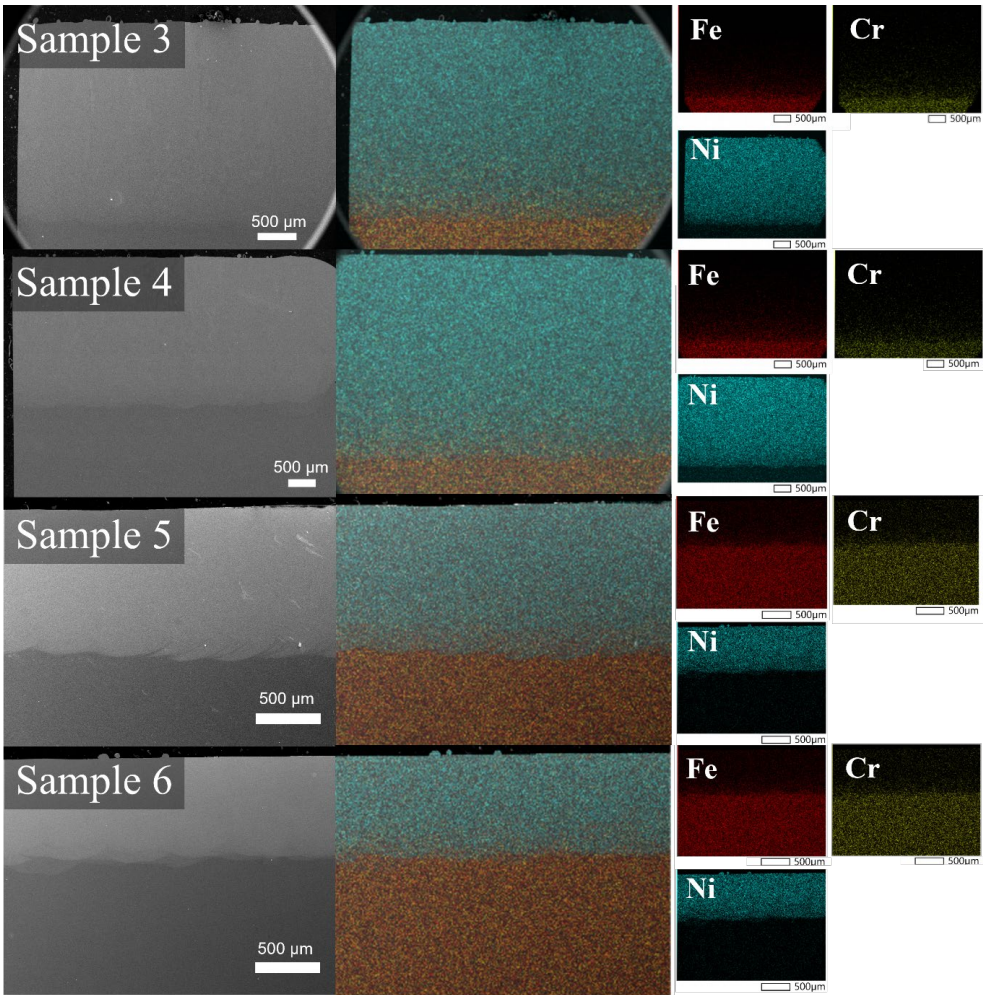

Fig. 3. SEM-EDX mapping images taken at interface regions between Ni and STS316H substate.

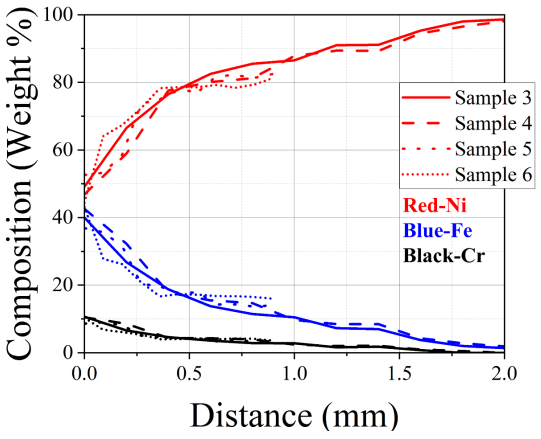

Fig. 4. Composition profiles of samples #3 through #6 as a function of distance from the interface between Ni and 316H. The profiles for samples #3 through #6 are represented by solid, dashed, dotted, and dash-dotted lines, respectively. Red, blue, and black colors indicate nickel, iron, and chromium, respectively.

않았다.

4. 본 연구는 Stainless Steel 소재로부터 순수 Ni 및 Ni 합금 적층 조형 시 적층 제조 높이 결정에 참고할 수 있으며 순수 Ni 소재의 DED 적층 제조 공정의 기초가 될 수 있다.

Conflict of Interest Declaration

교신저자는 현재 JPM편집이사로 봉사 중이지만, 논문 출판과정의 어떤 과정에서도 관여하지 않았습니다. 이 사항을 제외하면 저자들은 잠재적인 이해상충에 관련된 해당사항이 없음을 선언합니다.

Author Information

고의준, 이원찬 : 학생, 신기승: 연구원, 윤지현: 책임연구원, 김정한: 교수

Acknowledgement

이 논문은 2022년도 정부(방위사업청)의 재원으로 국방기술진흥연구소의 지원을 받아 수행된 연구임(21-107-F00-018(KRIT-CT-22-017), 차세대 다목적 고출력 전력생산기술(열원공급모듈 설계기술))

References

[1] J. Serp, M. Allibert, O. Beneš, S. Delpech, O. Feynberg, V. Ghetta, D. Heuer, D. Holcomb, V. Ignatiev, J. L. Kloosterman, L. Luzzi, E. M. Lucotte, J. Uhlíř, R. Yoshioka, and D. Zhimin: Prog. Nucl. Energy., **77** (2014) 308.

[2] K. O. Lee, M. A. Jessee, A. M. Graham, and D. J. Kropaczek: Nucl. Eng. Des., **417** (2024) 112824.

[3] Wang Y, Zhu C, Zhang M, Zhou W (2024) Chapter 9 - Molten salt reactors. In: Wang J, Talabi S, Leon SB y (eds) Nuclear Power Reactor Designs. Academic Press, pp 163–183

[4] Gomes DDS (2023) OVERVIEW OF THE PHYSICAL PROPERTIES OF MOLTEN SALT REACTOR USING FLIBE. JER 3:2–12. https://doi.org/10.22533/at.ed.3173362325107

[5] T. Ghaznavi, S. Y. Persaud and R. C. Newman: J. Electrochem. Soc., **169** (2022) 061502.

[6] F.-Y. Ouyang, C.-H. Chang and J.-J. Kai: J. Nucl. Mater., **446** (2014) 81.

[7] T. Ghaznavi, M. A. Bryk, S. Y. Persaud and R. C. Newman: Corros. Sci., **197** (2022) 110003.

[8] C. M. Abreu, M. J. Cristóbal, R. Losada, X. R. Nóvoa, G. Pena and M. C. Pérez: Electrochem. Acta, **51** (2006) 2991.

[9] M. Kondo,T. Nagasaka,T. Muroga,A. Sagara,N. Noda,Q. Xu,D. Ninomiya,N. Masaru,A. Suzuki and T. Terai: Fusion Sci. Technol., **56** (2009).

[10] A. I. Surenkov, V. V. Ignat'ev, S. S. Abalin, S. A. Konakov and V. S. Uglov: At. Energy, **124** (2018) 43.

[11] V. Errico, A. Fusco and S. L. Campanelli: Surf. Coat. Technol., **429** (2022) 127965.

[12] C. W. Park, R. N. Hajra, N. K. Adomako, W. Choo, S.-M. Yang, S.-J. Seo and J. H. Kim: Mater. Lett., **337** (2023) 133936.

[13] W. H. Kim, J. Ko and J. H. Kim: J. Powder Mater., **29** (2022) 314.

[14] J. Shao, G. Yu, S. Li, X. He, C. Tian and B. Dong: J. Alloys and Compd., **898** (2022) 162976.

[15] S. Sanchez, P. Smith, Z. Xu, G. Gaspard, C. J. Hyde, W. W. Wits, I. A. Ashcroft, H. Chen and A. T. Clare: Int. J. Mach. Tools Manuf., **165** (2021) 103729.

[16] K. Sridharan, T. R. Allen: Molten Salts Chem., (2013) 241.

Research Article

pISSN 2799-8525 · eISSN 2799-8681
J Powder Mater 2024;31(3):226-235

Journal of Powder Materials

Bandgap Tuning and Quenching Effects of In(Zn)P@ZnSe@ZnS Quantum Dots

Sang Yeon Lee[1,2], Su Hyun Park[1], Gyungsu Byun[2], Chang-Yeoul Kim[1,*]

[1]Nano-composite Materials Center, Korea Institute of Ceramic Engineering and Technology, 101 Soho-ro Jinju-si Gyeongsangnam-do 52851, Republic of Korea
[2]Department of Information and Communication Eng., Inha University, 100 Inha-ro Michuho-gu, Incheon 22212, Republic of Korea

InP quantum dots (QDs) have attracted researchers' interest due to their applicability in quantum dot light-emitting displays (QLED) or biomarkers for detecting cancers or viruses. The surface or interface control of InP QD core/ shell has substantially increased quantum efficiency, with a quantum yield of 100% reached by introducing HF to inhibit oxide generation. In this study, we focused on the control of bandgap energy of quantum dots by changing the Zn/(In+Zn) ratio in the In(Zn)P core. Zinc incorporation can change the photoluminescent light colors of green, yellow, orange, and red. Diluting a solution of as-synthesized QDs by more than 100 times did not show any quenching effects by the Förster resonance energy transfer phenomenon between neighboring QDs.

Keywords: InP; quantum dot; QLED; core/shell; FRET

Received: October 24, 2023
Revised: April 1, 2024
Accepted: April 13, 2024

***Corresponding author:**
Chang-Yeoul Kim
TEL: +82-55-792-2707
FAX: +82-55-792-2730
E-mail: cykim15@kicet.re.kr

1. Introduction

Recently, semiconducting quantum dots (QDs) have attracted many attentions for their various applications to light-emitting displays (LED) and biomarkers for the detection of cancers or viruses, since QDs of $CuCl_2$ and CdS was firstly synthesized [1, 2]. The bandgap energies of QDs could be controlled by changing the crystal sizes, then photoluminescent light color can be varied from blue to red due to their quantum confinements. The most widely studied QD material is CdSe for its stability and high quantum efficiency (QE), the rate of light emission versus incident photon. However, cadmium is a prohibited material for its toxicity. So, these days, InP QDs have been intensively researched. The InP QDs with highest QE of 100% was reported to develop QD LED by the inhibition of oxide generation on the surface of QDs with HF [3]. To improve the optical properties like QE, narrow band of PL light (smaller full-width at half maximum; FWHM), stability and the control of light color, many researches have been conducted [4-22]. It is known that the control of InP QD surfaces and InP core/shell interface is important [3, 6, 21, 22]. The adoption of halide precursor of indium is known to control the bandgap energies of InP QDs with the emission of blue, green and red color [23, 24]. Zn doping into InP QDs is known to be a good method to control the bandgap energy and improve the QE. The control of Zn/In ratio could change the P L(photoluminescence) peak wavelength and UV-Vis. absorption wavelength. N. Kirkwood et al [25] demonstrated that most of zinc atoms exist on the surface of InP QDs and only a small amount of zinc infiltrated into the lattice and contract the lattice parameter. In this study, we also change the ratio of In/(In+Zn) to investigate the effects of zinc incorporation for the InP QD core formation with the same composition of ZnSe and ZnS shell formation. We will also discuss the PL quenching effects of In(Zn)P@ZnSe@ZnS QDs concentrations by FRET (Förster resonance energy transfer) phenomenon.

2. Experiment

2.1. Chemicals

For the synthesis of In(Zn)P QD cores, indium(III) acetate

https://doi.org/10.4150/jpm.2024.00003

($In(Ac)_3$, 99.99 %, Sigma Aldrich, USA) and zinc acetate ($Zn(Ac)_2$, 99.99 %, Sigma Aldrich, USA) were purchase from Sigma Aldrich and trioctylamine was purchased from Daejung Chemical. (TOA, 99 %, Daejung, Korea) The source of phosphine was tris(trimethylsilyl)phosphine. (*ca*. 10 % in Hexane, $(TMS)_3P$; TCI Tokyo, Japan)

The capping agent for QDs was oleic acid (OA, 90 %, Sigma Aldrich, USA) and lauric acid (LA, 98%,Sigma Aldrich, USA) and palmitic acid. (LA, 98%,Sigma Aldrich, USA) For the formation of shell, ZnSe, selenium (Se, 99.99 %, Sigma Aldrich) and trioctylphosphine (TOP, 90 %, Sigma Aldrich) were purchased from Sigma Aldrich. For ZnS shell, sulfur (S, 99.98 %, Sigma Aldrich) was used. The organic solvents for the dispersion of QDs were 1-octadecene (ODE, 90 %, Sigma Aldrich, USA) and toluene (99.8 %, Sigma Aldrich), hexane (95 %, Sigma Aldrich) and chloroform (99 %, Duksan chemical, Korea). For the purification, acetone (99.8 %, Daejung) and methyl alcohol (99.5 %, Daejung) were used.

2.2. Synthesis of In(Zn)P@ZnSe@ZnS QDs

2.2.1 The synthesis of In(Zn)P core

The precursor chemicals of In(Zn)P cores were $In(Ac)_3$, $(TMS)_3P$, $Zn(Ac)_2$. In a 100 mL 3-neck flask, 1.2 mmol of $Zn(Ac)_2$ was dissolved in 2.4 mmol of OA and 10mL of ODE and degassed at 120 °C for 1 h (~500 mTorr). The reactant solution was observed to be clear. It was cooled to R·T under N_2 and then 0.6 mmol of $In(Ac)_3$ and 1.8mmol of LA were added. In this experiment, we varied In/(In+Zn) ratio from 0.33 to 1 by changing $Zn(Ac)_2$ to $In(Ac)_3$ molar ratio as shown in Table 1. The reactant was degassed at 120 °C for 1 h again (~500 mTorr). After that, 0.4mmol $(TMS)_3P$ precursor that was dissolved in 10 mL TOP was injected after heating up to 150 °C under N_2. The temperature was heated to 240°C and the heating mantle was removed to cool down to below 100 °C, rapidly. The reactant was transferred into two 50 mL conical tubes and 25 mL of acetone was added into each tube for purification. The reactant solution was centrifuged at 9,000 rpm for 5 m and the supernatant was discarded and the precipitate was taken and 25 mL of acetone was added and centrifuged at 9,000 rpm for 5 m. The purification was performed three times. Finally, the precipitate of In(Zn)P QD core was suspended in 2 mL toluene.

2.2.2 The synthesis of In(Zn)P@ZnSe@ZnS core/shell

The inner shell of In(Zn)P@ZnSe QDs was formed from $Zn(Ac)_2$ and SeTOP, which was synthesized by dissolving Se in TOP specified below. 2.4 mmol of $Zn(Ac)_2$ in 4.8 mmol of OA and 10mL TOA were dissolved and degassed at 120 °C for 1 h (~500 mTorr). The reaction temperature was raised to 180 °C under N_2, 2 mL of In(Zn)P cores synthesized previously were injected into the reaction solution and 0.72 mmol of SeTOP (in 10mL) TOP was added dropwise while raising the temperature to 320 °C and reacted for 1 h. Then, for the formation of the first outer shell of ZnS, that is, the final formation of In(Zn)P@ZnSe@ZnS core/shell, 0.8 mmol of STOP (in 10mL) were injected and reacted at 320 °C for 1h. For the formation of the second outer shell of ZnS, the reactant was cooled down to 280 °C, and 1.7 mmol of STOP (in 10mL) was injected into the reaction solution and reacted at 280 °C for 40 m. The reactant was cooled down to R·T and centrifuged by chloroform and methanol. The experimental procedure for the synthesis of In(Zn)P@ZnSe@ZnS was shown in Fig. 1.

2.3. Characterization

UV–Vis Absorption Spectroscopy and PL emission spectra

Steady-state absorption spectra of the QD samples diluted by 1 to 3,200 times were recorded by using a UV/vis spectrometer (V670, Jasco, Japan). Steady-state PL of QDs in toluene was measured by using a fluorescence spectrophotometer (HR4000, Ocean Optics, USA) excited by 425 nm blue LED light. The sample preparation of the QDs for the transmission electron microscopy (TEM) observation was conducted by putting the

Table 1. Moles of precursors for the In(Zn)P core, ZnSe Shell, and ZnS shell

Samples	In(Zn)P core					ZnSe shell		ZnS shell	
	In	*Zn*	*In/(In+Zn)*	*In & Zn (mmol)*	*TMS3P (mmol)*	*Zn (mmol)*	*SeTOP (mmol)*	*STOP (mmol)*	*STOP (mmmol)*
#1	1	2	0.33	1.8	0.4	2.4	0.72	0.8	1.7
#2	1	1	0.50	1.8	0.4	2.4	0.72	0.8	1.7
#3	2	1	0.67	1.8	0.4	2.4	0.72	0.8	1.7
#4	4	1	0.80	1.8	0.4	2.4	0.72	0.8	1.7
#5	1	0	1.0	1.8	0.4	2.4	0.72	0.8	1.7

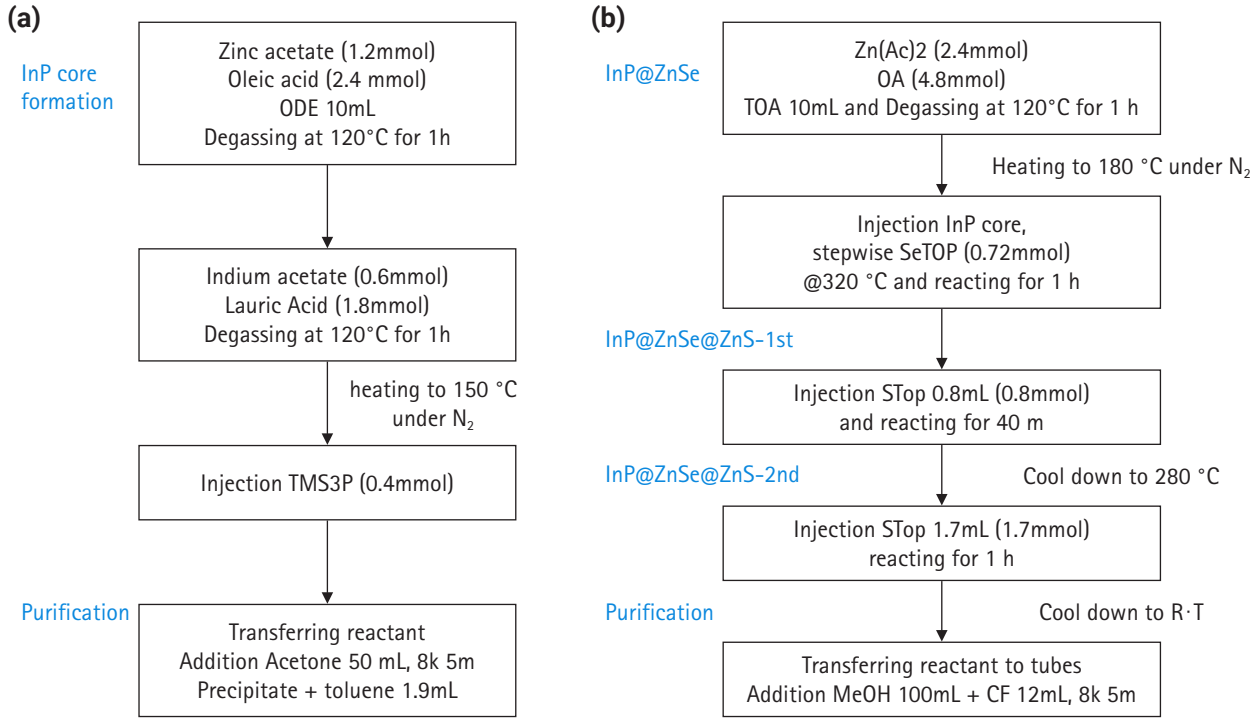

Fig. 1. Experimental process for the synthesis of the InP quantum dot core (a) and InP@ZnSe@ZnS quantum dot core/shell formation (b).

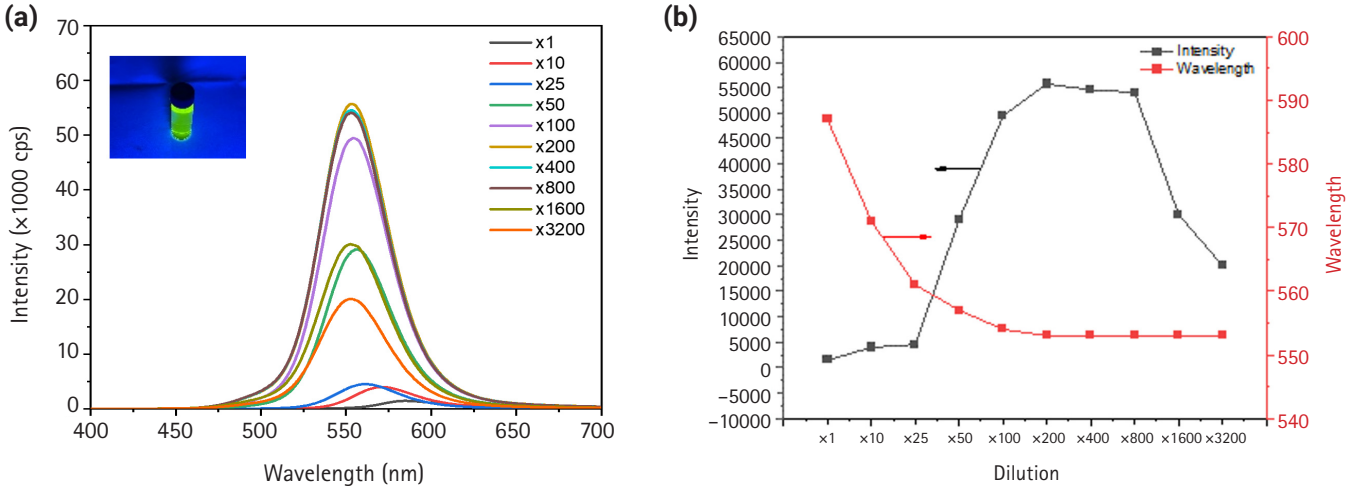

Fig. 2. Photoluminescence spectra of In(Zn)P@ZnSe@ZnS with an In/(In+Zn) ratio of 0.33 (a) and variations in the photoluminescence intensity and wavelength of the sample with the quantities of dilution.

solution-based QDs on carbon-coated copper grid and drying. The TEM observation was conducted by 400kV-high resolution TEM (JEOL-JEM-4010).

3. Results

Photoluminescence spectra of In(Zn)P@ZnSe@ZnS with 0.33 of In/(In+Zn) was shown in Fig. 2(a). The synthesized QDs showed the low PL peak intensity less than 10,000 cps. However, the dilution up to 25 times the intensity increase is slow and it increased very largely up to 50,000 cps for 100 times of dilution and saturated up to 800 times and then began to decrease up to 17,000 cps for 3,200 times of dilution. The wavelength of the emitted light of QDs with no dilution was 590 nm

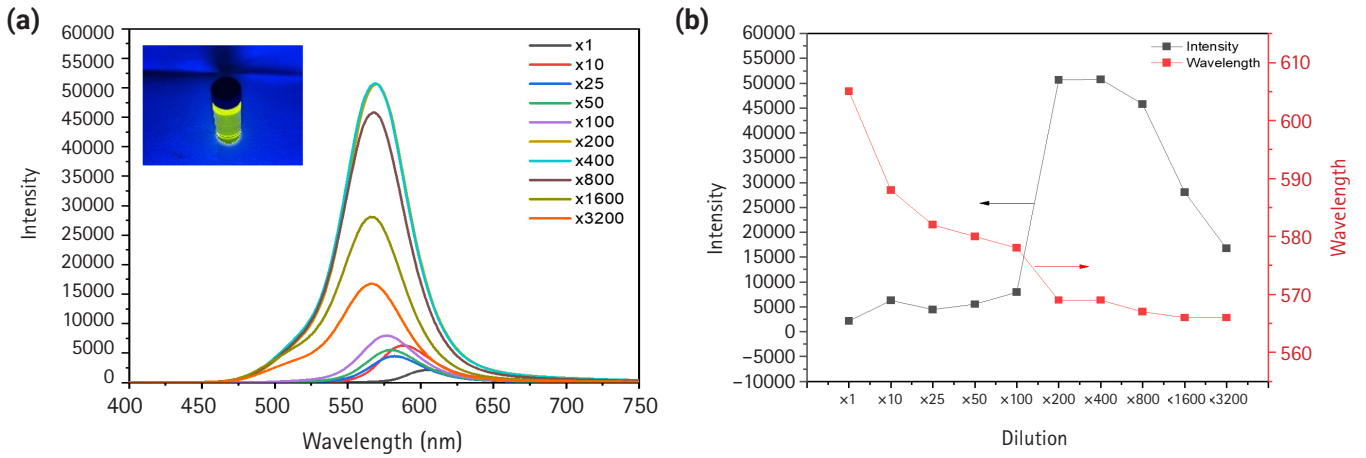

Fig. 3. Photoluminescence spectra of In(Zn)P@ZnSe@ZnS with an In/(In+Zn) ratio of 0.5 (a) and variations in the photoluminescence intensity and wavelength of the sample according to the quantities of dilution.

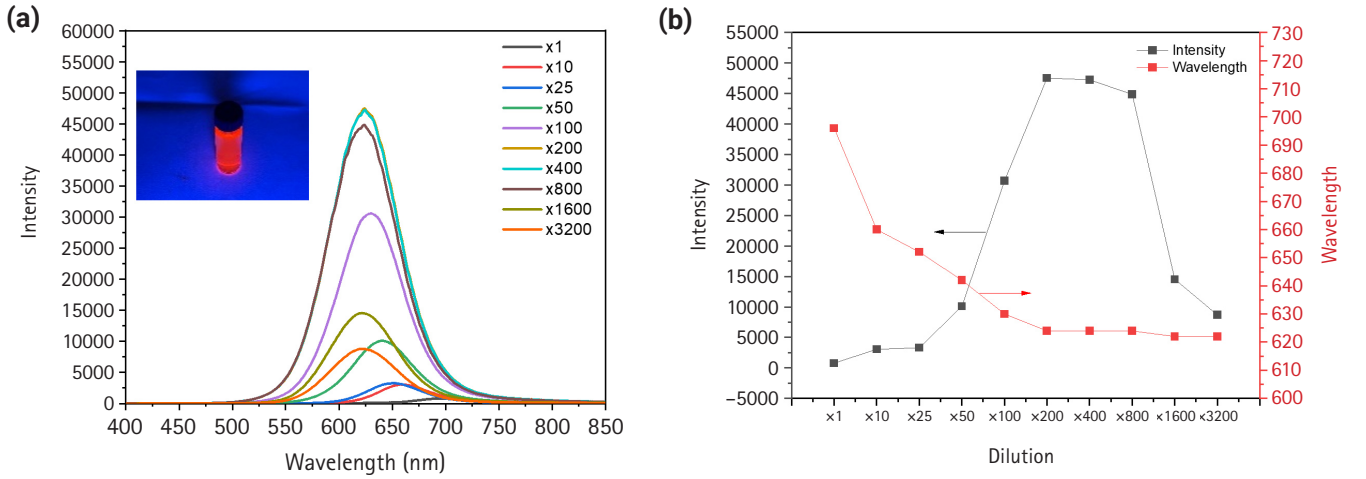

Fig. 4. Photoluminescence spectra of In(Zn)P@ZnSe@ZnS with an In/(In+Zn) ratio of 0.67 (a) and variations in the photoluminescence intensity and wavelength of the sample according to the quantities of dilution.

and decreased to 553 nm for 100 times of dilution and then did not show any change. As shown in Fig 2 (a), the light color of the sample was green. When the contents of In/(In+Zn) was 0.5, that is, 1;1 molar ratio of In to Zn, as shown in Fig. 3. the PL intensity increased very small up to 50 times of dilution, and then increased very largely up to 50,000 cps for 100 and 200 times of dilution. After that, it decreased to 15,000 cps for 3,200 times of dilution. The wavelength of the samples decreased from 605 nm for no dilution to 566 nm for 3,200 times of dilution. The light color of the sample with 200 times of dilution was greenish yellow color, equivalent to the wavelength of 560 nm. The increase of indium contents to 0.67 of In/(In+Zn) ratio increased the emission light wavelength to 605 nm for 200 times of diluted sample. The light color under 420 nm UV light illumination was red as shown in Fig. 4. The PL intensity variations with dilution quantities showed the almost sample trend. There is a small increase of PL intensity for 25 times of dilution and then increased greatly up to 200 times of dilution and began to decrease for more than 800 times of dilution. As shown in Fig. 5, the more increase of indium ratio to 0.8 decreased the wavelength of emitted light to 580 nm, yellow light. The PL intensity increased slightly to 2,500 cps for 100 times of dilution and then increase greatly for 200 to 1,600 times of dilution and began to decrease for greater than 1,600 times of dilution. The PL spectra of In(Zn)P@ZnSe@ZnS with 1 of In/(In+Zn) was shown in Fig. 6. This QD sample without zinc showed the red-

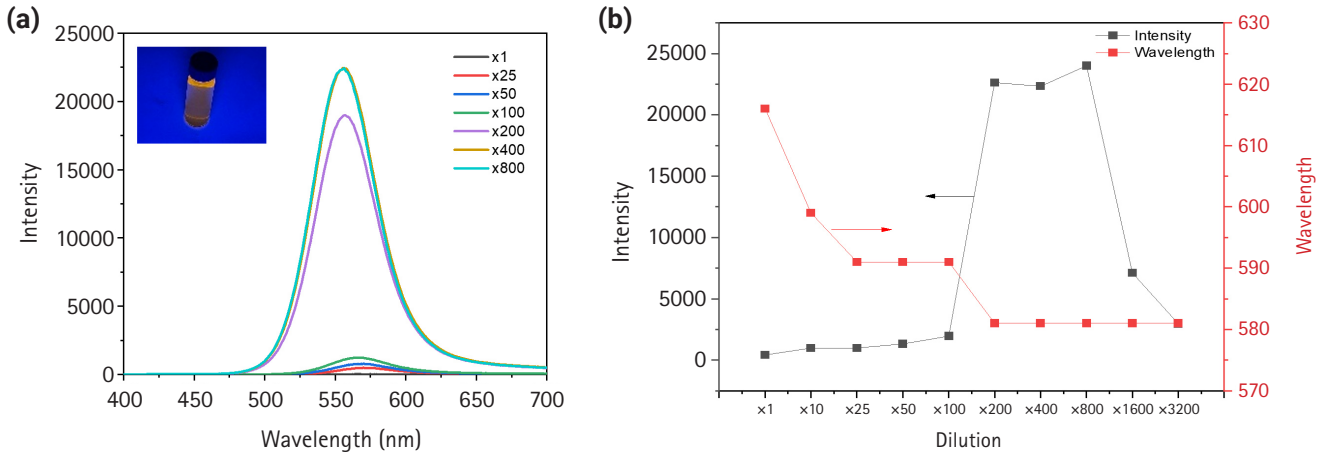

Fig. 5. Photoluminescence spectra of In(Zn)P@ZnSe@ZnS with an In/(In+Zn) ratio of 0.8 (a) and variations in the photoluminescence intensity and wavelength of the sample according to the quantities of dilution.

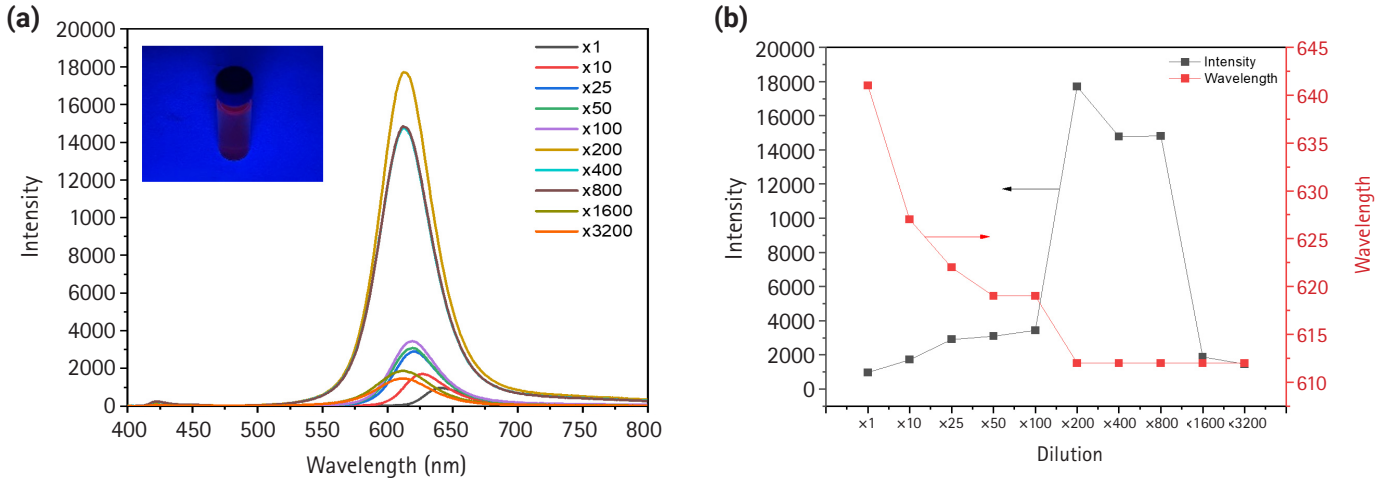

Fig. 6. Photoluminescence spectra of In(Zn)P@ZnSe@ZnS with an In/(In+Zn) ratio of 1 (a) and variations in the photoluminescence intensity and wavelength of the sample according to the quantities of dilution.

light emission with 613 nm of wavelength. The emitted light wavelength without dilution was 640 nm and decreased gradually to 613 nm for more than 200 times of dilution.

The absorbance spectra of the QDs with different In/(In+Zn) ratio diluted at 200 times and their corresponding PL spectra were shown in Fig 7 (a) and (b), and the photographs of QDs with 0.33, 0.5, 0.67, 0.8 and 1 of In/(In+Zn) ratio under 420 nm of UV illumination were shown in Fig. 7 (c). The absorbance peak appeared at 523 nm for 0.33 ratio, 573 nm for 0.5, 587 nm for 0.67, 536 nm for 0.8 and 470 nm for 1 In/(In+Zn) ratio. The corresponding PL emission peaks were 553, 569, 624, 581, and 612 nm, respectively. The colors of the QDs were green, yellow, red, orange, and dark red, respectively. First absorption peak wavelengths, absorbances, band edge energy (E_{QD}), volume of QDs (V_{QD}), molar extinction coefficients (ε), and molar concentrations (C) of QD samples were summarized in Table 2. As In/(In+Zn) ratio less than 0.67, the QDs showed the green or yellow colors at PL peak range between 550-570 nm, and their absorbance peaks increased from 535 nm for 0.33 ratio to 587 nm for 0.67nm. For more than 0.67 ratio, PL peaks showed red color with more than 600 nm (except 581 nm for 0.8 of the ratio) and their absorbance peak decreased from 587 nm to 470 nm. (Fig. 7 (c)) As mentioned in the introduction section, Kirkwood et al [25] specifically studied of Zn location in InP

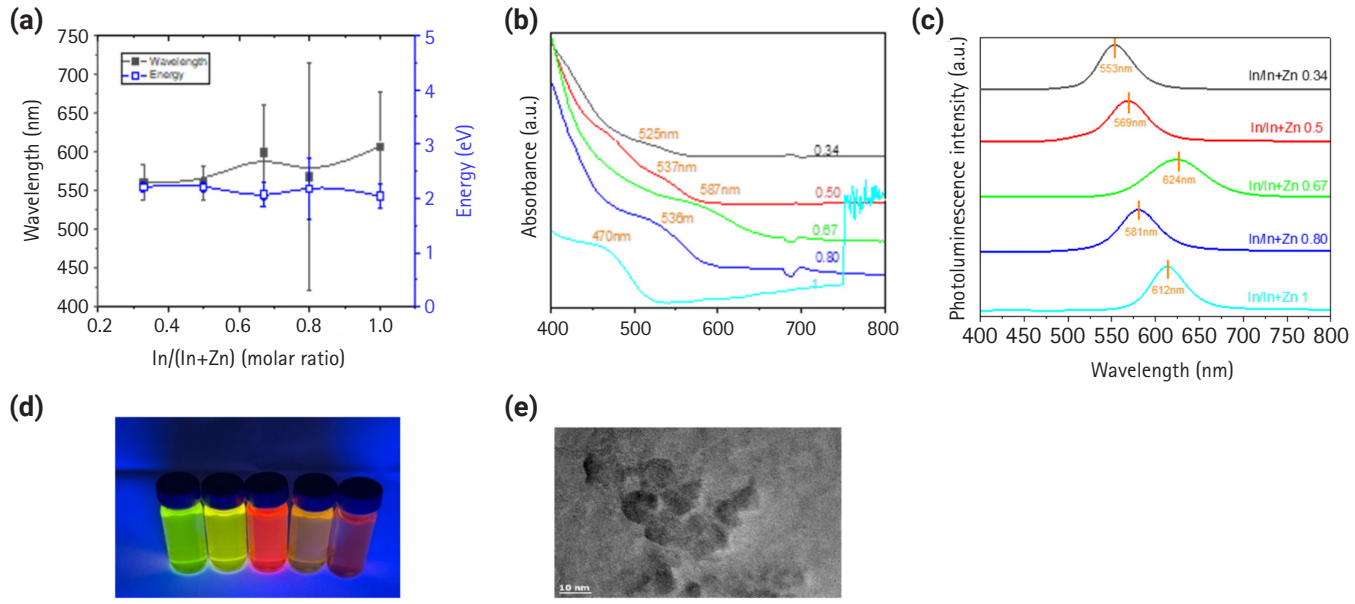

Fig. 7. Ultraviolet (UV)-visible absorbance (a) photoluminescence spectra (b) of In(Zn)P@ZnSe@ZnS with different ratios of In/(In+Zn), diluted 100 times, photoluminescence peak wavelengths and their energies for the samples (c), transmission electron microscopy images of In(Zn)P@ZnSe@ZnS quantum dots with an In/(In+Zn) ratio of 0.33 (d), and the sample photographs under UV illumination (e).

Table 2. First absorption peak wavelengths, absorbances, band edge energy (EQD), volume of QDs (VQD), molar extinction coefficients (ε), and molar concentrations (C) of QD samples.

Samples	In/(In+Zn)	Wavelength (1st peak) /nm	Absorbance	EQD	LQD	VQD	ε	C
				eV	nm	nm^3	$x10^6M^{-1}cm^{-1}$	$x10^{-9}M$
#1	0.33	525	0.1857	1.98	7.30	203.7	2.732	67.9
#2	0.5	536	0.0926	2.03	6.75	161.0	2.160	42.9
#3	0.67	586	0.2097	1.77	11.14	723.9	9.710	21.6
#4	0.8	535	0.3101	2.02	6.85	168.3	2.257	137
#5	1.0	470	1.15844	0.36	4.3	41.5	556,424	2,081

QD, quantum dot.

QD and structural and optical properties of In(Zn)P QDs by Zn incorporation ratio. We summerized PL properties of QDs in Table 3.

We observed the TEM images of the QDs for 0.33 of the ratio (Zn : In = 2:1) to find out the QD crystal size about 10 nm with an almost spherical shape (Fig. 7 (d) and Fig. 8).

4. Discussion

4.1. Size and volume of QDs

We can calculate the size of QD nanocrystals by using the following formula [26].

$$L_{QD} = (\frac{C}{E_{QD}-E_b})^{1/\alpha},$$

where L_{QD} is the average nanocrystal edge length, E_{QD} is the energy of band edge transition, E_b is the bulk band gap of InP (1.35 eV), and C and α are empirically derived fitting parameters (4.25 and 0.96, respectively for a tetrahedral-shaped InP QD nanocrystal). We need to obtain the average volume (V_{QD}) of a single QD crystal by using the following formula.

$$V_{QD} = \frac{4}{3}\pi(\frac{L_{QD}}{2})^3$$

As shown in Table 2, the QD crystal sizes were 7.30 nm for 0.33 of In/(In+Zn) ratio, 6.75 nm for 0.5, and the largest value of 11.14 nm for 0.67 of the ratio, and decreased to 6.85 nm for 0.8 and 4.3 nm for 1. The QD crystal size for 0.33 by TEM observation is about 10 nm, which is a little greater than the calculated size of 7.3 nm. However, the calculated QD crystal size

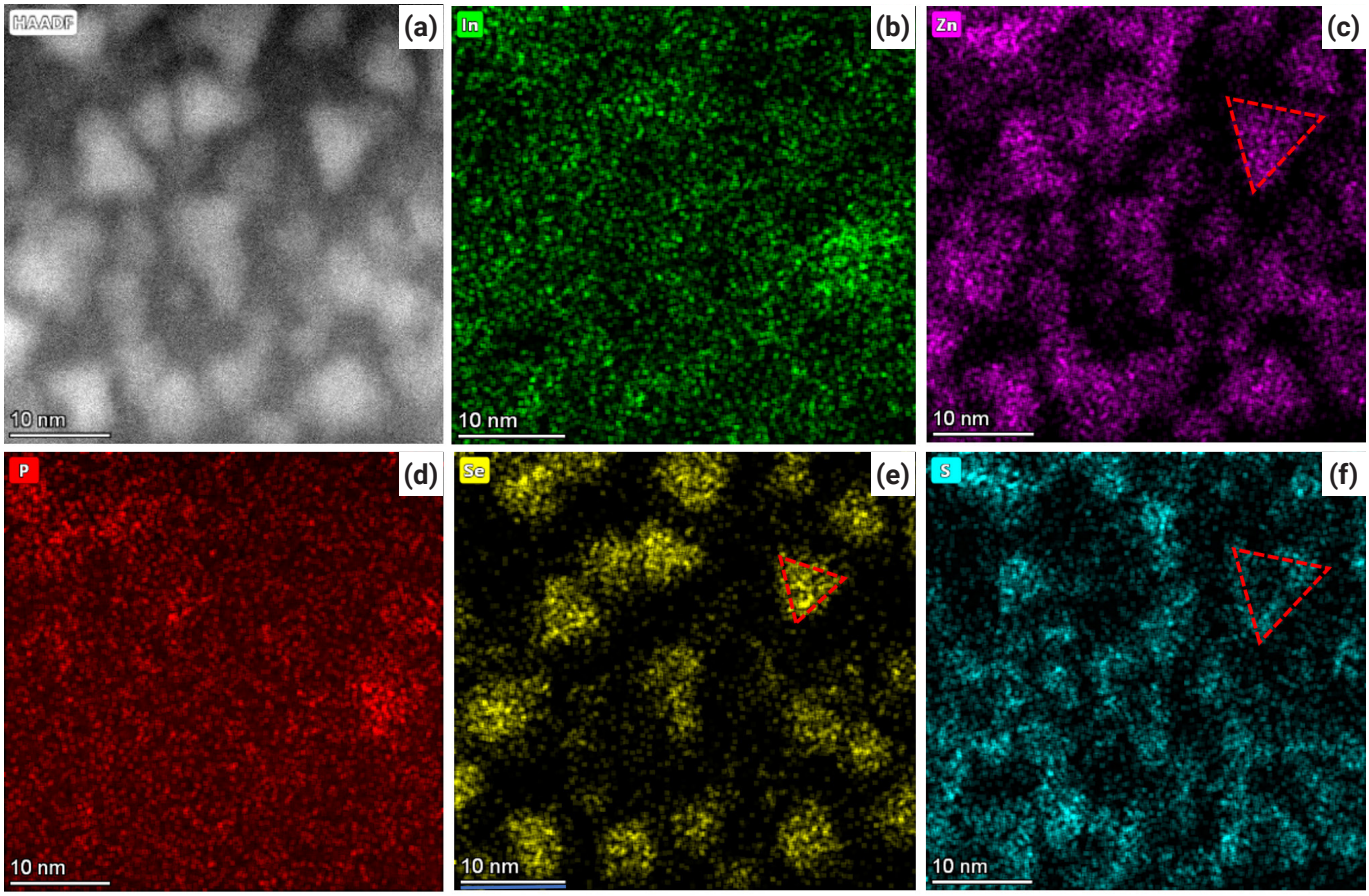

Fig. 8. Scanning electron microscopy and energy-dispersive X-ray spectroscopy mapping images of In(Zn)P@ZnSe@ZnS QDs.

is considered to be 8.65 ± 1.35 nm (standard error) (Fig. 8).

4.2. Absorptivity (ε_{1s}) and molar concentration of QDs

The concentration of InP@ZnSe@ZnS QDs is determined by the absorbance of UV–Vis spectroscopy. The intrinsic absorption coefficient of a QD material, μ_i, is size-independent at sufficiently short wavelengths. The absorbance (A) of QDs can be expressed as the Beer-Lambert equation, $A = \varepsilon cl$, where ε is a molar attenuation (or extinction) coefficient ($M^{-1}cm^{-1}$), c is a molar concentration (M) of QDs, and l is an optical path length of cuvette (in meter scale). The absorbance of A is also expressed as $A = \ln I_0/I$, where I_0 is an intensity of incident light and I is that of transmitted light. The absorbance can be shown as $A = \frac{\mu_i f l}{ln10}$, where f is a volume fraction of QDs. μ_i is related with $\sigma = V_{QD} \times \mu_i$. σ is the absorption cross section and the theoretical $\mu_{i,th}$ is used as a comparator, as it represents the intrinsic absorption of the bulk semiconductor, and is calculated using wavelength (λ)-dependent optical constants, including the real (n) and imaginary (k) parts of the refractive index of ZnSe and the local field factor $|f_{LF}|$, as well as the refractive index of the surrounding medium (n_s) [26].

$$\mu_{i,th} = \frac{2\pi}{n_s \lambda_0} |f_{LF}|^2 2 n_{QD} k_{QD},$$

$$|f_{LF}|^2 = \frac{9 n_s^4}{(n^2 - k^2 + 2n_s^2)^2 + 4(nk)^2}.$$

Comparing to Beer-Lambert's law, the molar extinction coefficient, ε, from this intrinsic absorption coefficient is expressed as following equation.

$$\varepsilon = \frac{N_A V_{QD}}{1000 ln10} (f_{InP} \mu_{i,InP} + f_{ZnSe} \mu_{i,ZnSe}),$$

where N_A is the Avogadro number, V_{QD} is the average volume of the In(Zn)P@ZnSe@ZnS QDs, and $\mu_{i,InP}$ is 8.5×10^4 cm^{-1} at 413 nm and μ_i,ZnSe is the intrinsic absorption coefficient of

Table 3. Photoluminescence wavelengths and intensities, FWHM and absorbance of In(Zn)P@ZnSe@ZnS QDs with varying molar ratios of In/(In+Zn).

Samples	In/(In+Zn)	PL peak	Intensity	FWHM	Absorbance
	Molar ratio	nm	cps	nm	
#1	0.33	553	55,751	43	0.1857
		571	36,179	45	
		559	57,611	44	
	Mean (95%, k=2)	561±23	49,847±29,494	44±2.5	
#2	0.5	569	50,782	52	0.0926
		560	13,441	42	
		551	28,507	49	
	Mean (95%, k=2)	560±22	30,910±46,667	48±13	
#3	0.67	574	19,663	41	0.2097
		600	54,083	56	
		624	47,526	66	
	Mean (95%, k=2)	599±62	40,424±45,400	54±31	
#4	0.8	556	22,435	53	0.3101
		579	22,402	49	
	Mean (95%, k=2)	568±146	22,418±210	51±25	
#5	1	612	17,704	43	1.15844
		601	15,998	47	
	Mean (95%, k=2)	607±70	16,851±10,838	45±25	

QD, quantum dot.

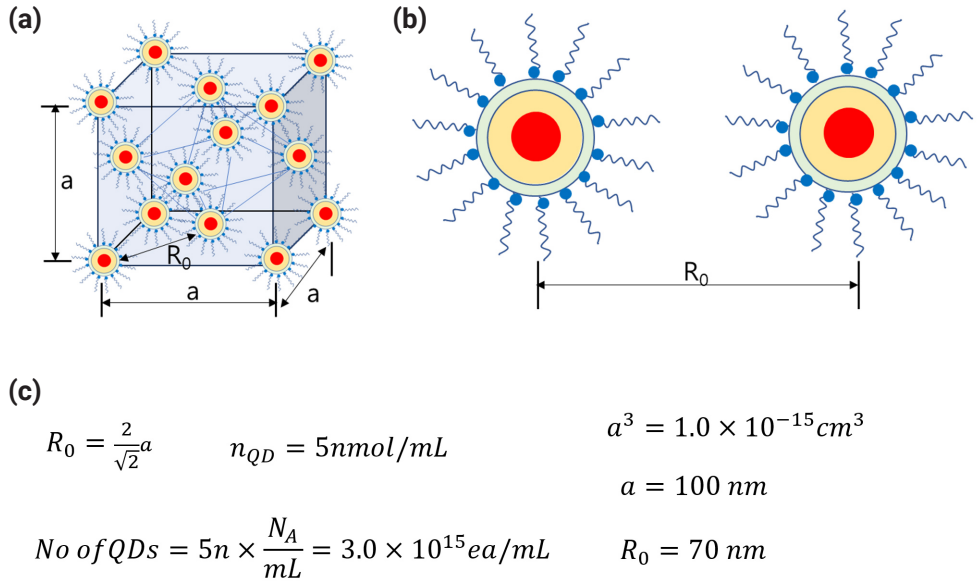

Fig. 9. Schematic model of In(Zn)P@ZnSe@ZnS QDsquantum dot (QD) dispersion in a solvent (a), the distance R0 between neighboring suface-capped QDs, and the calculated average FRET distance of R0 for 5 nmol/mL of QDsa QD concentration. (Red of 5 nmol/mL (red: In(Zn)P core, Yellow yellow: ZnSe shell, Green green: ZnS shell, line with head and tail : capping agent)).

InP at 413 nm. We adopted 5.0 × 10^4 cm^{-1} (theoretical value) of μ_i,ZnSe at 420 nm. f_{InP} and f_{ZnSe} is volume fractions of InP and ZnSe of core/shell components of QDs, where the values f_{InP} and f_{ZnSe} were adopted as 0.037 and 0.963, respectively in the

reference [4]. The molar extinction coefficient of QDs were in the range of 2.25~9.70 × 10^6 $M^{-1}cm^{-1}$ and the molar concentration were between 20 and 137 nM. The concentrations were of the diluted QDs by 200 times, and so the as-synthesized molar concentration was calculated to be between 4-27 μM.

4.3. Förster Resonance Energy Transfer (FRET) effects of QDs

Fluorescence resonance energy transfer (originally Förster resonance energy transfer; FRET) is energy transfer from donor to acceptor, In(Zn)P@ZnSe@ZnS QDs fluorophore and oleic acid in this paper. The FRET efficiency (E) depends on many physical parameters such as (1) the distance between the donor and the acceptor, (2) the spectral overlap of the donor emission spectrum, and (3) the relative orientation of the donor emission dipole moment. In this study, the acceptor of oleic acid is not a fluorophore and so it plays only as an energy transfer path from the donor the QDs to lipid organics. The rate of energy transfer (k_{ET}) can be expressed like the following equation. $k_{ET} = (\frac{R_0}{r})^6 \frac{1}{\tau_D}$, where τ_D is the donor's fluorescence lifetime in the absence of the acceptor, R_0 being the Förster distance of this pair of donor and acceptor, i.e. the distance at which the energy transfer efficiency is 50% and r is the distance between donor and acceptor [27].

$$R_0{}^6 = \frac{9000 \ln(10)\, Q_D k^2}{128\pi^5 n^4 N_A} \int_0^\infty F_D(\lambda)\epsilon_A(\lambda)\lambda^4\, d\lambda / \int_0^\infty F_D(\lambda) d\lambda$$

$$R_0{}^6 = 8.79 \times 10^{-25} n^{-4} Q_D k^2 J(\lambda) cm^6$$

where Q_D is the fluorescence quantum yield of the donor in the absence of the acceptor, k^2 is the dipole orientation factor, n is the refractive index of the medium, N_A is the Avogadro constant, ϵ_A (λ) is the acceptor molar extinction coefficient, and $J(\nu)$ is the spectral overlap integral calculated as $\int_0^\infty F_D(\lambda)\epsilon_A(\lambda)\lambda^4\, d\lambda / \int_0^\infty F_D(\lambda) d\lambda$. Here, we use hexane as a medium with refractive index 1.33 and Q_D is 0.4 and ϵ_A (λ) is 1.14x10^4 $mol^{-1}cm^{-1}$, the wavelength of In(Zn)P@ZnSe@ZnS emission is 540 nm, then we obtained R_0 as 47.6 nm. The molar concentration of QDs calculated by Beer-Lambert law was about 5 μM, that is, 5 nmol/mL. It means that the number of QDs was 3.0×10^{15}ea/mL and the average distance between neighboring QDs is calculated as about 70 nm. In our study, the quenching effect by FRET appeared at less than 100 dilution, 50 nM, where the neighboring distance is 7 μm, as shown in Fig. 9.

5. Conclusions

In our study, we discussed effects of the ratio of In/(In+Zn) to the PL and UV-Vis. absorption properties of In(Zn)P@ZnSe@ZnS QDs. The PL light of the QDs with the ratio of more than 2/3 indium is red color and the PL lights of the QDs with less than 2/3 of In ratio show green and yellow colors. The brightest red PL properties of the QDs ca be obtained for 2/3 ratio of In/(In+Zn) with the largest crystal size. The FRET quenching effects of the QDs suppress the PL intensities with less than R_0, 70 nm calculated FRET equation. The dilution of QDs solution by more than 100 times with about 50 nmol/mL does not show FRET phenomenon with the distance of 7 μm between the neighboring QDs.

Conflict of Interest Declaration

The authors declare no competing financial interests or personal relationships.

Author Information

S. Y Lee: Student, S. H. Park: Researcher, G. Byun: Professor, C.-Y. Kim: Principal Researcher

Acknowledgments

The authors are appreciated for the financial support by the project of nano-material development of Korean national research foundation (NRF-2021M3H4A6A03103774) and the strategic material development program of Korea Institute of Ceramic Engineering and Technology (KPP21003).

References

[1] A.I. Ekimov and A.A. Onushchenko: JETP Lett., **34** (1981) 345.
[2] R. Rossetti and L. Brus: J. Phys. Chem., **86** (1982) 4470.
[3] Y. Won, O. Cho, T. Kim, D.-Y. Chung, T. Kim, H. Chung, H. Jang, J. Lee, D. Kim, and E. Jang: Nature., **575** (2019) 638.
[4] Y. Kim, S. Ham, H. Jang, J. Min, H. Chung, J. Lee, D. Kim, and E. Jang: ACS Appl. Nano Mater., **2** (2019) 1496.
[5] R. Xie, D. Battaglia, and X. Peng: J. Am. Chem. Soc., **129**

(2007) 15432.
[6] J. Ziegler, S. Xu, E. Kucur, F. Meister, M. Batentschuk, F. Gindele, and T. Nann: Adv. Mater., **20** (2008) 4068.
[7] E. Jang, S. Jun, H. Jang, J. Lim, B. Kim, and Y. Kim: Adv. Mater., **22** (2010) 3076.
[8] S. Tamang, C. Lincheneau, Y. Hermans, S. Jeong, and P. Reiss: Chem. Mater., **28** (2016) 2491.
[9] P. Ramasamy, N. Kim, Y. Kang, O. Ramirez, and J. Lee: Chem. Mater., **29** (2017) 6893.
[10] Q. Wu, F. Cao, S. Wang, Y. Wang, Z. Sun, J. Feng, Y. Liu, L. Wang, Q. Cao, Y. Li, B. Wei, W. Wong, and X. Yang: Adv. Sci., **9** (2022) 2200959.
[11] L. Qian, Y. Zheng, J. Xue, and P. Holloway: Nat. Photon., **5** (2011) 543.
[12] B. S. Mashford, M. Stevenson, Z. Popovic, C. Hamilton, Z. Zhou, C. Breen, J. Steckel, V. Bulovic, M. Bawendi, S. C. Sullivan, and P. T. Kazlas: Nat. Photon., **7** (2013) 407.
[13] Z. Zhang, Y. Jin, Y. Niu, H. Cao, X. Liang, L. Chen, J. Wang, and X Peng: Nature., **515** (2014) 96.
[14] J. R. Manders, L. Qian, A. Titov, J. Hyvonen, J. T. Scott, K. P. Acharya, Y. Yang, W. Cao, Y. Zheng, J. Xue, and P. H. Holloway: J. Soc. Inf. Disp., **23** (2015) 523–528
[15] J. Lin, Y. Hu, X. Guo, Y. Lv, Z. Tang, J. Zhao, Y. Fan, N. Zhang, Y. Wang, and X. Liu: ACS Appl. Mater. Interfaces, **9** (2017) 38755.
[16] W. K. Bae, Y.-S. Park, J. Lim, D. Lee, L. A. Padilha, H. McDaniel, I. Robel, C. Lee, J. M. Pietryga, and V. I. Klimov: Nat. Commun., **4** (2013) 2661.
[17] Y. Yang, Y. Zheng, W. Cao, A. Titov, J. Hyvonen, J. R. Manders, J. Xue, P. H. Holloway, and L. Qian: Nat. Photon., **9** (2015) 259.
[18] W. Cao, C. Xiang, Y. Yang, Q. Chen, L. Chen, X. Yan, and L. Qian: Nat. Commun., **9** (2018) 2608.
[19] Y. Li, X. Hou, X. Dai, Z. Yao, L. Lv, Y. Jin, and X. Peng: J. Am. Chem. Soc., **141** (2019) 6448.
[20] P. Reiss, M. Carriere, C. Lincheneau, L. Vaure, and S. Tamang: Chem. Rev., **116** (2016) 10731.
[21] O. I. Mićić, K. M. Jones, A. Cahill, and A. J. Nozik: J. Phys. Chem. B., **102** (1998) 9791.
[22] J. L. Stein, W. M. Holden, A. Venkatesh, M. E. Mundy, A. J. Rossini, G. T. Seidler, and B. M. Cossairt: Chem. Mater., **30** (2018) 6377.
[23] M. D. Tessier, E. A. Baquero, D. Dupont, V. Grigel, E. Bladt, S. Bals, Y. Coppel, Z. Hens, C. Nayral, and F. Delpech: Chem. Mater., **30** (2018) 6877.
[24] M. D. Tessier, D. Dupong, K. D, J. D. Roo, and Z Hens: Chem. Mater., **27** (2015) 4893.
[25] N. Kirkwood, A. De Backer, T. Altantzis, N. Winckelmans, A. Longo, F.V. Antolinez, F. T. Rabouw, L.De Trizio, J. J. Geuchies, J. T. Mulder, N. Renaud, S. Bals, L. Manna, and A. J. Houtepen: Chem. Mater., **32** (2020) 557.
[26] M. Parvizian, J. Bechter, J. Huber, N. Chettata, and J. De Roo: J. Chem. Educ., **100** (2023) 1613.
[27] G. Beane, K. Boldt, N. Kirkwood, and P. Mulvaney: J. Phys. Chem. C., **118** (2014) 18079.

Research Article

pISSN 2799-8525 · eISSN 2799-8681
J Powder Mater 2024;31(3):236-242

Journal of Powder Materials

Investigation of the Thermal-to-Electrical Properties of Transition Metal-Sb Alloys Synthesized for Thermoelectric Applications

Jong Min Park[1,2], Seungki Jo[1], Sooho Jung[1], Jinhee Bae[1], Linh Ba Vu[1,2], Kwi-Il Park[2], Kyung Tae Kim[1,*]

[1]Department of 3D Printing Materials, Korea Institute of Materials Science, Changwon, Gyeongnam 51508, Republic of Korea
[2]Department of Materials Science and Metallurgical Engineering, Kyungpook National University, Daegu 41566, Republic of Korea

The development of thermoelectric (TE) materials to replace Bi_2Te_3 alloys is emerging as a hot issue with the potential for wider practical applications. In particular, layered Zintl-phase materials, which can appropriately control carrier and phonon transport behaviors, are being considered as promising candidates. However, limited data have been reported on the thermoelectric properties of metal-Sb materials that can be transformed into layered materials through the insertion of cations. In this study, we synthesized FeSb and MnSb, which are used as base materials for advanced thermoelectric materials. They were confirmed as single-phase materials by analyzing X-ray diffraction patterns. Based on electrical conductivity, the Seebeck coefficient, and thermal conductivity of both materials characterized as a function of temperature, the zT values of MnSb and FeSb were calculated to be 0.00119 and 0.00026, respectively. These properties provide a fundamental data for developing layered Zintl-phase materials with alkali/alkaline earth metal insertions.

Keywords: Thermoelectric materials; Transition metal; Antimony; Electrical properties; Thermal conductivity

Received: March 26, 2024
Revised: April 24, 2024
Accepted: April 24, 2024

***Corresponding author:**
Kyung Tae Kim
Tel: +82-55-280-3506
Fax: +82-55-280-3474
E-mail: ktkim@kims.re.kr

1. Introduction

Thermoelectric (TE) technology is attracting attention for energy production and efficient energy utilization. In particular, compared to other renewable energy sources, it is the unique technology that can directly convert thermal energy into electric energy or provide heating and cooling through electricity without any driving part. Bismuth telluride (Bi_2Te_3)-based alloys have been considered as representative materials for practical TE applications [1-3]. That is due to suitable combination between low thermal conductivity caused by their layered structure composed of Van der Waals bonds and a good power factor ($S^2\sigma$, PF) resulting from the mixture of covalent and ionic bonds in the temperature range of 273 – 500 K. These characteristics result in a superior dimensionless thermoelectric figure of merit (zT), calculated by the formula $zT = (S^2\sigma T)/\kappa$ (S: Seebeck coefficient, σ: electrical conductivity, κ: thermal conductivity, and T: absolute temperature), in the room temperature region compared to other materials [4-6]. However, Bi_2Te_3-based materials are often limited in more wide applications due to their performance degradation outside the room temperature range and the scarcity and toxicity of raw materials. Therefore, various materials are being investigated as possible replacements for Bi_2Te_3 alloy.

Among these studies, zintl phase materials such as Yb-Mg-Sb and Na-Ga-Sn, which combine metals and nonmetals, are attracting attention for their excellent charge transfer and controllable thermal conduction [7-10]. Recently, zintl phase materials composed of alkali/alkaline earth metal-transition metal-pnictogen elements in atomic ratios of 1-1-1 and 1-2-2 are known to exhibit a layered structure similar to Bi_2Te_3, which is expected to result in thermoelectric performances [11-13]. Transition metals can easily accept electrons released by the ionization of alkali/alkaline earth metals due to their various oxidation numbers. In particular, transition metal-pnictogen materials composed of d_5 and d_{10} ions such as Zn^{2+}, Fe^{3+}, and Mn^{2+} have been reported to form layered structures with the

https://doi.org/10.4150/jpm.2024.00031

insertion of alkali/alkaline earth metals. [14, 15]. In addition, the energy bandgap of the material generally tends to decrease as the atomic radius of the pnictogen element(As, Sb, and Bi) in periodic table increases [16, 17]. Therefore, antimony (Sb) rather than bismuth (Bi) can be typically utilized to achieve the energy bandgap size of about a few hundred meV such as SnSe, Bi_2Se_3, and Bi_2Te_3. Toberer et al. synthesized AZn_2Sb_2 (A = Sr, Ca, Yb, Eu) through vacuum tube encapsulation followed by 15 hours of melting at 1223 K [18]. Based on their thermoelectric properties, the zT values of AZn_2Sb_2 (A = Sr, Ca, Yb, Eu) were calculated, resulting in maximum values of 0.35, 0.55, 0.4, and 0.9, respectively. Lian Wu et al. synthesized a material composed of $Mg_{3.2}Sb_2$ and $CaZn_2Sb_2$ mixed in a specific ratio using a ball mill process [19]. Based on thermoelectric characterization results depending on the ratio of $Mg_{3.2}Sb_2$ to $CaZn_2Sb_2$, the material with a 1:1 composition exhibited the maximum zT of 0.68 at 773 K. Although many recent studies have reported the evaluation of properties of layered zintl phases with inserted alkali/alkaline earth metals, most of them are synthesized based on ZnSb. As mentioned above, the d_5 and d_{10} transition metals such as Fe and Mn are also expected to exhibit thermoelectric properties, but there are no relevant studies so far despite high potential as TE materials.

In this study, we synthesized FeSb and MnSb-based alloys that can be used for the base materials of advanced TE materials showing layered-zintl-phase. The synthesized FeSb and MnSb ingots were powdered, and subsequently, single-phase materials were successfully identified through XRD analysis. The confirmed single-phase FeSb and MnSb ingots were then polished to size for characterization. The Seebeck coefficient, electrical conductivity, and thermal conductivity of FeSb and MnSb were measured to calculate zT as a function of temperature. The FeSb and MnSb fabricated by arc melting yielded maximum zT values of 0.00026 and 0.00119 at 473 K, respectively. We have successfully investigated TE properties of metal-Sb materials for cation insertion, although these values are somewhat low.

2. Experimental

2.1.Fabrication of Fe-Sb and Mn-Sb Materials

A vacuum arc furnace (VAF) process was used to synthesize transition metal-Sb ingot materials of FeSb and MnSb. The raw materials used were Fe (0.1-1.7 mm, 3N, Kojundo Chemical Laboratory CO., LTD), Mn (2-5 mm, 3N, Kojundo Chemical Laboratory CO., LTD.), and Sb (2-6 mm, 5N, TASCO) shots. Referring to the phase diagrams of Fe-Sb and Mn-Sb [20, 21], the raw materials were weighed in compositions of 56:44 and 52:48 at%, respectively. These weighed raw materials were then placed in the arc melting machine and subjected to 120 V voltage for 5 repeated melting cycles.

2.2. Characterization

The as-synthesized ingots were ground using an induction milling machine and then powdered by filtering the grounds with a 50 μm standard sieve. The as-prepared ingots and powders were analyzed for microstructure and crystalline phase using scanning electron microscopy (SEM, SU-6600, HITACHI) and X-ray diffraction (D/MAX-2500VL/PC, Rigaku). The both ingots were machined to specification by a polishing process for the measurement of electrical conductivity (σ), Seebeck coefficient (S), and thermal diffusivity (D). Thermoelectric properties were measured by using Netzsch's SBA458 Nemesis equipment and laser flash analysis (LFA467 HyperFlash, Netzsch) instruments, respectively, at temperatures ranging from 298 K to 473 K. To calculate thermal conductivity, the density (ρ) of the material was measured by the Archimedes method, and the heat capacity (C_P) was calculated using the Dulong-Petit law ($C_P = 3R/M$) [22-24]. Thermal conductivity (κ) was then calculated using the equation $\kappa = D_\rho C_P$. Additionally, Hall analysis (HMS-5500, ECOPIA) at 298 K was performed to evaluate the carrier concentration (n) and mobility (μ) to analyze the changes in the electrical properties of the ingots.

3. Results and Discussion

Fig. 1(a) illustrates a schematic diagram of the fabrication process of transition metal-Sb materials using the arc melting process, along with actual photographs of the synthesized MnSb and FeSb ingots. The coin-shaped ingots, approximately 20 mm in diameter, were successfully produced by irradiating the raw materials with a high-energy arc, leading to rapid melting, followed by rapid cooling facilitated by a cold Cu plate with flowing coolant. Figs. 1(b) and 1(d) depict the surface microstructure of the samples observed after polishing the MnSb and FeSb ingots, respectively. Both materials underwent repeated rapid melting and cooling, resulting in various internal defects such as pores and cracks. Nevertheless, the EDS mapping results demonstrated that each element such as Fe, Mn, and Sb is uniformly distributed overall. Figs. 1(c) and 1(e) display the XRD patterns of the synthesized powders of MnSb and FeSb,

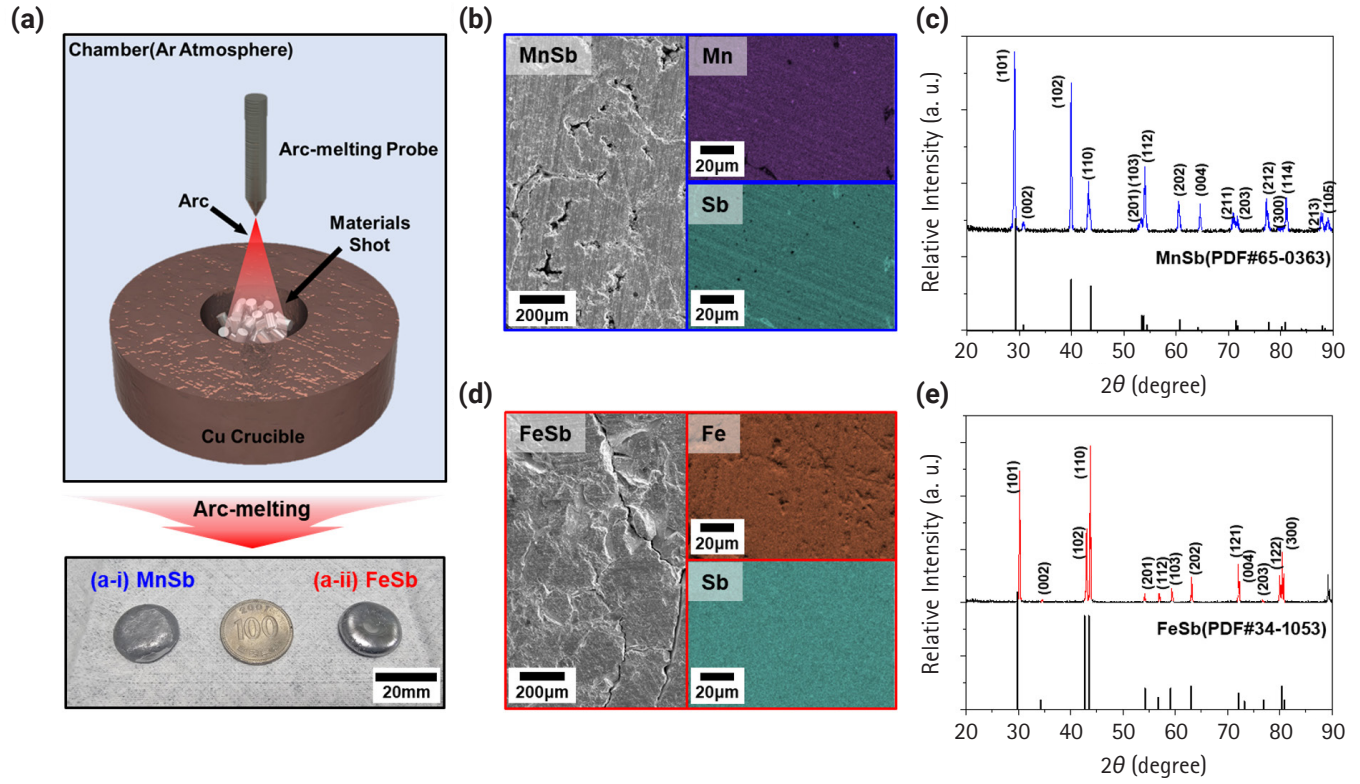

Fig. 1. (a) Schematic illustration of the arc-melting process and a photograph of synthesized MnSb and FeSb ingots. (b, c) Surface scanning electron microscopy (SEM), energy-dispersive spectroscopy (EDS) mapping image, and X-ray diffraction (XRD) patterns of synthesized MnSb. (d, e) Surface SEM, EDS mapping image and XRD patterns of synthesized FeSb.

respectively. According to the phase diagram mentioned in the experimental section [20, 21], the synthesis of single-phase FeSb and MnSb cannot be achieved smoothly when the ratio of Fe/Mn:Sb is 1:1. Materials synthesized with Fe-Sb and Mn-Sb compositions of 56:44 and 52:48 at% reveal good single-phase synthesis compared to the reference PDF card. This result suggests that we have successfully performed the first step for synthesizing a layered zintl phase.

Fig. 2 shows the results of the electrical properties of the ingots as a function of temperature ranging from 298K to 473K. Fig. 2(a) shows the variation of electrical conductivity with temperature for both synthesized FeSb and MnSb. The electrical conductivity of MnSb decreased from 3085 Scm^{-1} to 2145 Scm^{-1} with increasing temperature, exhibiting behavior typical of metals. This result is attributed to the metallic band structure of the majority spin electrons, although MnSb is a semiconductor [25]. Conversely, the electrical conductivity of FeSb increased from 330 Scm^{-1} to 414 Scm^{-1} with increasing temperature, exhibiting behavior typical of semiconductors. This result matches well with studies that FeSb is a semiconductor with a band gap [26]. Fig. 2(b) shows the Seebeck coefficient for both materials, showing a similar trend with negative values, confirming their N-type materials. Moreover, the mobility and carrier concentration of each material at room temperature were evaluated by Hall measurements (Fig. 2(c)). The mobility and carrier concentration of FeSb are 11.4 $cm^2V^{-1}s^{-1}$ and 2.88×10^{20} cm^{-3}, respectively, while those of MnSb are 151 $cm^2V^{-1}s^{-1}$ and 7.31×10^{20} cm^{-3}, respectively. The mobility of MnSb is about 10 times higher than that of FeSb, consistent with the substantial difference in electrical conductivity between the two materials observed in Fig. 2(a). Thus, it is feasibly confirmed that high electrical conducting behaviors of MnSb is due to high carrier concentrations and remarkably increased mobility compared to those of FeSb. Fig. 2(d) shows the calculated power factors based on the measured values of electrical conductivity and Seebeck coefficient, yielding 6.24 and 1.34 $\mu Wm^{-1}K^{-2}$ for MnSb and FeSb at 473 K, respectively.

Fig. 3 shows the comparison of the thermal conductivity of both alloys as a function of temperature. The density measured by the Archimedes method and the C_p value calculated by the Du-

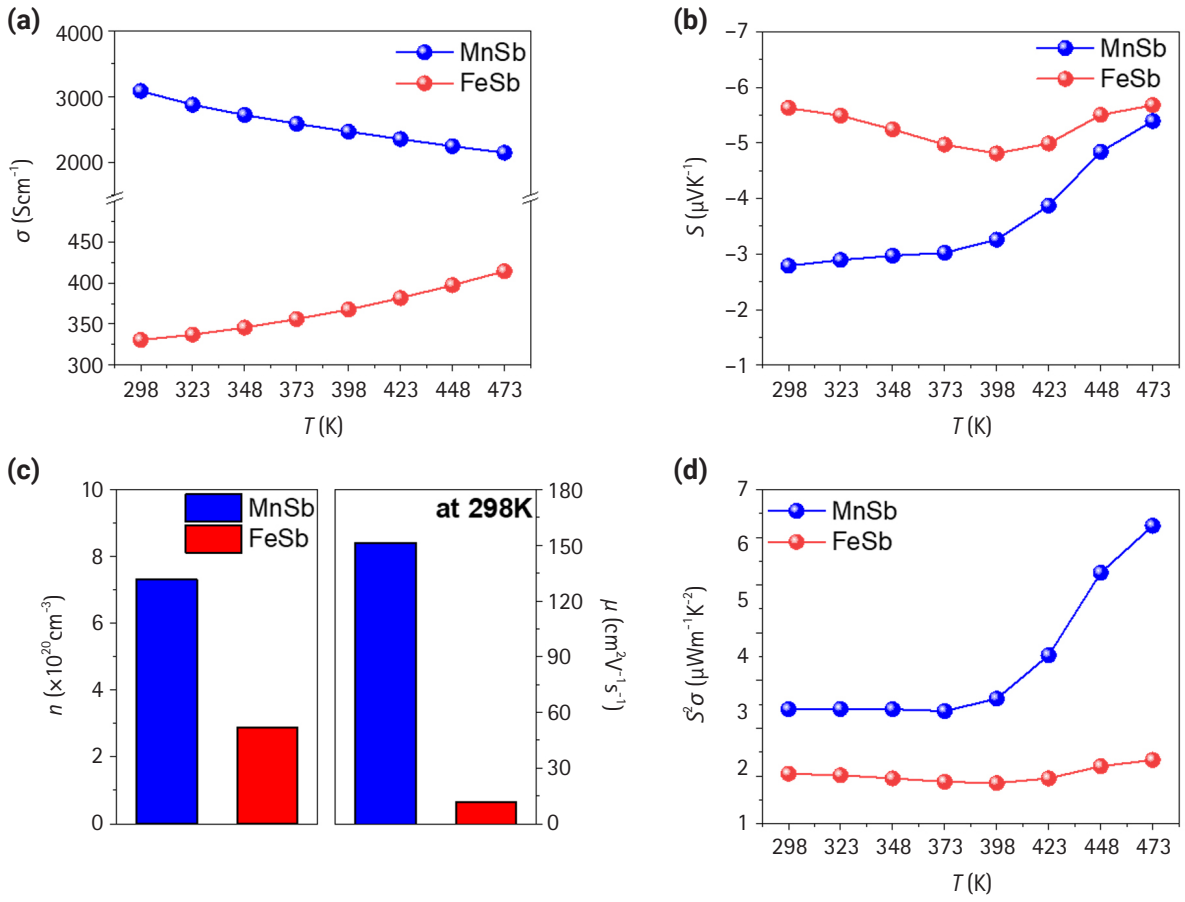

Fig. 2. Thermoelectric properties of MnSb and FeSb: (a) electrical conductivity, (b) the Seebeck coefficient, (c) carrier concentration and mobility, and (d) the power factor.

long-Petit law are presented in Table 1. The maximum thermal conductivity of MnSb was evaluated 2.74 $Wm^{-1}K^{-1}$ at 298 K, while the thermal conductivity of FeSb was evaluated 2.4 $Wm^{-1}K^{-1}$ at 473 K(Fig. 3(a)). These results are consistent with the behavior of the electrical conductivity depicted in Fig. 2(a).

Figs. 3(b) and 3(c) show the contribution of carrier ($\kappa_{e,cal}$) in total thermal conductivity and lattice thermal conductivity ($\kappa_{lat,cal}$) calculated using the following equations.

$$\kappa_{e,\,cal} = L\sigma T$$

$$L = 1.5 + \exp\left(-\frac{|S|}{116}\right)$$

$$\kappa_{tot} = \kappa_{lat,\,cal} + \kappa_{e,\,cal}$$

L is the Lorentz constant, which has units of 10^{-8} $W\Omega K^{-2}$ and was derived based on a computational approximation based on the single parabolic band model [27]. For both materials, a trend of increasing electronic thermal conductivity with rising temperature was observed. In the case of MnSb, the electronic thermal conductivity was calculated to reach up to 2.45 $Wm^{-1}K^{-1}$ as the temperature increased, which closely matched the measured total thermal conductivity at 473 K (2.47 $Wm^{-1}K^{-1}$). The lattice thermal conductivity of MnSb approached almost zero at 473 K, indicating that heat transfer inside the material strongly relies on electrons. That is, in spite of high electrical conductivity, it is analyzed that extremely low lattice thermal conductivity leads to decreasing-tendency of total thermal conductivity of the MnSb. Conversely, the calculated electronic thermal conductivity of the FeSb ingot reached up to 0.48 $Wm^{-1}K^{-1}$ at 473 K, constituting 20% of the total thermal conductivity evaluated in Fig. 3(a). This suggests that heat transfer in FeSb is highly dependent on the carrier rather than lattice phonon-scattering because lattice thermal conductivity shows similar values with increasing temperature. The analysis revealed differences in the primary heat transfer mechanisms with increasing temperature between FeSb and MnSb. MnSb exhibited

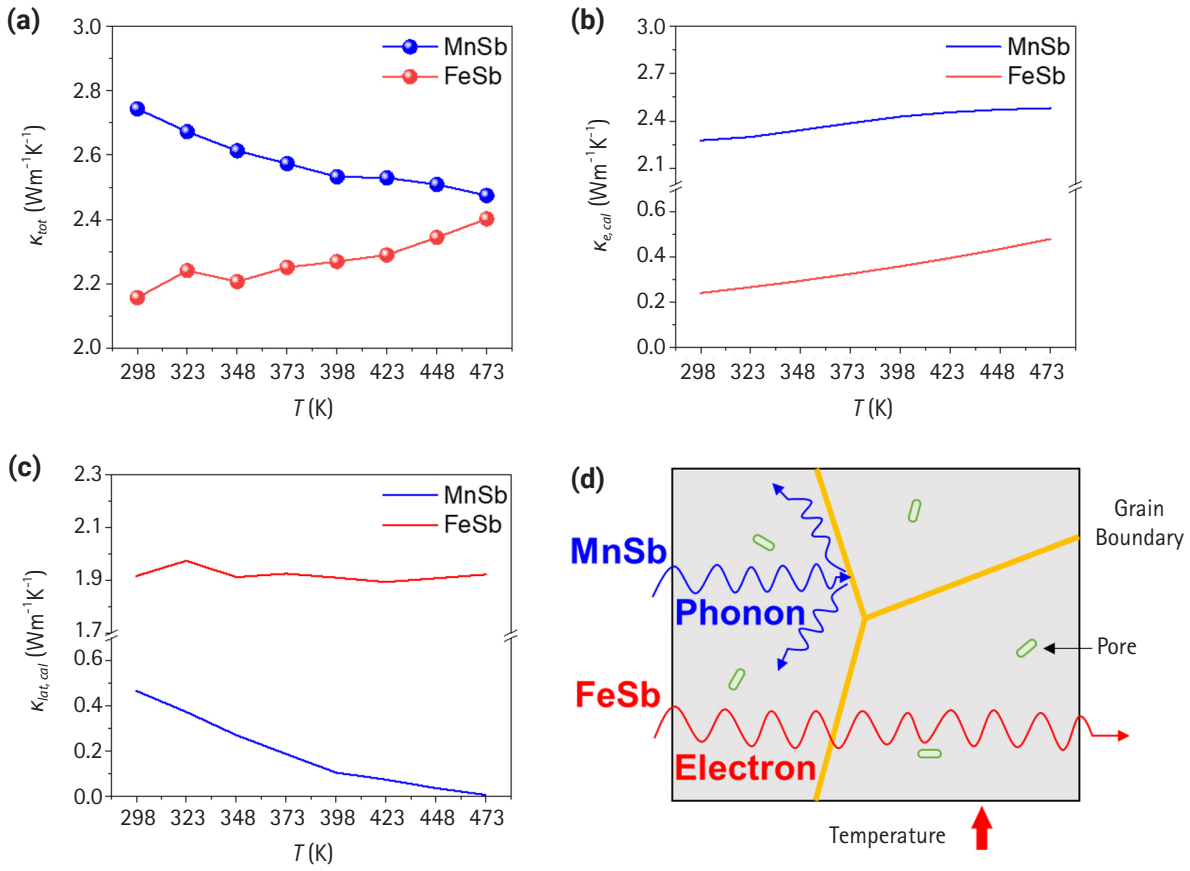

Fig. 3. (a) Total, (b) electronic, (c) and lattice thermal conductivity. (d) Schematic of the main mechanism for thermal conductivity of MnSb and FeSb.

Table 1. A comparison of measured density, calculated theoretical density [28,29], and calculated CP between MnSb and FeSb

Sample	Density (g·cm^{-3})	Theoretical Density (g·cm^{-3})	$C_{P,cal}$ (J·g^{-1}·K^{-1})
MnSb	6.342	6.79	0.141
FeSb	8.059	8.42	0.140

increased phonon scattering with increasing temperature, leading to a reduction in lattice thermal conductivity and an overall decrease in thermal conductivity. On the other hand, FeSb exhibited minimal change in lattice thermal conductivity, but an increase in electronic thermal conductivity due to enhanced carrier mobility, resulting in an overall increase in thermal conductivity (Fig. 3(d)).

Based on the evaluated electrical conductivity, Seebeck coefficient, and thermal conductivity as shown in Figs. 2 and 3, a dimensionless thermoelectric performances (zT) were calculated (Fig. 4). MnSb exhibited higher zT values compared to FeSb in all temperature range, with maximum zT values of 0.00119 and 0.00026 at 473 K, respectively. The maximum zT of MnSb was approximately 4.5 times higher than that of FeSb. Considering our aim in this study to achieve thermoelectric behaviors of two transition metal-Sb alloys as a function of temperature, TE properties of base materials was successfully obtained.

4. Conclusion

In this study, FeSb and MnSb, transition metal-pnictogen materials were synthesized and their fundamental thermoelectric properties were characterized for developing advanced TE materials through cation-insertion in base materials. The XRD patterns of the powderized FeSb and MnSb shows successful synthesis of single-phase materials. Subsequently, thermoelectric property evaluation of the machined single-phase FeSb and MnSb ingots produced zT values of up to 0.00026 and 0.00119

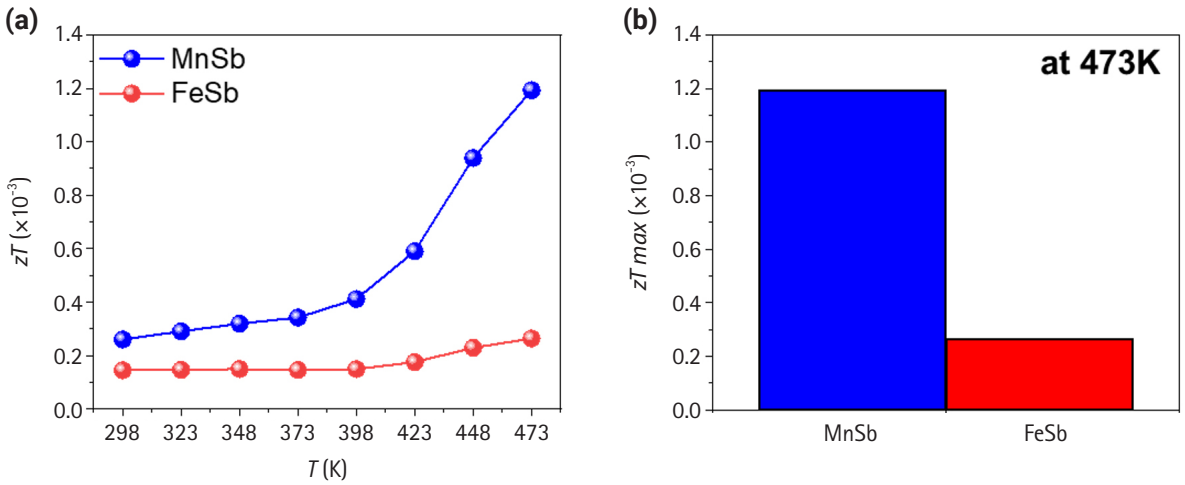

Fig. 4. (a) Temperature-dependent dimensionless figure of merit *zT* and (b) maximum *zT* of MnSb and FeSb.

at 473 K, respectively. The higher mobility observed in MnSb compared to FeSb aligns well with the results indicating high electrical conductivity at 298 K. Despite the relatively low zT values, this investigation into the thermoelectric properties of transition metal-pnictogen materials provides basic information for future advancements in layered zintl phase materials with alkali/alkaline earth metal insertions.

Conflict of Interest Declaration

S. Jo, K. -I. Park, and K. T. Kim serves as an editor of the Journal of Powder Materials editing, but has no role in the decision to publish this article. Except for that, no potential conflict of interest relevant to this article was reported.

Author Information and Contribution

J. M. Park : Ph.D. candidate, Conceptualization, Methodology, Investigation, Data curation, Formal analysis, Visualization, Writing – original draft, S. Jo : Senior researcher, Methodology, Validation, S. Jung : Senior researcher, : Resources, Validation, J. Bae : Senior researcher, Resources, Validation, L. B. Vu : M. S. Candidate, Resources, Validation, K. -I. Park : Professor, Conceptualization, Writing – review & editing, Supervision, Resources, K. T. Kim : Principal researcher, Conceptualization, Writing – review & editing, Supervision, Resources, Funding acquisition, Project administration.

Acknowledgments

This work was supported by the principal R&D program of Korea Institute of Materials Science (Code No. PNK9950) and Bridge-Convergence Technology R&D project (Code No. 2021M3C1C309754021) funded by National Research Foundation of Korea, respectively.

References

[1] S. Jung, Y. J. Woo, K. T. Kim, and S. Jo: J. Powder Mater., **30** (2023) 123.
[2] M. J. Jung, J. Y. Park, S. M. Eun, and B. J .Choi: J. Powder Mater., **30** (2023) 130.
[3] D. Bao, J. Chen, Y. Yu, W. Liu, L. Huang, G. Han, J. Tang, D. Zhou, L. Yang, and Z. Chen: Chem. Eng. J., **388** (2020) 124295.
[4] M. Rull-Bravo, A. Moure, J. F. Fernandez, and M. Martin-Gonzalez: RSC Adv., **5** (2015) 41653.
[5] T.M. Tritt and M.A. Subramanian: MRS Bull., **31** (2011) 188.
[6] A. J. Minnich, M. S. Dresselhaus, Z. F. Ren, and G. Chen: Energy Environ. Sci., **2** (2009) 466.
[7] S. Ohno, A. Zevalkink, Y. Takagiwa, S. K. Bux, and G. J. Snyder: J. Mater. Chem. A., **2** (2014) 7478.
[8] H. Tamaki, H. K. Sato, and T. Kanno: Adv. Mater., **28** (2016) 10182.
[9] T. Yamada, H. Yamane, and H. Nagai: Adv. Mater., **27** (2015) 4708.

[10] L. Borgsmiller, Q. Li, M. Y. Toriyama, and G. J. Snyder: Adv. Energy Mater., **13** (2023) 2300393.
[11] X. Zhang, H. Gu, Y. Zhang, L. Guo, J. Yang, S. Luo, X. Lu, K. Chen, H. Chai, G. Wang, X. Zhang, and X. Zhou: Chem. Eng. J., **374** (2019) 589.
[12] W. Zhang, C. Chen, H. Yao, W. Xue, S. Li, F. Bai, Y. Huang, X. Li, X. Lin, F. Cao, J. Sui, S. Wang, B. Yu, Y. Wang, X. Liu, and Q. Zhang: Chem. Mater., **32** (2022) 6983.
[13] S. Zheng, K. Peng, S. Xiao, Z. Zhou, X. Lu, G. Han, B. Zhang, G. Wang, and X. Zhou: J. Adv. Ceram., **11** (2022) 1604.
[14] J. Song, H. Y. Song, Z. Wang, S. Lee, J. Hwang, S. Y. Lee, J. Lee, D. Kim, K. H. Lee, Y. Kim, S. H. Oh, and S. W. Kim: Sci. Adv., **5** (2019) eaax039.
[15] C. Zheng: J. Solid State Chem., **72** (1988) 58.
[16] B. I. Yoo, N. Lee, B. Lamichhane, J. Bang, H. Y. Song, B. C. Park, K. H. Lee, S. Kim, and S. W. Kim: Adv. Mater., **34** (2022) 2200074.
[17] S. Khan, D. F. Khan, R. Neffati, T. Usman, M. W. Ahsraf, S. Khan, S. U. Jan, and G. Murtaza: J. Rare Earths., **42** (2024) 147.
[18] E. S. Toberer, A. F. May, B. C. Melot, E. Flage-Larsen, and G. J. Snyder: Dalton Trans., **39** (2010) 1046.
[19] L. Wu, Z. Zhou, G. Han, B. Zhang, J. Yu, H. Wang, Y. Chen, X. Lu, G. Wang, and X. Zhou: Chem. Eng. J., **475** (2023) 145988.
[20] D. Boa, S. Hassam, G. Kra, K. P. Kotchi, and J. Rogez: Calphad., **32** (2008) 227.
[21] P. Kainzbauer, K. W. Richter, and H. Ipser: J. Phase Equilib. Diffus., **37** (2016) 459.
[22] D. An, S. Zhang, X. Zhai, W. Yang, R. Wu, H. Zhang, W. Fan, W. Wang, S. Chen, O. Cojocaru-Miredin, X. Zhang, M. Wuttig, and Yu: Nat. Commun., **15** (2024) 3177.
[23] X. Zhang, Z. Bu, X. Shi, Z. Chen, S. Lin, B. Shan, M. Wood, A. H. Snyder, L. Chen, G. J. Snyder, and Y. Pei: Sci. Adv., **6** (2020) eabc0726.
[24] M. T. Ange, P. W. Voorhees, and G. J. Snyder: Adv. Mater., **31** (2019) 1902980.
[25] J. Zheng and W. Davenport: Phys. Rev. B., **69** (2004) 144415.
[26] G. Rahman, S. Cho, and S. C. Hong: J. Magn. Magn. Mater., **304** (2006) e146.
[27] H. Kim, Z. M. Gibbs, Y. Tang, H. Wang, and G. J. Snyder: APL Mater., **3** (2015) 041506.
[28] The Materials Project: MnSb (mp-786). (2023)
[29] The Materials Project: FeSb (mp-2619). (2023)

Research Article

pISSN 2799-8525 · eISSN 2799-8681
J Powder Mater 2024;31(3):243-254

Journal of Powder Materials

Characterization of the Manufacturing Process and Mechanical Properties of CoCrFeMnNi High-Entropy Alloys via Metal Injection Molding and Hot Isostatic Pressing

Eun Seong Kim[1], Jae Man Park[2], Do Won Lee[1], Hyojeong Ha[1], Jungho Choe[1,3], Jaemin Wang[1], Seong Jin Park[2], Byeong-Joo Lee[1], Hyoung Seop Kim[1,4,5,6,*]

[1]Department of Materials Science and Engineering, Pohang University of Science and Technology (POSTECH), Pohang 37673, Republic of Korea
[2]Department of mechanical Engineering, Pohang University of Science and Technology (POSTECH), Pohang 37673, Republic of Korea
[3]Nano Materials Research Division, Korea Institute of Materials Science (KIMS), Changwon, Republic of Korea
[4]Graduate Institute of Ferrous & Eco Materials Technology (GIFT), Pohang University of Science and Technology (POSTECH), Pohang 37673, Republic of Korea
[5]Institute for Convergence Research and Education in Advanced Technology, Yonsei University, Seoul, 03722, Republic of Korea
[6]Advanced Institute for Materials Research (WPI-AIMR), Tohoku University, Sendai 980-8577, Japan

High-entropy alloys (HEAs) have been reported to have better properties than conventional materials; however, they are more expensive due to the high cost of their main components. Therefore, research is needed to reduce manufacturing costs. In this study, CoCrFeMnNi HEAs were prepared using metal injection molding (MIM), which is a powder metallurgy process that involves less material waste than machining process. Although the MIM-processed samples were in the face-centered cubic (FCC) phase, porosity remained after sintering at 1200°C, 1250°C, and 1275°C. In this study, the hot isostatic pressing (HIP) process, which considers both temperature (1150°C) and pressure (150 MPa), was adopted to improve the quality of the MIM samples. Although the hardness of the HIP-treated samples decreased slightly and the Mn composition was significantly reduced, the process effectively eliminated many pores that remained after the 1275°C MIM process. The HIP process can improve the quality of the alloy.

Keywords: High-entropy alloys; Metal injection molding; Hot isostatic pressing; Microstructure; Microhardness

Received: April 15, 2024
Revised: May 13, 2024
Accepted: May 27, 2024

***Corresponding author:**
Hyoung Seop Kim
TEL: +82-54-279-2150
E-mail: hskim@postech.ac.kr

1. Introduction

The hydrogen economy requires the development of materials and processes that exhibit diverse functional properties [1, 2]. High-entropy alloys (HEAs), which have been reported to have better cryogenic properties [3, 4], corrosion resistance [5], and hydrogen embrittlement resistance than commercial materials [6], have attracted attention as candidates to replace existing commercial materials. HEAs are alloys that have changed the concept of conventional alloy design and are single solid-solution phase alloys composed of five or more main elements with maximized compositional entropy [2,3]. Among them, CoCrFeMnNi HEAs in face-centered cubic (FCC) phase with low stacking fault energy (SFE) have been extensively studied in mechanical property as well as in novel process applications [7-9].

However, because CoCrFeMnNi HEAs are relatively expensive in terms of their chemical composition compared to conventional commercial alloys, research is also being conducted to reduce the cost by saving materials or reducing the processing procedure to help commercialize them. Processes reported for the fabrication of CoCrFeMnNi HEAs include casting and forging [10], direct energy deposition [9, 11, 12], powder bed fusion [13, 14], binder jetting additive manufacturing [15], high pressure torsion [16], and metal injection molding [17, 18]. In

https://doi.org/10.4150/jpm.2024.00059

particular, powder metallurgy, especially the sintering process, has the advantage of less material loss and excellent accuracy compared to other processes, making it applicable for mass production [19]. Among the various processes, we focused on 3D shape manufacturing using the feedstock of powders and binders. Similar to the metal additive manufacturing (MAM) process, which produces near-net shaped 3D parts, it is a highly industrial process that eliminates most of the machining procedures, resulting in low material loss [20]. There are two processes for manufacturing 3D-shaped parts using binders with very little loss of powder materials: the binder jetting (BJ) additive manufacturing process [15], which involves layer-by-layer deposition, and the metal injection molding (MIM) process [17-20], which involves injection into a mold in the shape of the parts.

The MIM process is well suited for the mass production of precision parts because it uses a feedstock mix of powder and binder, which is injected into a mold of the target part geometry, followed by debinding and sintering to produce the final parts [20]. In other words, MIM has the advantage of manufacturing precise parts with little material waste, which is attractive because it can reduce the production costs of expensive material processes. Kim et al. [18] fabricated CoCrFeMnNi HEA by MIM process and analyzed their microstructure. However, the MIM process alone makes it difficult to achieve high relative densities due to the residual pores in the part. High porosity and low density are widely recognized to degrade the mechanical properties of parts and are the main reasons for achieving less than expected properties [21]. This means that the MIM process alone leaves pores, which must be removed by an additional process. In the literature, defects in alloys manufactured by powder metallurgy have been effectively removed using hot isostatic pressing (HIP) [22]. HIP process can be used to increase the density and reduce the porosity of HEA fabricated by the MIM process.

In this study, we prepared HEA using the MIM process and attempted to improve their relative densities and porosities using the HIP process. We also investigated the changes in hardness and microstructure under different process conditions.

2. Experimental

2.1. Powder materials

The CoCrFeMnNi HEA powders used in this study were spherical powders prepared via gas atomization (MK Inc., Republic of Korea). The morphology and composition of the powders before the MIM process were measured using the field emission scanning electron microscope (SEM, XL-30S FEG, FEI Co., 5 kV) with the energy dispersive spectrometer (EDS). The particle size distribution (PSD) of the CoCrFeMnNi HEA powders was measured by a laser particle size analyzer (Mastersizer 3000, Malvern), and the median D50 of the powdered material was 86.2 μm (Fig. 1a). The spherical powders were mixed with each element in approximately equal fractions (Fig. 1b).

2.2. MIM process

The feedstock was prepared by mixing the binder and powders. Fig. 2a show that specimens with a width of 20 mm, length of 64 mm, and thickness of 7 mm were injected using a metal injection molding machine (MIM, Sodick, TR30EH). Thermal debinding was performed after solvent debinding to remove the binder. The samples were then sintered at three conditions of 1200 °C, 1250 °C, and 1275 °C. These three conditions were named M1, M2, and M3, respectively (Fig. 2b).

2.3. HIP process

In order to reduce the porosity of the MIM-processed samples, the HIP process was performed at 1150 °C for 4 h under the pressure of 150 MPa (Fig. 3a). Considering the phase diagram simulated by Thermo-Calc software (Database: TCFE2000 and its upgraded version [23-28]), the HIP process conditions were determined to be the temperature at which the FCC phase matrix forms (Fig. 3b). The HIP-treated M1, M2, and M3 were named H1, H2, and H3, respectively (Fig. 3a). In addition, M1, M2, M3, H1, H2, and H3 were all sintered at high temperatures and cooled gradually in the furnace to avoid thermally induced residual stresses and distortions.

2.4. Microstructure characterization & mechanical testing

To analyze the cross-sectional microstructures of the MIM- and HIP-treated samples, SiC sheets of 400, 600, 800, and 1200 grit were used for mechanical polishing, and colloidal silica solution was used for mechanochemical polishing. The cross-sectional morphology was obtained using optical microscopy (OM, BX51M, Olympus, magnification: x50). In addition, SEM was used to analyze the electron backscatter diffraction (EBSD, XL30S, Philips, step size: 1.5 μm, beam: 20 kV) and EDS. The density was measured by Archimedes' principle density balance (XP 205, Mettler Toledo, repeated five times). The mechanical properties were tested using the Vickers hardness machine (FM-700, Future Tech, load: 100 gf, dwell time: 10 s). Vickers hardness was measured eight times at intervals of 2 mm (Fig. 2a show the cross-section view and schematic).

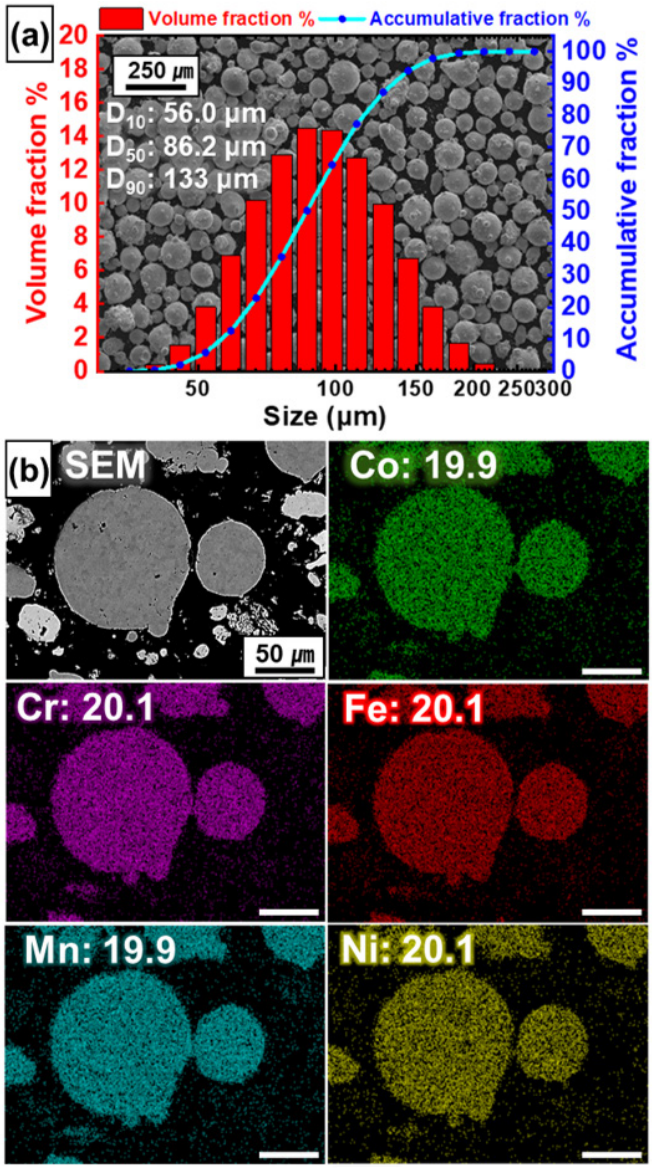

Fig. 1. Spherical powders were prepared for the metal injection molding (MIM) process. (a) Particle size distribution results are superimposed on a scanning electron microscopy (SEM) image of the powders. D10, D50, and D90 are the percentile values of the diameter estimated from the cumulative fraction (%). The median is approximately 86 μm. (b) Cross-sectional SEM-energy-dispersive X-ray spectroscopy (EDS) results of spherical CoCrFeMnNi high-entropy alloy (HEA) powders prepared by gas atomization for process use in MIM. The CoCrFeMnNi HEA can be regarded as having an almost equiatomic chemical composition, with each element measured at about 20 at.% in the EDS.

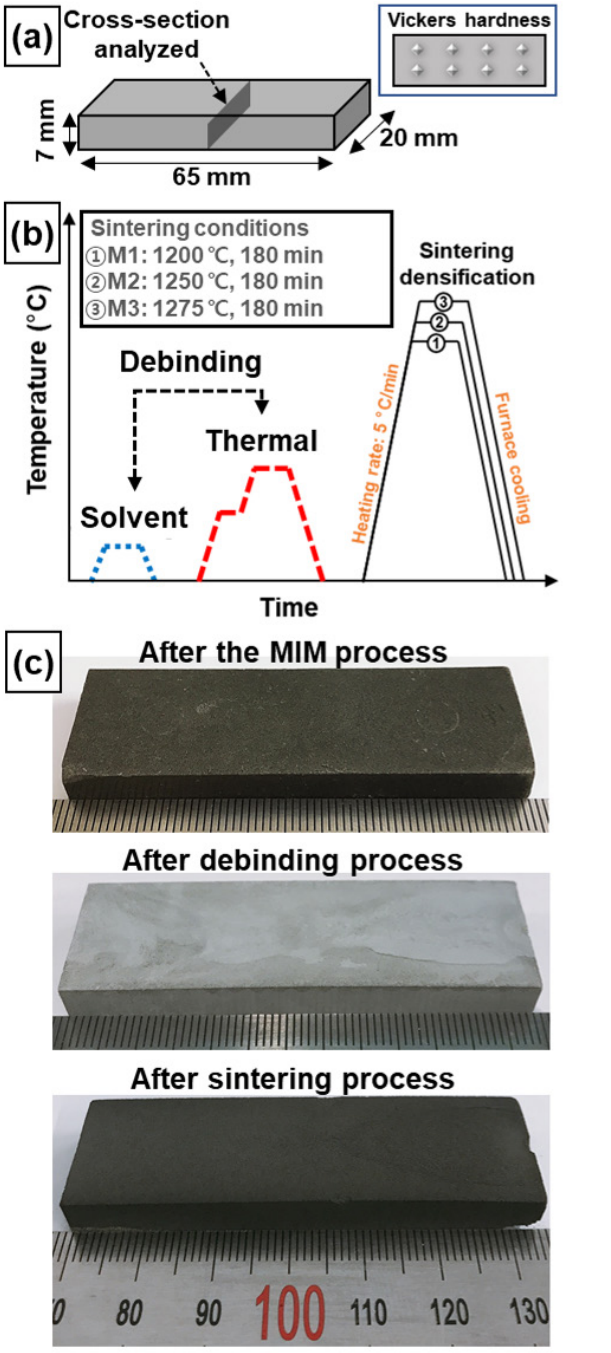

Fig. 2. (a) Schematic diagram of the metal injection molding (MIM). The mechanical properties and microstructure analysis were carried out at the cross-section of the center side. (b) Schematic diagram of post-processing. The MIM parts are processed through debinding to remove the binder materials and compacted through the sintering process. (c) MIM-processed CoCrFeMnNi HEA samples were manufactured by sintering under three different conditions (1200°C, 1250°C, and 1275°C). For more detailed methods of the design and process procedures of MIM conditions, please refer to the previous work [18].

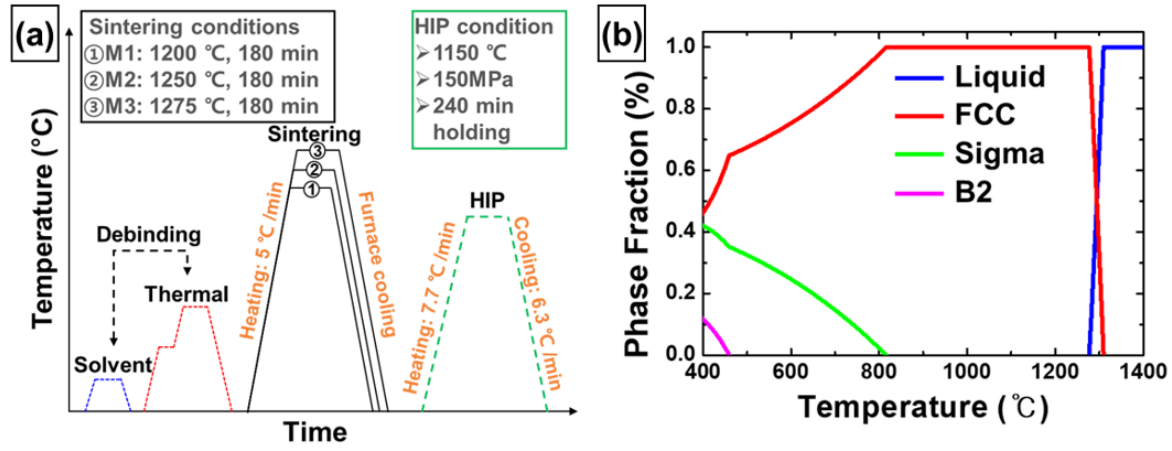

Fig. 3. (a) Schematic diagram of the metal injection molding (MIM) and hot isostatic processing (HIP) processes, showing the difference in process sequence and temperature conditions over time. (b) Equilibrium phase diagram with temperature. The phase diagram was calculated using CALPHAD thermodynamic software, based on the compositions of the powders used in this study.

3. Results and Discussion

3.1. Optical microscopy analysis

Fig. 4 shows the images of the pores observed by OM measurements. The OM analysis of the cross-section shows that the MIM treatment alone on M1 resulted in poor sintering, and features of the powders were observed (Fig. 4a). Because M1 is barely sintered and not in a shape that can be pressurized sintered, the additional HIP treatment has little effect on the pores or morphology (Fig. 4d). In other words, M1 sintered at 1200 °C could not be improved by the HIP. In contrast to M1, for M2 sintered at 1200 °C (Fig. 4b), the pore features formed during sintering were observed (yellow arrows). Fig. 4e shows H2 after HIP treatment of M2, where many of the small pores (yellow arrows) in M2 were significantly removed. Relatively large pores remained, but smaller ones were closed or consolidated into smaller pores (Fig. 4b,e). On the other hand, in contrast to M2, M3 sintered at 1275 °C does not show any relatively small-sized pores (Fig. 4c). Fig. 4f shows H3 after the HIP treatment, and many of the pores (green arrows) in M3 were noticeably removed. Consequently, the large pores in M2 were significantly removed and H3 became closed pores with irregular shapes.

3.2. Microhardness with the grain size

Fig. 5 shows the porosity analyzed by OM and the density measured by Archimedes' method before and after HIP treatment for relative comparison analysis. Considering the porosity and relative density (Figs. 4, 5), M2 has a porosity of 24.1% and a relative density of 85.2% (6.778 g/cm^3), while H2 has a porosity of 7.03% and a relative density of 89.1% (7.09 g/cm^3). Fig. 4b,e intuitively shows that the density increased with porosity improvement (the yellow arrow that disappeared in M2 corresponds to the porosity that disappeared in H2). Similarly, M3 had a porosity of 14.1% and a relative density of 87.8% (6.989 g/cm^3), whereas H3 had a porosity of 2.99% and a relative density of 90.5% (7.201 g/cm^3). Fig. 4c,f show that the pores in M2 (green arrows) are significantly removed in H3. The porosity of M3 was significantly reduced, indicating that the density of H3 was significantly improved.

Fig. 5 show the hardeness measured by Vickers Hardness test. Because enhanced density and porosity cannot explain the reduction in hardness, another major microstructural factor, grain size, must also be considered [21, 29]. Fig. 6i-l show the kernel average misorientation (KAM) maps estimated using EBSD. The KAM value is an effective way to show the tendency of the dislocation-based strain distribution [9,30-32]. Because M2 and M3, as well as H2 and H3, were processed at high temperatures and cooled gradually, the average KAM values did not differ significantly. This KAM analysis allowed us to analyze the effect of grain size and grain boundaries on hardness more clearly, without considering the main microstructural factors of dislocations.

Fig. 5 shows the change in hardness before and after the HIP treatment. Although the density and porosity of M2 improved in H2, the hardness decreased slightly from 174 ± 14 Hv to 162 ± 11 Hv. According to the Hall-Petch relationship [33, 34], the relationship between the average grain size and yield strength can be found, and according to the Tabor relationship

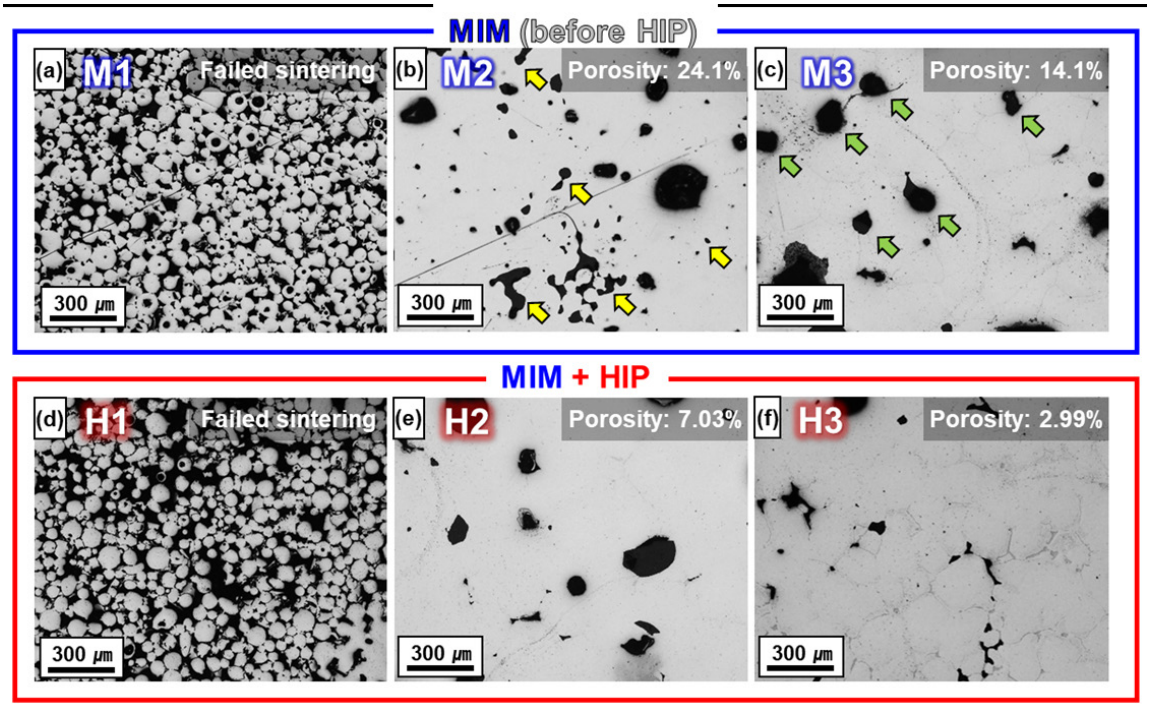

Fig. 4. The optical microscopy (OM) images are divided into before (a-c) and after (d-f) hot isostatic processing (HIP). MIM processed at (a) 1200°C is M1, (b) 1250°C is M2, (c) 1275°C is M3. HIP processed under 1150°C/4h using (d) M1 is H1, (e) M2 is H2, (f) M3 is H3. Porosity was calculated using OM and image processing software (ImageJ, version 1.51j). The M1 and H1 samples are failed conditions because the sintering processes were not complete. M2 was observed with small or irregularly shaped pores (yellow arrows).

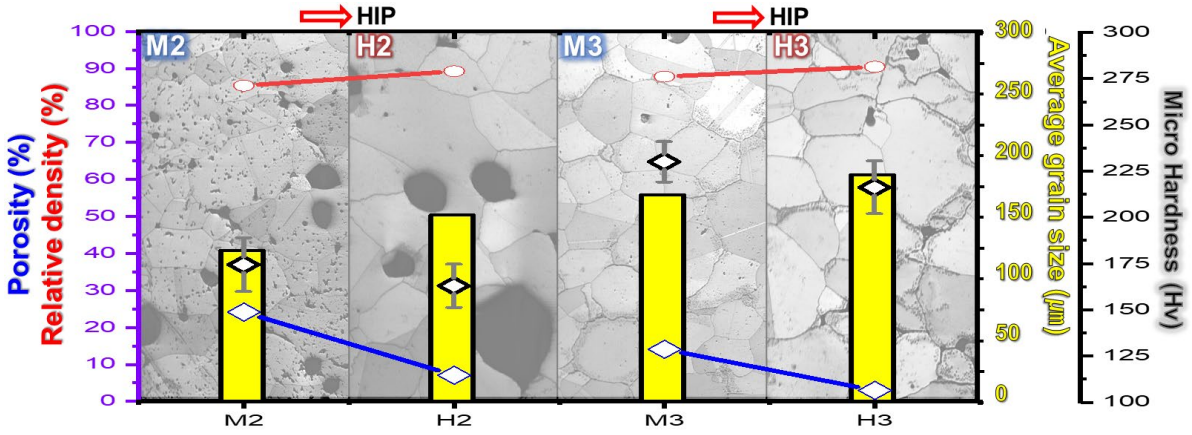

Fig. 5. Microstructure analysis and mechanical properties superimposed on electron backscatter diffraction (EBSD)-IQ maps considering the pore shapes and grain boundaries. From the superimposed graphs, the changes in relative density, porosity, and average grain size and micro-hardness after HIP treatment are compared. Porosity was calculated using optical microscopy (OM) and image processing and the density was measured by Archimedes' principle of density balance.

[33, 35], the relationship between yield strength and hardness can be found. The relationship expression that considers the above two relationships is summarized in Eq. (1).

$$\sigma_y = 9.81 * \frac{Hardness}{3} = \sigma_0 + \frac{k_y}{\sqrt{d}} \quad (1)$$

Where σ_y is the yield strength, σ_0 is the material constant for dislocation movement, k_y is the strengthening coefficient, and d

is the average grain size. In general, in metallic materials, grain boundaries typically function as fixed points and obstruct the propagation of dislocations [36]. The increase in grain size equals the decrease in grain boundary fraction, and we can see that grain size and hardness are inversely proportional, meaning that the increase in grain size from 123 μm to 152 μm due to the HIP treatment is likely responsible for the decrease in hardness. Similarly, the hardness of M3 was 230 ± 11 Hv, which was slightly reduced to 216 ± 14 Hv in H3 after HIP treatment. Considering Equation 1 together, the average grain size of H3 increased from 168 μm to 184 μm with the HIP treatment, which contributed to the decreased hardness.

3.3. Microstructure and chemical composition

For microstructure analysis, IQ-inverse pole figure (IPF) maps were obtained by EBSD based on the (100) crystal plane (Fig. 6a-d). The color difference in the IPF map indicates which crystal direction each grain is oriented, and is a useful analysis method that can effectively distinguish the texture of the metallic materials [9, 18, 31, 37]. Because neither the MIM sintering nor the HIP treatment induced anisotropy, the grains were grown as homogeneously textured, equiaxed grains that were not oriented.

The IQ-phase maps show that the FCC phase is organized in the matrix for all conditions before and after HIP process (Fig. 6e,h). Considering the thermodynamic equilibrium diagram (Fig. 3b), it is possible to have B2 and sigma phases besides the FCC phase, as furnace cooling will unavoidably pass through temperatures with different stable phases [17, 30]. However, during the sintering process, the elements segregated towards the grain boundaries have a different composition from that of the initial powder, which can also lead to different phases [38]. The composition analyzed by EDS shows that in H2, M3, and H3, the elements Cr, Ni, and Mn have inhomogeneous distributions (Fig. 7). However, considering the Mn content of 19.9 at.% in the initial powders, M2 and M3 fabricated by the MIM process showed the decrease in Mn content of about 3-4 at.%, while H2 and H3, which were subjected to HIP treatment, showed the additional decrease in Mn content of about 8-10 at.%. The reduced Mn content can be attributed to two factors [39]. First, the high-temperature sintering in the vacuum atmosphere in MIM process resulted in more evaporation of Mn, which has the relatively low melting point compared to other elements (Co, Cr, Fe, Ni), and the HIP treatment in an Ar atmosphere with accompanying pressure accelerated the evaporation of Mn. Second, the reduction of Mn is assumed to be formed due to the inevitable oxidation during the MIM and HIP processes. Also, Fig. 7, the distribution of O is consistent with that of Mn. Manganese oxide is mainly observed around the voids, and the Mn content of the matrix decreased in proportion to the manganese oxide formed.

The IQ-phase maps show that the FCC phase was organized in the matrix for all conditions before and after the HIP process (Fig. 6e,h). Considering the thermodynamic equilibrium phase diagram (Fig. 3b), it is possible to have B2 and sigma phases in addition to the FCC phase because furnace cooling will inevitably pass through temperatures with different phases [17, 30]. However, during the sintering process, the elements segregated towards the grain boundaries have a different composition from that of the initial powder, which can also lead to different phases [8, 38]. For H2, M3, and H3, the compositional distributions analyzed by EDS show the inhomogeneity of Cr, Ni, and Mn along the grain boundaries (Fig. 7). However, considering the Mn content of 19.9 at.% in the initial powders, M2 and M3 fabricated by the MIM process showed a decrease in Mn content of approximately 3-4 %p, while H2 and H3, which were subjected to HIP treatment, showed an additional decrease in Mn content of approximately 8-10 %p. The reduced Mn content could be attributed to two factors [39]. First, high-temperature sintering in the vacuum atmosphere in the MIM process resulted in more evaporation of Mn, which has a relatively low melting point compared to other elements (Co, Cr, Fe, and Ni), and the HIP treatment in an Ar atmosphere with accompanying pressure accelerated the evaporation of Mn. Second, the reduction of Mn is assumed to occur owing to the inevitable oxidation during the MIM and HIP processes. Plus, Fig. 7 shows that the distribution of O was consistent with that of Mn. Manganese oxide was mainly observed around the voids, and the Mn content of the matrix decreased in proportion to the manganese oxide formed.

In addition, HEAs have a low SFE, an alloy in which twinning is activated by annealing or deformation [40]. The twin boundary fraction (TBF) increased to 22.7% in M2 and 27.7% in H2 (yellow boundaries in Fig. 6e,f). Furthermore, Ni and Mn, the main elements in CoCrFeMnNi HEAs, are typical FCC phase-stabilizing elements, and it can be inferred that the reduced Mn induces the matrix to be less phase-stabilized to FCC, further enabling twinning. On the other hand, in contrast to H2, TBF decreased slightly in H3 to 15.1% (M3) and 12.5% (H3) (Fig. 6g,h).

Considering the average chemical composition (Fig. 7), this is not convincing because the trend of the global chemical

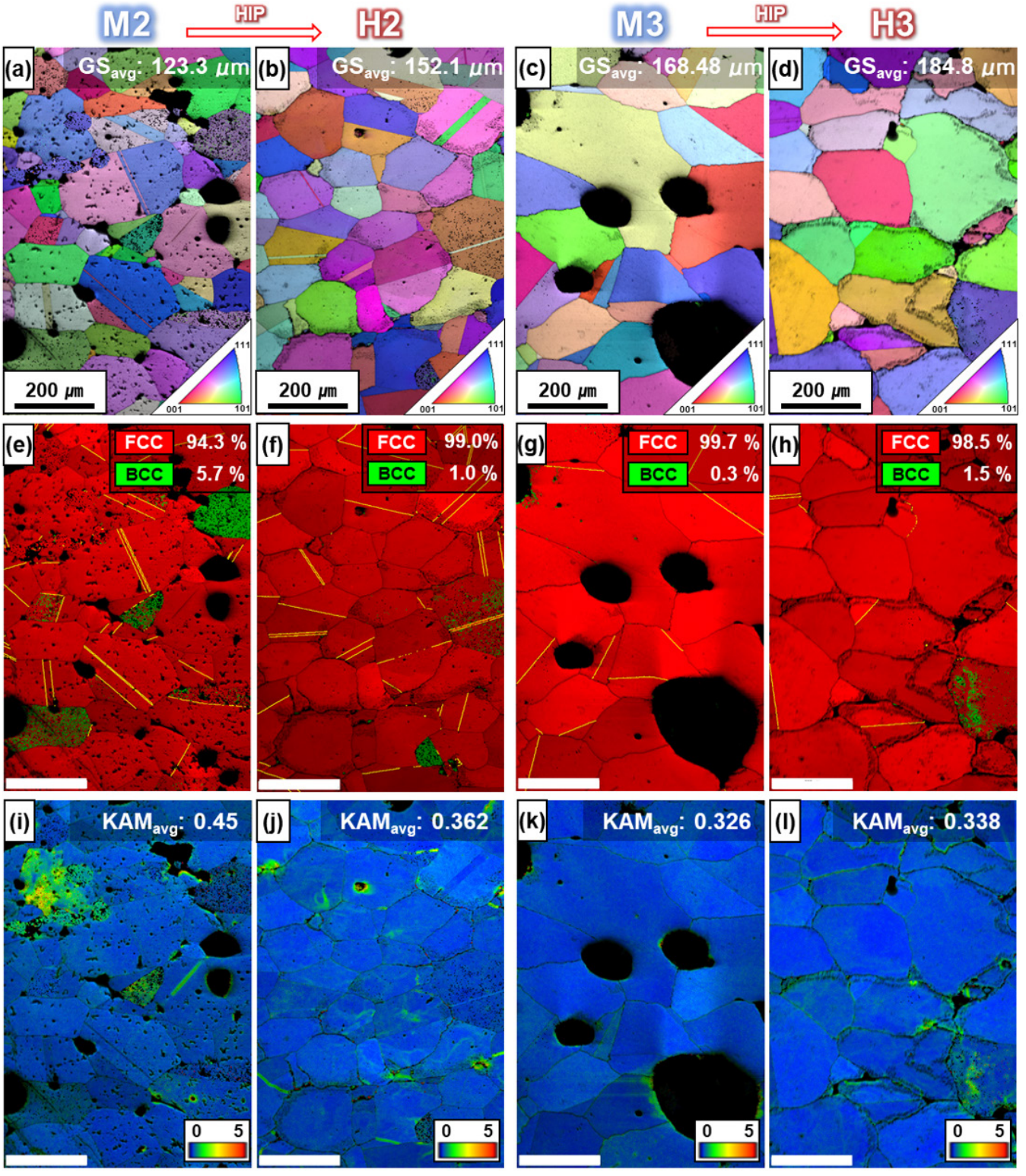

Fig. 6. Scanning electron microscopy– electron backscatter diffraction (SEM-EBSD) maps of M2, M3, H2, and H3. The grain boundary color of all maps is black. (a-d) EBSD–inverse pole figure (IPF) map. No anisotropies were observed under any conditions. (e-h) EBSD-phase map. The yellow boundaries are twin boundaries of the Δ3 type in the face-centered cubic (FCC) phase. (i-l) EBSD– kernel average misorientation (KAM) map. Maximum orientation: 5° with the third nearest neighbor kernel.

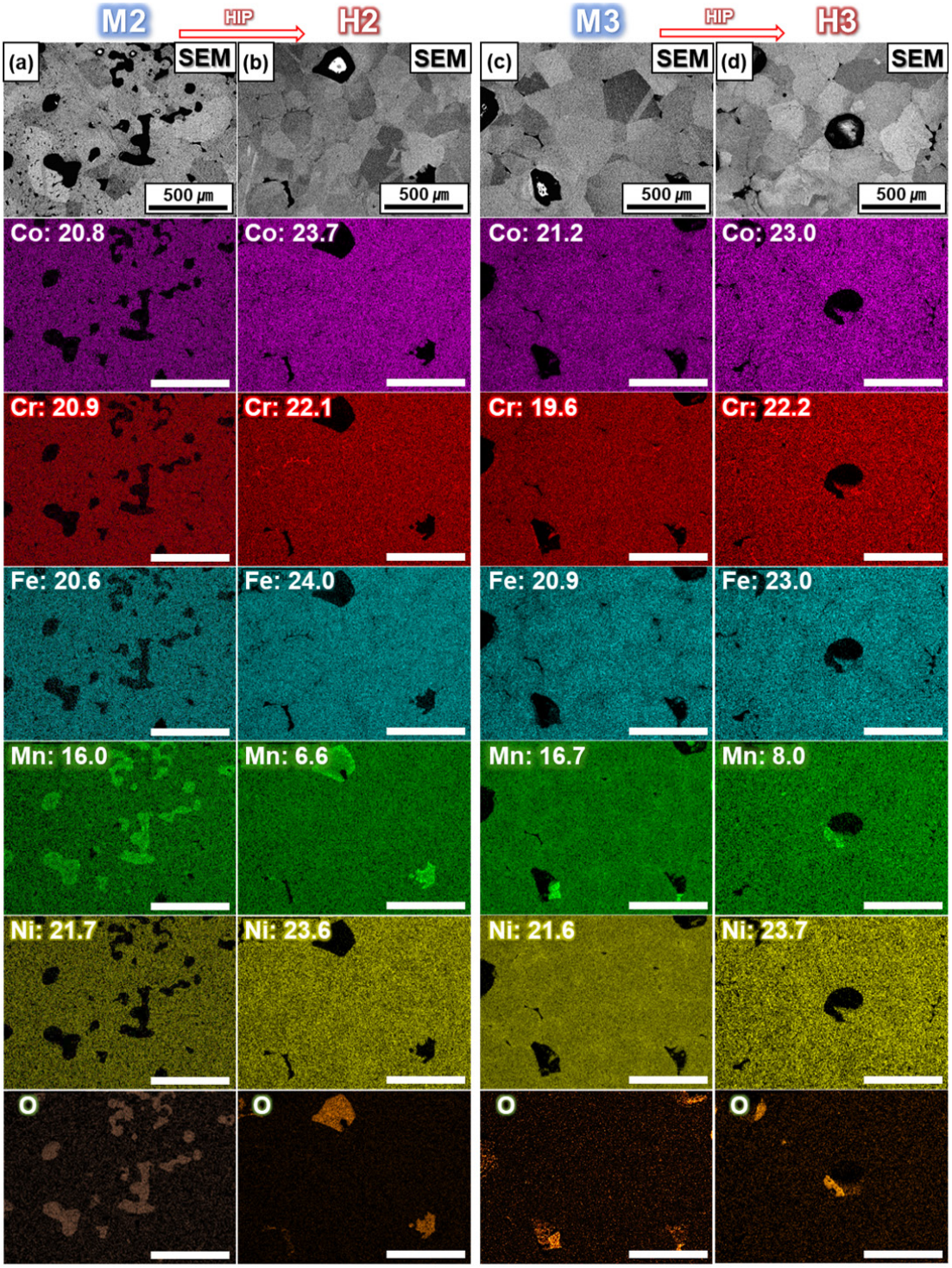

Fig. 7. Scanning electron microscopy–energy-dispersive X-ray spectroscopy (SEM-EDS) maps of (a) M2, (b) M3, (c) H2, and (d) H3. (a) M2, the metal injection molding (MIM)-processed sample, was insufficiently sintered, and numerous areas of manganese oxide were observed along the pores. (b) H2 results after HIP treatment of M2, showing more sintering than M2, enrichment in Cr along the grain boundaries, and deficiency in Fe and Co. (c) MIM sample M3, unlike M2, is significantly sintered and is enriched in Cr, Mn, and Ni along the grain boundaries and deficient in Fe and Co. (d) Compared to M3, HIP-treated H3 has a homogeneous composition distribution with sufficient diffusion of Fe, Ni, and Mn, and Cr during the hot isostatic pressing (HIP) process is abundantly distributed around the grain boundary, similar to H2. In addition, the O maps of all conditions showed numerous oxides. This suggests that oxidation was unavoidable for both MIM and HIP, even when they were prepared under an inert atmosphere.

composition changed by the HIP process for both H2 and H3 is similar. However, the Co-Cr-Fe-Mn-Ni system is an alloy in which phases other than FCC appear when the composition of each element varies [40]. In other words, the chemical composition is strongly related to the stability of either the FCC or BCC phases.

Fig. 8 shows the SEM-EDS line profile results obtained near the grain boundary, and the chemical composition distributions of H2 and H3 were different. Both the HIP-treated H2 and H3 precipitated Cr-rich phases at the grain boundaries. The Cr-rich phase formed by heat treatment is the BCC phase near the grain boundary [17, 41], and the precipitated BCC phase is more distributed in H3 than in H2. In other words, Cr functions as a BCC stabilizer [42, 43], which increases the FCC stability of the matrix. Table 1 shows the average chemical composition of the matrix region as measured by EDS, showing that Cr in the matrix is more depleted in H3.

Thermodynamically simulated Gibbs free energy (G) with matrix composition also supports this evidence (Software: Thermo-Calc, Database: TCFE2000 and its upgraded version

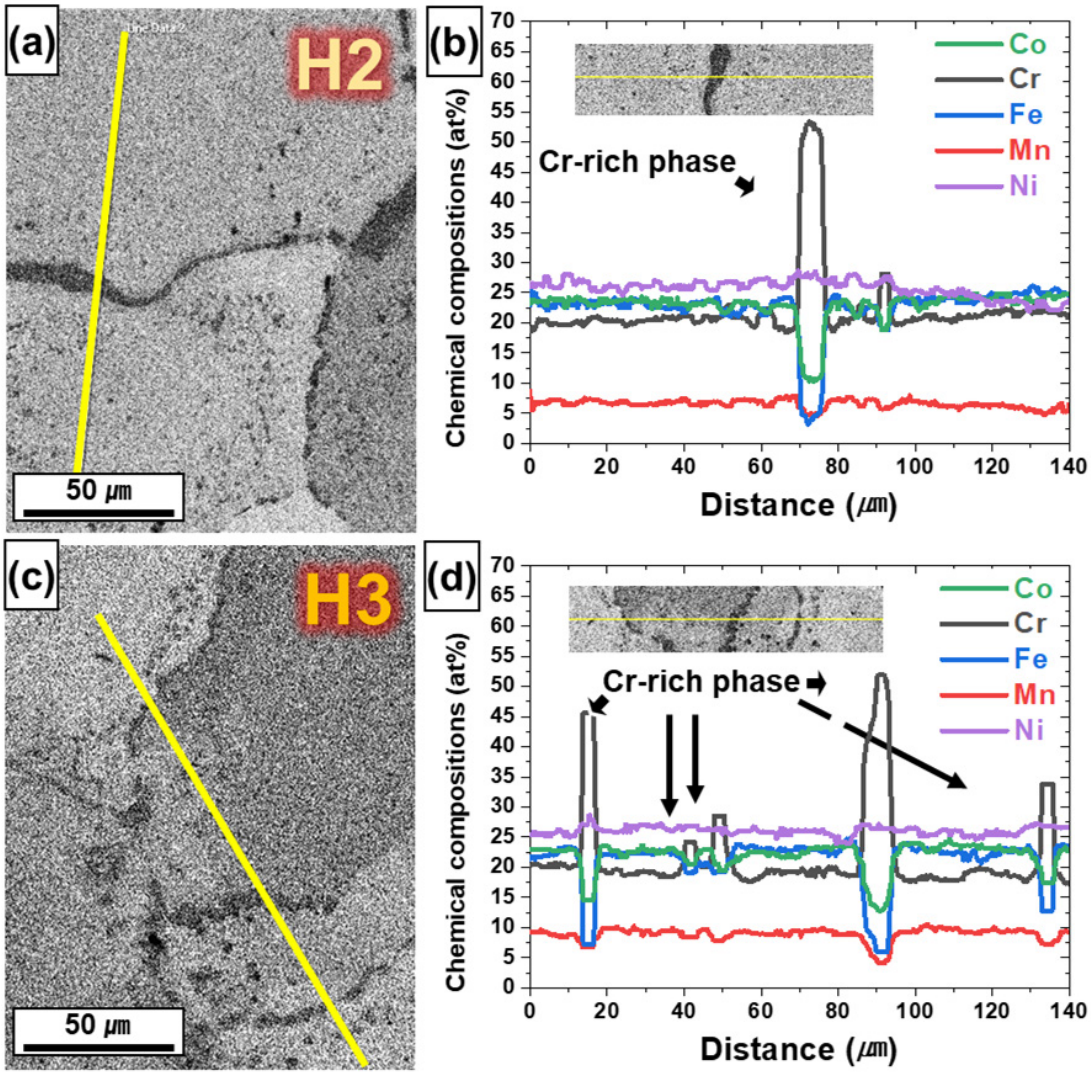

Fig. 8. Scanning electron microscopy–energy-dispersive X-ray spectroscopy (SEM-EDS) line profile results. (a) High-magnification SEM image of H2 and EDS line-profile analysis along the yellow line across the grain boundary. (b) H2 shows a composition with severe segregation of Cr along the grain boundary. The Cr-rich phase is a precipitate phase composed mainly of body-centered cubic (BCC) structures, whereas the composition of the matrix is lower than the average in Cr. (c) Location of the EDS line profile of H3. (d) H3 also shows a composition with severe segregation of Cr along the grain boundary. In addition, many Cr-rich phases were observed around the grain boundaries. The matrix had a more Cr-deficient composition than that of H2.

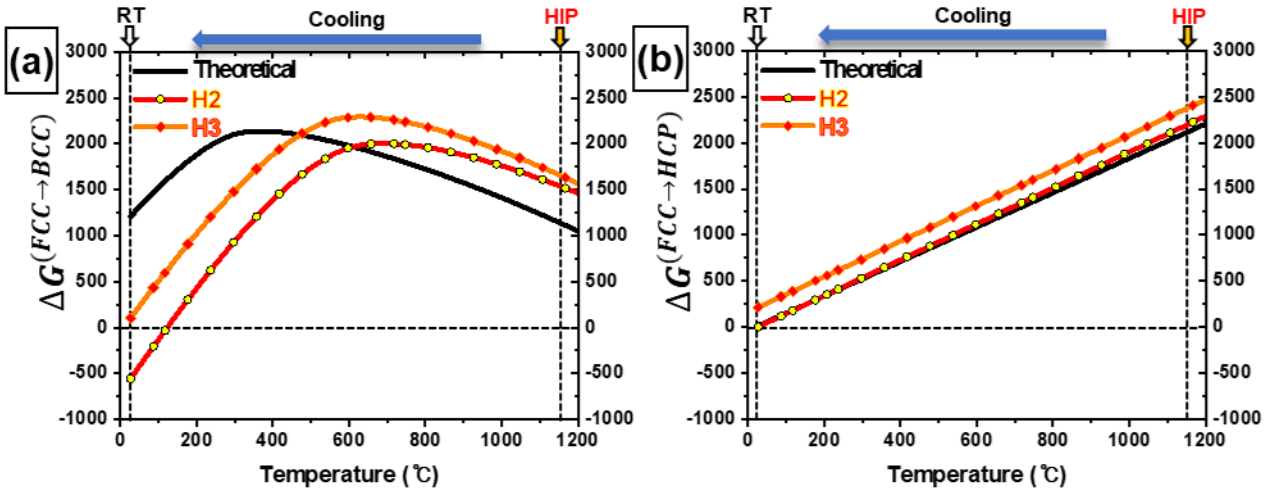

Fig. 9. Gibbs free energy was calculated by CALPHAD thermodynamic software at the pressure condition of 150 MPa based on the compositions of the H2 and H3 matrix (Table 1 shows chemical compositions). Gibbs energy change after hot isostatic pressing (HIP) treatment considering cooling (1150 °C→25 °C): (a) ΔG (FCC to BCC) and (b) ΔG (FCC to HCP). The positive ΔG value indicates that the FCC phase is stable. FCC, face-centered cubic; BCC, body-centered cubic; HCP, hexagonal close-packed.

[23-28]). *G* is a useful means of expressing the phase stability, where the phase with the lowest negative value can be described as the stable phase [41, 42]. Fig. 9 shows the results of *G* for the phase stability simulated at 150 MPa, mimicking the HIP process conditions. For comparative analysis, we reconstructed the simulated stability of each phase in terms of *G* difference (△ *G*) in Eq. (1,2).

$$\Delta G^{(FCC\rightarrow BCC)} = G^{BCC} - G^{FCC}\ [J/mol] \quad (2)$$

$$\Delta G^{(FCC\rightarrow HCP)} = G^{HCP} - G^{FCC}\ [J/mol] \quad (3)$$

A positive $\triangle G$ is indicates that the FCC phase is stable and a negative $\triangle G$ indicates that the FCC phase unstable. In other words, when the energy barrier is overcome ($\triangle G = 0$), it becomes phase transformation. At the HIP treated temperature (1150 °C), $\triangle G^{(FCC\rightarrow BCC)}$ of H3 is 1686 J/mol, which is greater than H2 (1563 J/mol) (Fig. 9a, Table 1). Similarly, $\triangle G^{(FCC\rightarrow HCP)}$ shows the same trend (H3: 2349, H2: 2168) as $\triangle G^{(FCC\rightarrow BCC)}$ (Fig. 9b, Table 1). Moreover, H3 was greater than H2 at all temperatures. Taken together, these results suggest that although it forms a single FCC phase at elevated temperatures and changes to the metastable FCC phase during cooling to room temperature (RT), H3 is more stable than H2 at all temperatures, which is consistent with the trend of the TBF of H2 (27.7 %) being greater than that of H3 (12.5 %), suggesting that H3, which is more depleted in Cr than H2, is a more stable FCC phase than H2.

This means that the TBF difference is inferred to be influenced more by the MIM processing temperature. The difference in TBF due to HIP treatment was ~4%p (M2 and H2) and ~3%p (M3 and H3), while the difference in TBF due to the difference in sintering temperature of the MIMs was ~7%p (M2 and M3). Considering all the SEM-EDS images (Fig. 7), the influence of the secondary phases cannot be ruled out. The annealed twins of HEA in the FCC matrix can be attributed not only to the chemical composition (distribution changed by Mn

Table 1. The chemical compositions of the FCC matrix as measured by EDS. (at.%) The Gibbs energy was calculated using the CALPHAD thermodynamic software (Fig. 9 shows Gibbs energy simulations under 150 MPa considering H2 and H3). FCC, face-centered cubic; EDS, energy-dispersive X-ray spectroscopy; BCC, body-centered cubic; HCP, hexagonal close-packed.

	Average chemical composition of FCC matrix (at.%)					ΔG (J/mol)	
	Co	Cr	Fe	Mn	Ni	FCC to BCC	FCC to HCP
Theoretical	20.0	20.0	20.0	20.0	20.0	1169	2088
H2	24.13	20.69	23.34	6.10	25.56	1563	2168
H3	23.70	17.86	22.51	9.72	26.06	1686	2349

evaporation during HIP treatment), but also to the temperature influence of the MIM process (difference between M2 and M3, matrix composition, and BCC phase).

In this study, the MIM-processed HEA prepared at different temperatures were further subjected to the HIP process to improve the porosity, and the hardness and microstructure differences of the MIM samples before and after HIP treatment were analyzed. In the future, we will perform thermodynamic calculations considering temperature and pressure to propose further improved process conditions and fabricate improved FCC single-phase HEA components to analyze the influence of the microstructure on the mechanical deformation behavior.

4. Conclusion

In this study, CoCrFeMnNi HEA samples were fabricated by metal injection molding (MIM) process and hot isostatic pressing (HIP) treatment. The hardness, density, porosity, and microstructure of the HIP-treated HEA were investigated and the following conclusions were obtained:

1) After the HIP treatment, the average grain size increased and the hardness decreased, but the porosity was significantly reduced and the density increased, which improved the quality.
2) Both MIM and HIP processes resulted in Mn composition changes; the composition of Mn decreased slightly after the MIM process and decreased significantly after the HIP process. Manganese oxide was observed in all samples during cooling of the heat treatment, and precipitation on Cr-rich BCC could not be avoided.
3) The annealing twin changes slightly (3-4%p) after HIP treatment, but a more dominant change (8-10%p) can be seen with the difference in sintering temperature of the MIMs, which is due to the change in composition during the process and the influence of the precipitation phases.

In order to contribute to the manufacturing of commercial HEA components, future work should not only study the microstructure under different process conditions, but also the effect of microstructure on the mechanical deformation behavior.

Conflict of Interest Declaration

The authors declare no competing financial interests or personal relationships.

Author Information

Eun Seong Kim, Do Won Lee, Hyo Jeong Ha: Student, Jae Man Park Jungho Choe, Jaemin Wang: Researcher, Seong Jin Park, Byeong-Joo Lee, Hyoung Seop Kim: Professor

Acknowledgments

This work was supported by the National Research Foundation (NRF) of the Republic of Korea (2021R1A2C3006662 and 2022R1A5A1030054). Eun Seong Kim is also supported by Basic Science Research Program through the National Research Foundation of Korea (NRF) funded by the Ministry of Education (2022R1A6A3A13073830).

References

[1] M. Yue, H. Lambert, E. Pahon, R. Roche, S. Jemei, and D. Hissel: Renew. Sustain. Energy Rev., **146** (2021) 111180.
[2] B. Gludovatz, A. Hohenwarter, D. Catoor, E. H. Chang, E. P. George, and R. O. Ritchie: Science., **6201** (2014) 1153.
[3] E. P. George, D. Raabe, and R. O. Ritchie: Nat. Rev. Mater., **4** (2019) 515.
[4] H. Luo, Z. Li, W. Lu, D. Ponge, and D. Raabe: Corros. Sci., **136** (2018) 403.
[5] Y. Fu, J. Li, H. Luo, C. Du, and X. Li: J. Mater. Sci. Technol., **80** (2021) 217.
[6] Z. Pu, Y. Chen, and L. H. Dai: Mater. Sci. Eng. A., **736** (2018) 156.
[7] R. B. Mane, R. Y, and B. B. Panigrahi: Powder Metallurgy., **61** (2018) 131.
[8] F. Otto, A. Dlouhý, K. G. Pradeep, M. Kuběnová, D. Raabe, G. Eggeler, and E. P. George: Acta Mater., **112** (2016) 40.
[9] E. S. Kim, K. R. Ramkumar, G. M. Karthik, S. G. Jeong, S. Y. Ahn, P. Sathiyamoorthi, H. Park, Y. -U. Heo, and H. S. Kim: J. Alloys Compd., **942** (2023) 169062.
[10] J. H. Kim, K. R. Lim, J. W. Won, Y. S. Na, and H.-S. Kim: Mater. Sci. Eng. A., **712** (2018) 108.
[11] G. H. Gu, E. S. Kim, H. Kwon, S. Son, R. E. Kim, T. K. Oh, and H. S. Kim: Mater. Sci. Eng. A., **836** (2022) 142718.
[12] S. Y. Ahn, D. G. Kim, J. A. Lee, E. S. Kim, S. G. Jeong, R. E. Kim, S.-J. Hong, P. Quang, S. Lee, and H. S. Kim: J. Alloys Compd., **960** (2023) 170602.
[13] A. Piglione, B. Dovgyy, C. Liu, C. M. Gourlay, P. A. Hooper, and M. S. Pham: Mater. Lett., **224** (2018) 22.
[14] G. M. Karthik, Y. Kim, E. S. Kim, A. Zargaran, P. Sathiya-

moorthi, J. M. Park, S. G. Jeong, G. H. Gu, A. Amanov, T. Ungar, and H. S. Kim: Addit. Manuf., **59** (2022) 103131.
[15] Z. Xu, Z. Zhu, P. Wang, G. K. Meenashisundaram, S. M. L. Nai, and J. Wei: Addit. Manuf., **35** (2020) 101441.
[16] G. M. Karthik, P. Asghari-rad, P. Sathiyamoorthi, A. Zargaran, E. S. Kim, T. S. Kim, and H. S. Kim: Scr. Mater., **195** (2021) 113722.
[17] Y. Zhang, T. Bian, X. Shen, Z. Wang, S. Ye, S. Feng, K. Yu, C. Ding, and P. Yu: J. Alloys Compd., **868** (2021) 158711.
[18] E. S. Kim, J. M. Park, J. S. Lee, J. Choe, S. Y. Ahn, S. G. Jeong, D. W. Lee, S. J. Park, and H. S. Kim: J. Powder Mater., **30** (2023) 1.
[19] A. O. Araoyinbo, F. A. Ishola, E. Y. Salawu, M. B. Biodun, and A. U. Samuel: AIP Conf. Proc., **2437** (2022) 020153.
[20] S. V. Atre, T. J. Weaver, and R. M. German: Injection Molding of Metals and Ceramics, SAE Technical Paper (1998) 982417.
[21] F. Ternero, L. G. Rosa, P. Urban, J. M. Montes, and F. G. Cuevas: Metals., **11** (2021) 730.
[22] D. F. Heaney: Handbook of metal injection molding, Woodhead Publishing (2018)
[23] J. O. Andersson, T. Helander, L. Höglund, P. Shi, and B. Sundman: Calphad., **26** (2002) 273.
[24] B.-J. Lee and B. Sundman: TCFE2000: The Thermo-Calc Steels Database, upgraded by B.-J. Lee, KTH, Stockholm (1999)
[25] W.-M. Choi, Y. H. Jo, D. G. Kim, S. S. Sohn, S. Lee, and B.-J. Lee: J. Phase Equilibria Diffus., **39** (2018) 694.
[26] W.-M. Choi, Y. H. Jo, D. G. Kim, S. S. Sohn, S. Lee, and B.-J. Lee: Calphad., **66** (2019) 101624.
[27] H.-S. Do, W.-M. Choi, and B.-J. Lee: J. Mater. Sci., **57** (2022) 1373.
[28] H.-S. Do, T. J. Jang, K. J. Kim, S. S. Sohn, and B.-J. Lee: Mater. Sci. Eng. A., **859** (2022) 144220.
[29] J. Čapek and D. Vojtěch: Mater. Sci. Eng. C., **43** (2014) 494.
[30] E. S. Kim, F. Haftlang, S. Y. Ahn, G. H. Gu, and H. S. Kim: J. Alloys Compd., **907** (2022) 164415.
[31] G. M. Karthik, E. S. Kim, P. Sathiyamoorthi, S. G. Jeong, R. Xiong, S. H. Kang, J.-W. Cho, and H. S. Kim: Addit. Manuf., **47** (2021) 102314.
[32] M. J. Sagong, E. S. Kim, J. M. Park, G. M. Karthik, B.-J. Lee, J.-W. Cho, C. S. Lee, T. Nakano, and H. S. Kim: Mater. Sci. Eng. A., **847** (2022) 143318.
[33] E. S. Kim, F. Haftlang, S. Y. Ahn, H. Kwon, G. H. Gu, and H. S. Kim: J. Mater. Sci., **57** (2022) 17967.
[34] H. Kwon, P. Asghari-Rad, J. M. Park, P. Sathiyamoorthi, J. W. Bae, J. Moon, A. Zargaran, Y. T. Choi, S. Son, and H. S. Kim: Intermetallics., **135** (2021) 107212.
[35] A. E. Tekkaya and K. Lange: CIRP Annals., **49** (2000) 205.
[36] Z. Shen, R. H. Wagoner, and W. A. T. Clark: Acta Metall., **36** (1988) 3231.
[37] F. Haftlang, E. S. Kim, and H. S. Kim: J. Mater. Process. Technol., **309** (2022) 117733.
[38] H. Zhao, F. De Geuser, A. K. da Silva, A. Szczepaniak, D Ponge, and D. Raabe: Acta Mater., **156** (2018) 318.
[39] E. Hryha, E. Dudrova, and L. Nyborg: Metall. Mater. Trans. A., **41** (2010) 2880.
[40] M. Vaidya, K. Guruvidyathri, and B. S. Murty: J. Alloys Compd., **774** (2019) 856.
[41] M. Vaidya, A. Anupam, J. Vijay Bharadwaj, C. Srivastava, and B. S. Murty: J. Alloys Compd., **791** (2019) 1114.
[42] K. Guruvidyathri, B. S. Murty, J. W. Yeh, and K. C. Hari Kumar: J. Alloys Compd., **768** (2018) 358.
[43] S. Yang, G. Liu, and Y. Zhong: J. Alloys Compd., **916** (2022) 165477.

Research Article

pISSN 2799-8525 · eISSN 2799-8681
J Powder Mater 2024;31(3):255-262

Journal of Powder Materials

원자층 증착법을 통한 Nb-Si계 초내열합금 분말 상의 TiO_2 박막 증착 연구

박지영[1], 은수민[1], 변종민[1,2], 최병준[1,2,*]

[1]서울과학기술대학교 신소재공학과
[2]서울과학기술대학교 분말기술연구소

TiO_2 Thin Film Coating on an Nb-Si-Based Superalloy via Atomic Layer Deposition

Ji Young Park[1], Su Min Eun[1], Jongmin Byun[1,2], Byung Joon Choi[1,2,*]

[1]Department of Materials Science and Engineering, Seoul National University of Science and Technology, Seoul 01811, Republic of Korea
[2]The Institute of Powder Technology, Seoul National University of Science and Technology, Seoul 01811, Republic of Korea

Nano-oxide dispersion-strengthened (ODS) superalloys have attracted attention because of their outstanding mechanical reinforcement mechanism. Dispersed oxides increase the material's strength by preventing grain growth and recrystallization, as well as increasing creep resistance. In this research, atomic layer deposition (ALD) was applied to synthesize an ODS alloy. It is useful to coat conformal thin films even on complex matrix shapes, such as nanorods or powders. We coated an Nb-Si-based superalloy with TiO_2 thin film by using rotary-reactor type thermal ALD. TiO_2 was grown by controlling the deposition recipe, reactor temperature, N_2 flow rate, and rotor speed. We could confirm the formation of uniform TiO_2 film on the surface of the superalloy. This process was successfully applied to the synthesis of an ODS alloy, which could be a new field of ALD applications.

Keywords: Superalloy, atomic layer deposition, oxide dispersion strengthening, TiO_2, thin film

Received: April 12, 2024
Revised: May 7, 2024
Accepted: May 8, 2024

***Corresponding author:**
Byung Joon Choi
TEL: +82-2-970-6641
FAX: +82-2-970-6657
E-mail: bjchoi@seoultech.ac.kr

1. Introduction

전 세계적으로 배출되는 이산화탄소의 주 원인은 화석연료로부터 발생하고 있다. 화석연료의 사용량을 절감하여 이산화탄소 발생량을 획기적으로 줄이기 위해 높은 효율의 내연기관의 개발이 주목받고 있다. 내연기관의 효율은 작동 온도 및 압력 증가와 비례하지만, 작동 온도와 압력이 증가할 경우 소재의 열화로 인해 심각한 내구성의 저하가 발생한다. 따라서, 고온·고압 환경에서 기계적 특성, 내열성, 내마모성, 내식성 등을 향상시키기 위한 공정의 개발이 필수적인 상황이다. 현재 근본적인 소재 물성 향상을 위해 산화물 분산 강화 합금(Oxide Dispersion Strengthened alloy, ODS), 즉 ODS 합금의 개발이 주목받고 있다. ODS는 금속기지 내에 산화물을 분산시켜 특성을 향상시키는 방법으로, 여러 금속 강화기구 중 가용 온도가 매우 넓다는 장점을 가지고 있다. 보통 고온 안정성이 우수한 Y_2O_3와 TiO_2 미세 입자를 분산재로 흔히 사용하며, 기지 내 분산된 미세 산화물은 전위의 이동을 효과적으로 억제하므로 고온 인장강도 및 크리프 저항 등을 향상시키게 된다. ODS의 주요 강화기구는 결정립 미세화에 따른 홀-패치(Hall-Petch) 효과, 분산된 산화물에 따른 오로완 메커니즘(orowan mechanism), 고용강화와 매트릭스 효과 등으로 설명되며, 분산된 산화물의 크기와 밀도, 균일도, 결정립 크기 등에 의해 성능이 좌우된다[1-5]. 본 연구에서는 최초로 원자층 증착법(Atomic Layer Deposition, ALD)을 통해 Nb-Si계 초내열합금 분말 상에 TiO_2 나노 박막을 증착하여, 분산 강화 효과를 보기 위한 기초 연구를 수행하였다. ALD란, 전구체 및 반응물의 교차 주입을 통해 낮은 온도 범위에서 나노 단위의 매우 얇은 막을 증착할 수 있는 기술이다. 균일하고 매우 높은 단차 피복(step coverage) 특성을 가지는 박막 성장이 가능하며 조

https://doi.org/10.4150/jpm.2024.00052

성 및 두께 제어에 용이하다는 장점을 지녀 오늘날 박막 증착 분야에서 가장 각광받고 있는 기술이다. 최근에는 평판형의 반도체 기판에 박막을 증착하는 형태에서 벗어나, 추가적인 반응기를 장착하여 나노 로드(nanorod), 나노 파이버(nanofiber) 또는 나노 분말과 같은 입체 구조 기판에 박막 코팅이 가능해졌다. 위 방식은 주로 배터리 및 나노 촉매, 센서 등의 분야에 적용되고 있으며, 나노 구조체 제조에 유리한 특성 때문에 다양한 분야에서 활발히 연구되고 있다[6-12].

본 연구에서는 회전식 반응기 방식을 적용하여 ALD 공정을 실시하였다. Fig. 1은 ALD를 통해 Nb-Si계 합금 분말 표면에 TiO_2 박막을 코팅하는 과정을 도식화 하였다. 반응기가 회전하며 분말이 교반 되고, 이와 동시에 TiO_2 합성에 필요한 전구체와 반응 기체가 순차적으로 주입되며 화학 반응에 의해 표면에 균일한 박막이 형성된다. 'TTIP 주입 – N_2 퍼지 – H_2O 주입 – N_2 퍼지' 순서로 공정이 진행되며, 전구체와 반응 기체 주입 사이 사이에 질소를 흘려주어 반응에 참여하지 않은 부산물을 제거하는 과정을 거친다[13]. 사용한 분말은 Nb-Si계 초내열합금이며, 높은 기계적 강도와 화학적 안정성을 지닌다. 고온에서의 내열성 및 내식성이 뛰어나 항공 및 우주 산업에서 가스터빈, 엔진 등에 주로 사용되는 합금이다[14-23]. 최근 기계적, 열적 특성을 향상시키기 위해 Nb-Si계 합금 조성 최적화 및 열처리 공정을 통한 미세 구조 제어 연구가 활발히 진행되고 있다[24, 25]. 또, 3D 프린팅 기술에 적용되어 소결 기반 고강도 부품의 제작에 사용되며 다른 재료와 혼합하여 다양한 기능성 부품을 제작하고 있다[26]. 분산재로 선택한 TiO_2는 강도가 높으며 경도가 낮은 재료이다. 화학적으로 안정해 내식성이 뛰어나며 고열 안정성 또한 높아, 산화물 분산 강화 합금에 적용할 시 기계적, 화학적 특성 모두 향상시켜 극한의 환경에서 사용하기에 적합한 물질이며, 합금의 중량을 최소한으로 증가시켜 우주 항공 산업에 적용하기에 유리하다[15, 27].

본 연구에서는 기존에 시도되지 않은 Nb-Si계 합금 분말 상에 TiO_2 박막 코팅을 완료하고, TiO_2 코팅막의 형상과 조성, 화학적 특성 및 미세 구조 관찰 결과를 통해 최적의 증착 조건을 탐색하였다. 본 연구를 통해 추후 소결 시 분산된 TiO_2 박막에 의해 합금 내부 결정립 성장이 억제되며 미세 구조 형성을 통한 강도 및 경도 향상 효과를 기대할 수 있다. 또, 소결 접착을 강화하고 열적 안정성을 높여 소결성을 향상시킬 수 있을 것으로 예상된다[28-31].

2. Experimental

본 연구에서는 Nb-15Si-24Ti-13Cr-2Al-2Hf-2Sn-0.5B (at%)

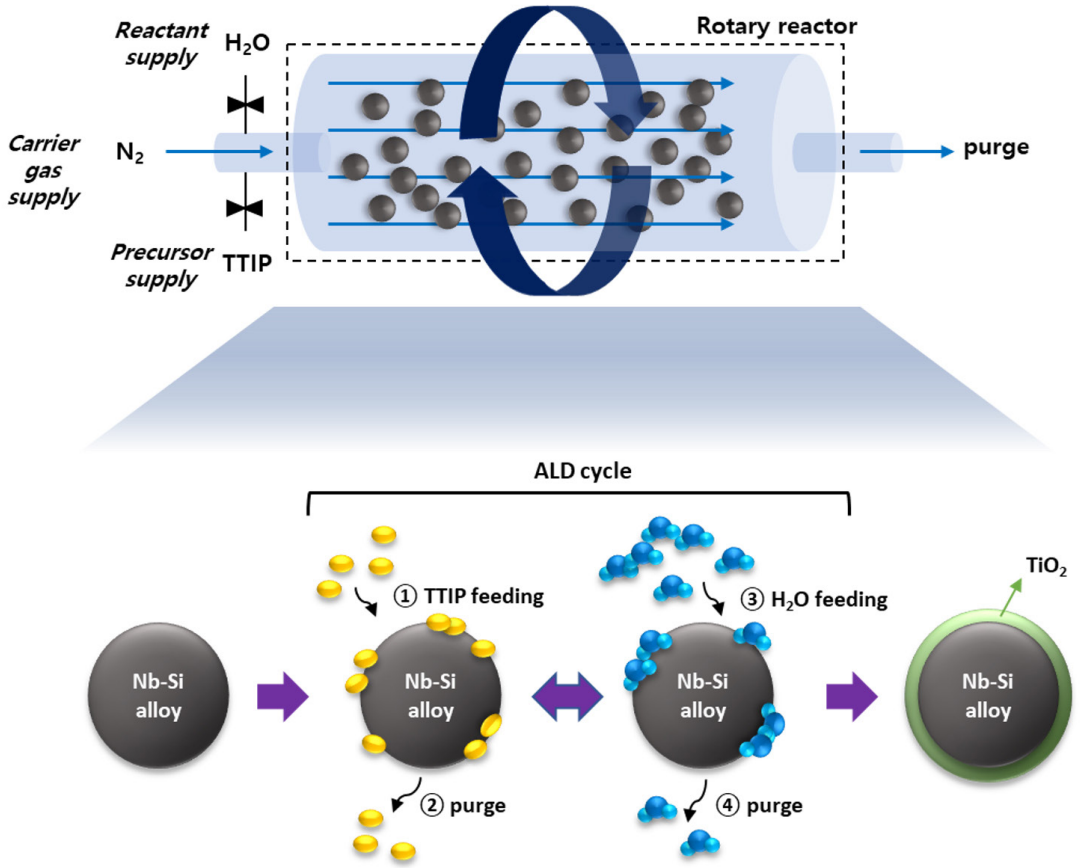

Fig. 1. Schematic of the atomic layer deposition (ALD) process of TiO_2 thin film coating on a powder using a rotary-type reactor

조성의 8원계 합금 분말을 시작 물질로 사용하였다[32]. Nb-Si계 분말은 산소 친화도가 높으며 초고융점 특성을 지녀 기존 금속 분말 제조 공정으로는 적층 제조용 구형 미세 분말 제조가 불가능하다. 이 때문에 세라믹 제외 분무공정인 EIGA (Electrode induction melt gas atomization) 공정에 플라즈마 토치를 결합시킨 플라즈마 하이브리드 EIGA 공정이 개발되었으며, 해당 분말은 PGHA (Plasma gas hybrid atomization) 공정을 통해 제조되었다. PGHA 공정은 기존 gas atomization 공정법과 달리 플라즈마를 통한 고온 유지가 가능해 오리피스의 냉각 및 막힘 현상을 방지할 수 있으며 회수율 50%, RFP 30%에 달하는 성능을 보인다. ALD 박막 증착 공정은 챔버 내에 회전식 반응기를 장입하고 직류 모터를 이용해 분말을 지속적으로 교반하며 실시하였다. Ti의 전구체로는 Titanium Tetraisopropoxide (TTIP, I-CHEMS Co., Korea)를, 반응 가스로는 H_2O를 사용하였다. TiO_2 형성 과정은 다음과 같은 반응식을 따른다.

$$Ti\{OCH(CH_3)_2\}_4 + 2H_2O \rightarrow TiO_2 + 4(CH_3)_2CHOH$$

Table 1은 변수 제어를 진행한 ALD 공정 조건을 나타내었다. ODS 합성을 위한 최적 TiO_2 증착 조건을 찾기 위해 전구체 및 반응물 주입 레시피, 반응기 온도, 운반 기체 유량, 회전 속도(rotor speed)를 조절하여 변수 조절을 진행하였다. 챔버 내 베이스 압력은 3×10^{-2} Torr, 공정 압력은 N_2 운반 기체 유량이 100 sccm일 경우 1.1 Torr, 200 sccm일 경우 1.8 Torr를 유지하였다. TTIP와 H_2O의 캐니스터 온도는 각각 70 ˚C와 25 ˚C로 설정하였으며, TTIP 소스 라인의 온도는 80 ˚C, H_2O 소스 라인의 온도는 100 ˚C로 설정하였다. 모든 샘플은 한 번의 ALD 공정 당 5g의 분말이 사용되었다.

분말 크기를 측정하기 위해 입자 크기 분석(PSA; Particle Size Analyzer, Mastersizer 3000, Malvern, UK)을 실시하였다. 분말 표면 및 TiO_2 박막의 형상 및 정량 분석을 위해 고해상도 주사전자현미경(HR-FESEM; High Resolution Field Emission Scanning Electron Microscope, SU8010, Hitachi, Japan), 집속 이온 빔(FIB; Focused Ion Beam, Crossbeam 350, ZEISS, Germany), 투과전자현미경(HR-TEM; High Resolution Transmission Electron Microscope, NEO ARM, JEOL, Japan), 에너지 분산 X선 분광법(EDS; Energy Dispersive Spectroscopy, NEO ARM, JEOL, Japan), 에너지 분산 X선 형광 분석법(ED-XRF; X-ray Fluorescence, ARL QUANT'X, Thermo Fisher Scientific Co., USA)을 진행하였다. HR-FESEM 및 HR-TEM 분석 시 가속 전압은 각각 10kV 및 200kV를 사용하였다. 분말 및 박막의 화학적 결합 상태를 분석하기 위해 X선 광전자 분광법(XPS; X-ray Photoelectron Spectroscopy, ULVAC PHI, Japan)를 진행하였다.

3. Results and Discussion

3.1. TiO_2 박막 증착 조건 탐색

ALD를 통한 Nb-Si 분말 상의 TiO_2 박막 증착은 Table 1에 나타낸 조건을 적용하여 총 200 사이클 공정을 실시하였다. "Bare"는 원 분말 샘플이며, "T1–T10" 샘플은 ALD 공정 변수를 각각 다르게 조절하여 제작한 것이다. 증착 레시피는 'TTIP 주입–N_2 퍼지–H_2O 주입–N_2 퍼지' 순서로 구성되었으며, 퍼지 시간은 모두 30초로 고정한 채 TTIP 주입은 0.4–1초, H_2O 주입은 0.5–2초 범위로 조절하였다. 반응기 온도는 150 ˚C 및 200 ˚C, N_2 운반 기체 유량은 100 sccm 및 200 sccm, 반응기 교반 속도는 30 rpm 및 60 rpm으로 변화해가며 실험을 진행하였다. 200 ˚C 이하의 반응기 내에서 분말 상의 Ti가 추가적으로 용출 산화가 발생하기에는 충분하지 않은 열에너지가 공급되기 때문에, 공정 과정 중 전구체와 반응물 주입에 의한 TiO_2 박막 형성만이 이루어졌을 것으로 판단된다. ALD 공정 직후 ED-XRF를 통해 측정한 분말 상의 Ti 농도를 Fig. 2에 나타내었다. ED-XRF 분석은 동일 조건 2회 이상 제작한 샘플 각각에서 2회 이상 채취한 시편을 각 5회 이상 측정하여 평균 및 표준편차를 계산한 결과이다. Bare 샘플의 Ti 농도는 약 85.66 μg/cm^{2}이며, T3 및 T7–T10 샘플의 경우 Ti의 농도가 약 91.82–

Table 1. Atomic layer deposition parameters for all samples

Sample	Recipe (sec)	Reactor Temp. (°C)	N2 flow (sccm)	Rotor speed (rpm)
Bare	-	-	-	-
T1	0.4-30-0.5-30	150	100	30
T2	1-30-1-30	150	100	30
T3	1-30-1-30	150	200	30
T4	1-30-1-30	200	100	30
T5	1-30-1-30	200	200	30
T6	1-30-1.5-30	200	200	30
T7	1-30-1-30	200	200	60
T8	1-30-1.5-30	200	200	60
T9	1-30-1.5-30	150	200	60
T10	1-30-2-30	200	200	60

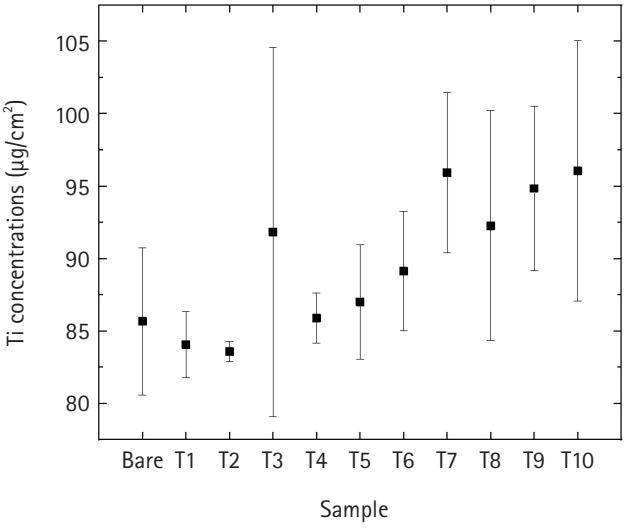

Fig. 2. Ti concentrations of all the samples analyzed by energy-dispersive X-ray fluorescence

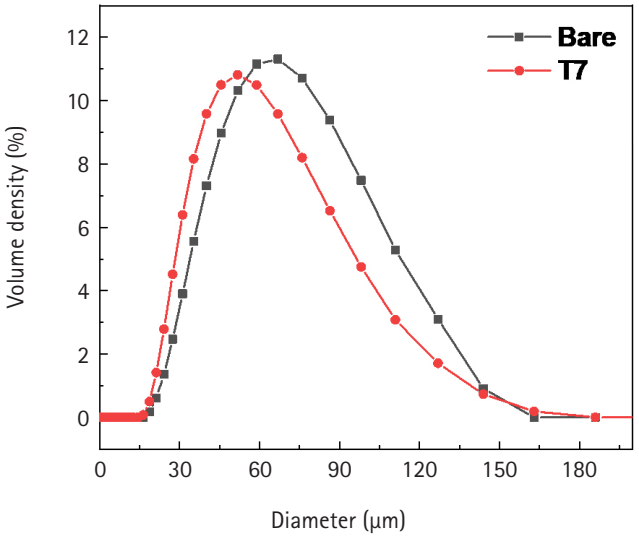

Fig. 3. Particle size and distribution of bare powders and T7 powders analyzed using a particle size analyzer

96.03 μg/cm²까지 증가함을 확인하였다. 다원계 분말 특성 상 ED-XRF 분석 시 노출 부위에 따라 편차가 존재할 수 있으며, T1, T2 샘플의 경우 bare 샘플의 Ti 농도보다 더 낮은 평균값을 가지는데, 이는 측정 편차에 의한 결과이며 두 샘플의 평균값이 bare 샘플의 편차 범위 내에 존재하기 때문에 유효한 결과임을 밝힌다. Ti 농도가 상대적으로 높게 나온 5개 샘플의 증착 조건을 살펴보았을 때, 공통적으로 N_2 운반 기체의 유량이 200 sccm임을 확인할 수 있다. 이는, 100 sccm의 유량으로 전구체 주입 및 퍼지를 진행하였을 때보다 2배 빠른 속도로 물질을 공급하여 증착률을 높일 수 있던 것으로 확인된다. T3 샘플을 제외한 T7–T10 샘플은 공통적으로 반응기를 60 rpm의 회전 속도로 교반하여 실시한 공정이다. 이를 보았을 때, 높은 교반 속도로 인해 공정 과정 중 반응 가스에 분말의 표면적이 더 고르게 노출될 수 있어 박막 증착에 더욱 유리한 환경이 조성된 것으로 예상된다. 상호간 마찰력이 높아 응집이 잘 발생하는 비정형 분말에 비해 구형 분말은 유동성이 좋기 때문에 빠르게 교반해 주며 반응 기체에 최대한 많은 표면을 노출시키는 것이 박막 증착에 유리한 환경으로 판단된다. 또한, 초내열합금 분말은 고온 안정성 및 내식성이 높기 때문에 역학적 에너지가 더 많이 공급될수록 박막 증착을 위한 표면 화학 반응이 유도되기에 유리한 것으로 보인다. 5개 샘플의 증착 레시피를 살펴보았을 때, H_2O 주입 시간이 증가에 따른 Ti 농도 변화의 경향성은 확보하지 못하였으며, 1초 주입 시간으로 충분함을 확인하였다. 반응기 온도 또한 150 ˚C 및 200 ˚C에서 모두 증착이 가능함을 확인하였다. 일반적인 ODS 합금의 경우 기지에 수–수십 % 농도로 산화물 도핑을 진행하는 데에 반해, ALD-TiO_2 박막 코팅을 통한 TiO_2 도핑은 극소량이기 때문에 ED-XRF 결과상 편차가 가장 낮은 안정적인 조건으로 증착되며, Ti 농도가 비교적 높은 T7 증착 조건이 유리할 것으로 판단하였다.

3.2. TiO_2 박막의 미세구조 및 화학적 분석

Nb-Si 분말 상의 TiO_2 박막 증착 조건 확립 이후, 원(bare) 분말과 T7 샘플의 구조화학적 분석을 진행하였다. Fig. 3은 입도 분석 결과를 그래프로 나타낸 것이다. Bare 분말과 T7 분말의 직경을 측정한 결과, 두 분말 모두 약 30–150 μm에 이르는 넓은 분포의 사이즈를 가지고 있으며, T7 분말에서 bare 분말보다 약 15 μm 더 낮은 중간 값을 보였는데, 이는 공정 시 가해주는 열에너지 및 기계적 교반에 의한 마찰에 의해 응집된 분말들이 분산된 것으로 추정된다.

Fig. 4 (a)–(b)는 bare 분말, Fig. 4 (c)–(d)는 T7 분말의 표면을 HR-FESEM을 통해 관찰한 이미지이다. Fig. 4 (a), (c)는 각 분말을 1000배 확대한 이미지이며, 전반적인 분말 형상은 구형이며 마치 여러 원소들이 나노 로드 형태로 석출된 듯한 형태의 표면을 지니고있는 것을 확인할 수 있다. Fig. 4 (b), (d)는 각 분말을 5만배 확대하여 관찰한 이미지이며, bare 분말은 모든 부위가 매끄러운 반면 T7 분말은 표면에 박막이 뒤덮여 더 뚜렷한 가장 자리(edge)를 확인할 수 있다.

TiO_2 박막을 더욱 세밀히 관찰하기 위해 HR-TEM 분석을 실시하였다. Fig. 5는 500 사이클 공정을 실시한 T7 샘플을 FIB를 통해 단면 샘플링한 이후 진행한 HR-TEM 이미지 관찰, EDS 맵핑(mapping) 및 라인 스캔(line scan) 결과를 나타내었다. Fig. 5 (a)–(b)에 나타낸 분말 단면 관찰 결과, 약 21 nm 두께의 비정질 TiO_2 박막이 균일하게 증착된 것을 확인할 수 있다. Fig. 5 (c)의 EDS 맵핑 결과, Nb과 Si이 존재하는 원 분말 상 영역 위로 Ti와 O가 동일 영역 균일하게 분포함을 관찰하였고 동일 두께 범위임을 확인하였

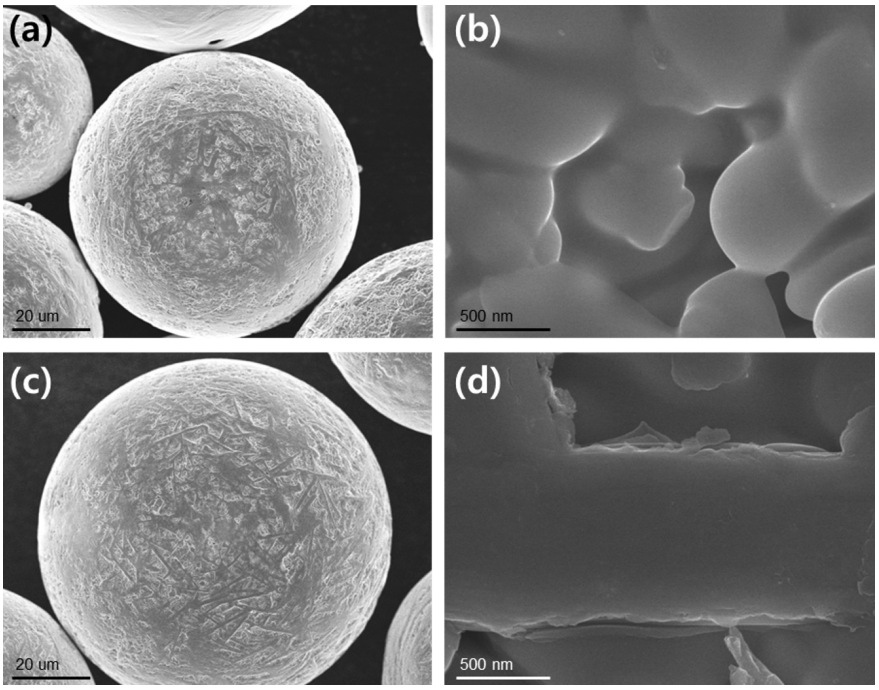

Fig. 4. High-resolution field emission scanning electron microscopy images of the (a–b) bare powder and (c–d) T7 powder

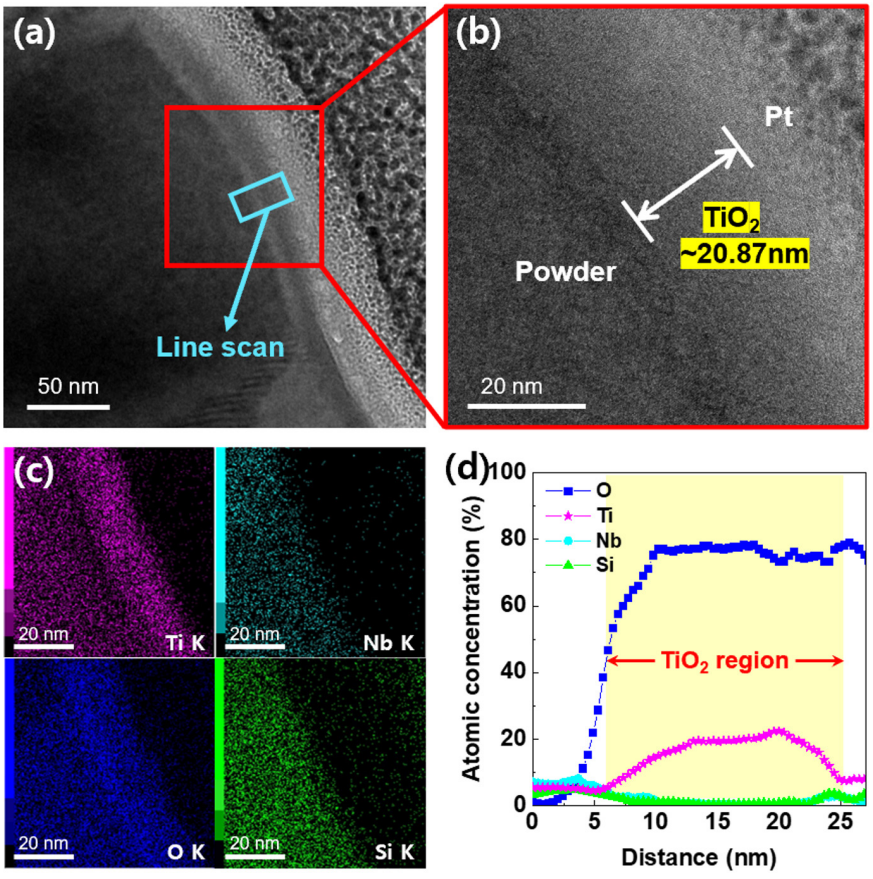

Fig. 5. (a-b) Cross-sectional high-resolution transmission electron microscopy images of T7 powder/TiO_2 interface. (c) Energy-dispersive spectroscopy mapping and (d) atomic concentration from the line-scanned range

다. Fig. 5 (d)는 라인 스캔을 통해 EDS 관찰을 진행했던 4가지 원소의 원자 분율 측정 결과를 나타내었다. 약 20 nm 두께 영역에서 동일하게 Ti와 O가 증가, Nb, Si이 감소하는 경향성을 관찰할 수 있다. 이를 통해 Nb-Si 분말 표면에 TiO_2 박막이 균일하게 증착됨을 확인할 수 있다.

다음으로 증착된 TiO_2 박막의 화학적 결합 상태를 고찰하기 위해 XPS 분석을 실시하였다. Fig. 6는 각각 bare 및 T7 샘플의 (a) Ti 2p, (b) O 1s, (c) Nb 3d, (d) Si 2p의 결합 에너지 분포를 나타내었다. Fig. 6 (a)의 Ti 2p 스펙트럼을 보면, 약 458 eV와 464.1 eV에 해당하는 Ti $2p_{3/2}$, Ti $2p_{1/2}$ 피크가 관찰되었으며, TiO_2가 표면에 증착된 T7 샘플에서 두 피크의 강도가 더 강하게 뜨는 것을 확인할 수 있다. Ti^{3+} 피크 대비 Ti^{4+} 피크의 분율을 비교할 시, bare 샘플에서 약 9.1, T7 샘플에서 약 15.2가 도출되었다. T7 샘플에서 피크 강도가 증가함과 동시에 서브 피크(sub-peak) 대비 Ti^{4+} 피크의 분율이 큰 것을 보아, TiO_2 박막이 증착됨을 확인할 수 있다. Fig. 6 (b)는 O 1s 분석 결과이며, 약 530 eV에서 Ti-O 결합에 해당하는 피크가 지배적으로 존재함을 확인하였다. 약 531.5 eV 부근의 서브 피크는 원 분말 상에 형성된 SiO_2로 추정되며, 표면에 TiO_2가 결합된 T7 샘플에서 강도가 더 약해진 것을 확인할 수 있다. Fig. 6 (c)–(d)는 원 분말 상에 존재하는 Nb 3d 및 Si 2p 원소의 결합 에너지 분포를 나

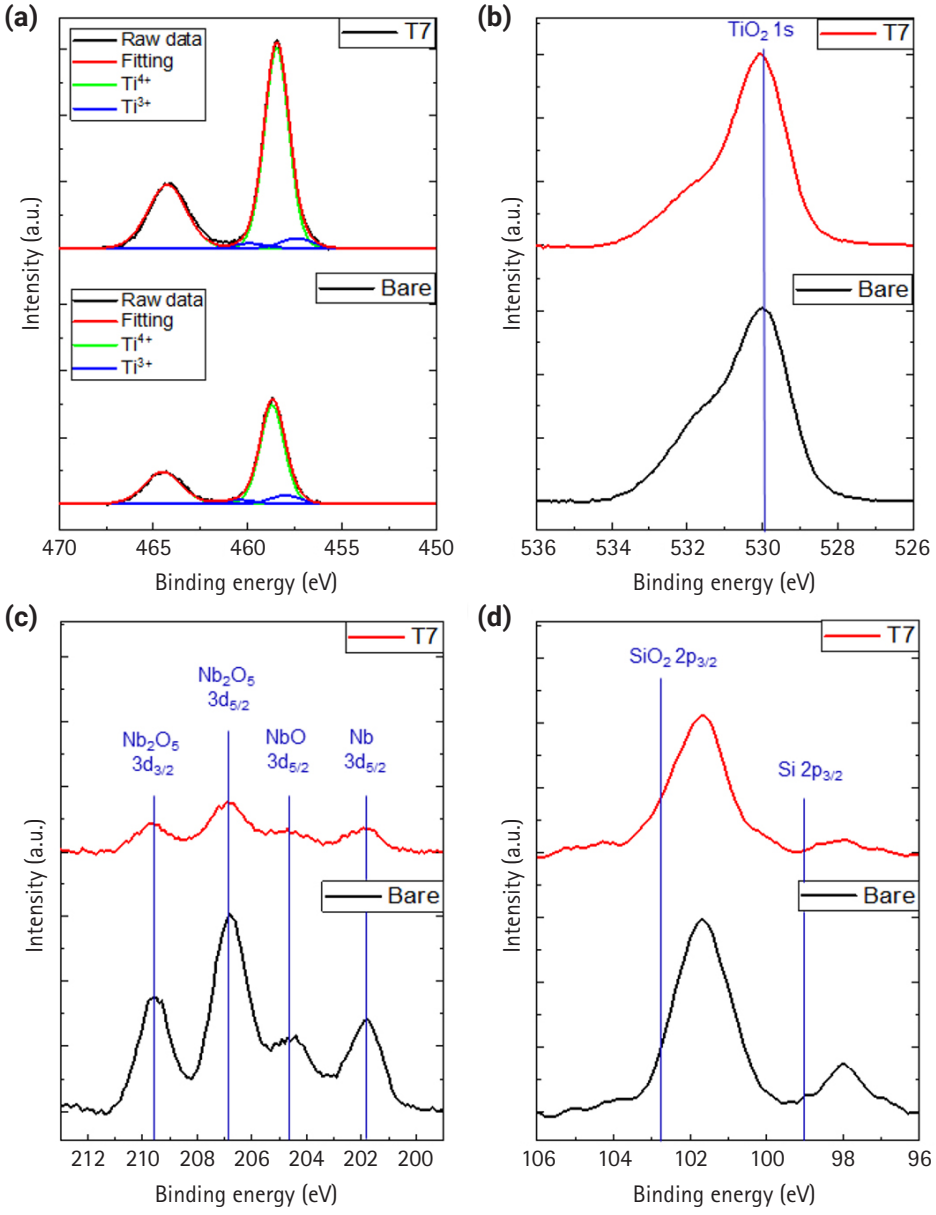

Fig. 6. X-ray photoelectron spectroscopy spectra of (a) Ti 2p, (b) O 1s, (c) Nb 3d and (d) Si 2p for the bare and T7 samples

타내었다. Bare 분말에 비해 T7 분말에서 각 피크의 강도가 더 낮아지는 것을 확인할 수 있다. 이는 표면에서 감지할 수 있는 신호의 양이 더 적기 때문이며, TiO_2 박막이 코팅되었기 때문임을 짐작할 수 있다. Si 2p 피크는 전하 효과에 의해 전반적으로 낮은 에너지 방향으로 이동됨을 확인하였다. 위 분석을 통해 분말 표면에 TiO_2 박막이 잘 결합하여 형성되었음을 확인할 수 있다.

4. Conclusion

본 연구에서는 Nb-Si계 초내열합금 분말 상에 회전식 반응기를 이용한 ALD를 통해 표면에 TiO_2 박막을 코팅하였으며, 다양한 공정 변수를 조절하여 최적의 증착 조건을 확립하였다. H_2O 주입량을 1초 이상으로 늘렸을 때 Ti 농도의 경향성은 발견되지 않았으며, N_2 운반 기체의 유량이 200 sccm, 교반 속도가 60 rpm일수록 비교적 안정적으로 높은 Ti 농도를 확보할 수 있음을 확인하였다. 분말 표면 상의 TiO_2 박막 증착 최적 조건은 다음과 같다; 'TTIP 1 s 주입 – N_2 30 s 퍼지 – H_2O 1 s 주입 – N_2 30 s 퍼지' 순의 증착 레시피, 반응기 온도 200˚C, N_2 운반 기체 유량 200 sccm, 교반 속도 60 rpm. HR-FESEM을 통한 TiO_2 코팅 샘플의 표면 형상 관찰 시 bare 분말에 비해 박막 코팅에 의한 뚜렷한 표면부가 관찰되었으며, 500 사이클 공정 후 HR-TEM 및 EDS 정량분석을 통해 약 21 nm의 균일한 박막이 증착됨을 확인하였다. XPS 분석 결과, 기저 분말 상에 존재하는 Nb 3d, Si 2p 결합 에너지는 TiO_2가 증착됨에 따라 강도가 낮아졌으며, Ti 2p에서의 서브 피크 대비 Ti4+ 피크 분율 증가, O 1s에서의 서브 피크가 감소함을 확인하였다. 회전식 반응기 타입 ALD를 도입하여 Nb-Si계 합금 분말 상의 TiO_2 박막 증착이 성공적으로 이루어졌으며, 공정 변수를 제어하여 TiO_2 박막 증착률을 높일 수 있었다. 후속 연구에서는 소결체를 제작 후 기계적 물성 평가를 통한 산화물 분산 강화 효과를 입증할 계획이다. ALD를 통한 TiO_2 코팅막 형성은 소결 중 결정립 성장 억제 효과 및 분산 강화에 기여할 것으로 기대된다.

Conflict of Interest Declaration

교신저자는 현재 JPM편집이사로 봉사 중이지만, 논문 출판과정의 어떤 과정에서도 관여하지 않았습니다. 이 사항을 제외하면 저자들은 잠재적인 이해상충에 관련된 해당사항이 없음을 선언합니다.

Author Information

박지영, 은수민: 학생, 변종민, 최병준: 교수

Acknowledgement

본 연구는 한국연구재단의 기초연구실 지원사업(2022R1A4A5033917)으로 수행되었습니다.

References

[1] C. Qiu: J. Alloys Compd., **790** (2019) 1023.
[2] M. B. Wilms, S. K. Rittinghaus, M. Goßling, and B. Goekce: Prog. Mater. Sci., **133** (2023) 101049.
[3] Z. Dong, W. Hu, Z. Ma, C. Li, and Y. Liu: Mater. Chem. Front., **3** (2019) 1952.
[4] L. Yu, Z. Lu, S. Peng, and X. Li: Mater. Sci. Eng. A., **845** (2022) 143240.
[5] M. B. Wilms, N. Pirch, and B. Göekce: Prog. Addit. Manuf., **8** (2023) 2.
[6] S. Adhikari, S. Selvaraj, and D. H. Kim: Adv. Mater. Interfaces., **5** (2018) 1800581.
[7] S. He, A. Bahrami, X. Zhang, I. G. Martíne, S. Lehmann, and K. Nielsch: Adv. Mater. Technol., **7** (2022) 2100953.
[8] M. J. Jung, M. Ji, J. H. Han, I. Y. S. T. Oh, H. M., and B. J. Choi: Ceram. Int., **48** (2022) 36773.
[9] Y. Hu, J. Lu, and H. Feng: RSC Adv., **11** (2021) 11918.
[10] C. Hirschberg, N. S. Jensen, J. Boetker, A. Ø. Madsen, T. O. Kääriäinen, M. L. Kääriäinen, P. Hoppu, S. M. George, M. Murtomaa, C. C. Sun, J. Risbo, and J. Rantanen: Org. Process Res. Dev., **23** (2019) 2362.
[11] M. Lee, W. Ahmad, D. W. Kim, K. M. Kwon, H. Y. Kwon, H. B. Jang, S. W. Noh, D. H. Kim, S. J. A. Zaidi, H. Park, H. C. Lee, M. A. Basit, and T. J. Park: Chem. Mater., **34** (2022) 3539.
[12] S. Choi, J. H. Han, and B. J. Choi: J. Powder Mater., **26** (2019) 243.
[13] J. Y. Park, J. H. Han, and B. J. Choi: J. Vac. Sci. Technol. A., **42** (2024) 3.
[14] L. Su, L. Jia, J. Weng, Z. Hong, C. Zhou, and H. Zhang: Corros. Sci., **88** (2014) 460.
[15] P. Tsakiropoulos: Prog. Mater. Sci., **123** (2022) 100714.
[16] G. Kommineni, B. R. Golla, M. Z. Alam, R. Sarkar, and S. P. VV: J. Alloys Compd., **873** (2021) 159832.
[17] Z. Sun, X. Guo, and B. Guo: Int. J. Refract. Hard Met., **51** (2015) 243.
[18] N. Wang, L. Jia, B. Kong, Y. Guo, H. Zhang, and H. Zhang: Int. J. Refract. Hard Met., **71** (2018) 273.
[19] S. Zhang and X. Guo: Intermetallics., **64** (2015) 51.
[20] S. Zhang and X. Guo: Intermetallics., **70** (2016) 33.
[21] G. Sun, L. Jia, Z. Hong, G. Liu, and H. Zhang: Prog. Nat. Sci.: Mater. Int., **31** (2021) 442.
[22] W. Liu, S. Huang, C. Ye, L. Jia, Y. Kang, J. Sha, B. Chen, Y. Wu, and H. Xiong: J. Mater. Sci. Technol., **149** (2023) 127.
[23] Y. Tian, G. Cheng, J. Guo, L. Zhou, L. He, and H. Ye: Adv.

Eng. Mater., **9** (2007) 963.
[24] Y. Kang, F. Guo, and M. Li: Mater. Sci. Eng. A., **760** (2019) 8.
[25] M. Sankar, G. Phanikumar, V. Singh, and V. S. Prasad: Intermetallics., **101** (2018) 123.
[26] Y. Guo, L. Jia, B. Kong, S. Zhang, J. Sha, and H. Zhang: J. Alloys Compd., **696** (2017) 5.
[27] M. Fujikura, A. Kasama, R. Tanaka, and S. Hanada: Mater. Trans., **45** (2004) 2.
[28] Y. Li, W. Zhu, Q. Li, S. Qiu, and J. Zhang: J. Alloys Compd., **704** (2017) 311.
[29] T. Geng, C. Li, J. Bao, X. Zhao, Z. Du, and C. Guo: Intermetallics., **17** (2009) 343.
[30] D. Reyes, V. Malard, S. Drawin, A. Couret, and J. P. Monchoux: Intermetallics., **144** (2022) 107509.
[31] W. Mao and X. Guo: Prog. Nat. Sci.: Mater. Int., **22** (2012) 139.
[32] J. Yang, G. Zhuo, K. Jiang, X. Zhu, and L. Su: Materials., **13** (2020) 1229.

Research Article

pISSN 2799-8525 · eISSN 2799-8681
J Powder Mater 2024;31(3):263-271

Journal of Powder Materials

다양한 고체분산체 제조방법으로 제조한 실로도신 함유 고체분산체의 비교 및 특성분석

이수만, 송다영, 김경수*

경상국립대학교 제약공학과

Comparison and Characterization of Silodosin-loaded Solid Dispersions Prepared by Various Solid Dispersion Preparation Methods

Su Man Lee, Da Young Song, Kyeong Soo Kim*

Department of Pharmaceutical Engineering, Gyeongsang National University, 33 Dongjin-ro, Jinju 52725, Republic of Korea

This study focused on improving the solubility of silodosin, a drug poorly soluble in water, by utilizing solid dispersions. Three types of dispersions were examined and compared against the drug powder: surface-attached (SA), solvent-wetted (SW), and solvent-evaporated (SE). Polyvinyl alcohol (PVA) was identified as the most effective polymer in enhancing solubility. These dispersions were prepared using spray-drying techniques with silodosin and PVA as the polymer, employing solvents such as water, ethanol, and a water-acetone mix. The physicochemical properties and solubility of the dispersions were evaluated. The surface-attached dispersions featured the polymer on a crystalline drug surface, the solvent-wetted dispersions had the amorphous drug on the polymer, and the solvent-evaporated dispersions produced nearly round particles with both components amorphous. Testing revealed that the order of improved solubility was: solvent-evaporated, solvent-wetted, and surface-attached. The results demonstrated that the preparation method of the solid dispersions significantly impacted their physicochemical properties and solubility enhancement.

Keywords: Silodosin, Polymer, Solid dispersion, Spray drying, Solubility

Received: May 27, 2024
Revised: June 18, 2024
Accepted: June 18, 2024

***Corresponding author:**
Kyeong Soo Kim
Tel: +82-55-772-3391
Fax: +82-55-772-3399
E-mail: soyoyu79@gnu.ac.kr

1. Introduction

양성 전립선 비대증(Benign prostatic hyperplasia, BPH)은 노년 남성에게서 흔히 관찰되는 전립선의 크기가 증가하는 질병이다. 이로 인해 환자는 잔뇨감, 소변줄기 약화 또는 끊김, 빈뇨, 야뇨증 등 다양한 하부 요로 증상(Lower urinary tract symptoms, LUTS)을 겪게 된다[1]. 사람의 전립선, 방광기저부, 방광 경부, 전립선 피막 및 요도에는 교감 신경 중 하나인 시냅스 후 α1 아드레날린 수용체가 다량 분포한다. 실로도신(Silodosin)은 α1 아드레날린 수용체를 차단하는 역할을 하여 이러한 조직의 평활근을 이완시켜 소변흐름이 개선되고, 전립선 비대증의 증상이 감소하게 된다[2].

실로도신의 IUPAC명은 1-(3-hydroxypropyl)-5-[(2R)-2-({2-[2-(2,2,2-trifluoroethoxy)phenoxy]ethyl}amino)propyl]-2,3-dihydro-1H-indole-7-carboxamide이며[3], 화학식은 $C_{25}H_{32}F_3N_3O_4$, 분자 구조는 Fig. 1과 같다. 흰색~황백색 분말로 녹는점은 약 105 ˚C~109 ˚C이며, 아세트산과 알코올에는 매우 잘 용해되나 물에는 아주 약간 용해된다고 FDA 라벨에 명시되어 있다[4]. 경구 투여 약물의 경우 위장관 막을 통하여 전신순환에 도달하기 때문에 먼저 위 또는 장액에서 용해되어야 한다[5]. 물에 잘 녹지 않는 약물의 특성으로 인하여 경구 투여 시 용해 및 흡수에 관련한 문제 가능성을 가지고 있다. 실로도신의 수용해도 개선은 궁극적으로 약물의 경구 생체 이용률을 증가시킬 수 있을 것으로 사료된다.

약물의 수용해도 개선을 위한 방법으로는 공결정 형성, 염형성,

https://doi.org/10.4150/jpm.2024.00143

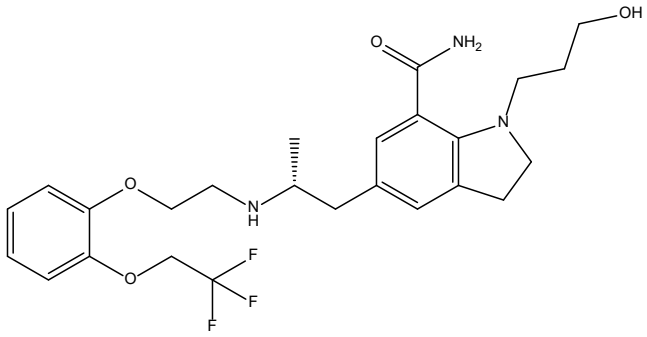

Fig. 1. Structure of silodosin.

사이클로덱스트린과의 복합체화, SNEDDS (Self-NanoEmulsifying Drug Delivery System) 및 나노 파티클 등 여러가지 방법이 사용되어왔다[6]. 이러한 가용화 방법 외에 고체분산체(Solid dispersion, SD) 제조는 약물의 용해도를 향상시켜 생체 이용률을 향상시키는 전통적이며 효과적인 수단 중 하나이다[7]. 고체분산 기술에 의한 약물 가용화와 관련한 메커니즘의 기본 원리는, 약물의 입자 크기를 감소시키고 약물의 결정성을 제거함으로써 무정형 약물을 만들 수 있게 된다[8]. 결정성 약물은 용해 과정에서 격자 분해 에너지가 필요하지만 무정형 약물은 격자 에너지가 불필요하며 표면적이 증가하여 무정형 약물이 결정형보다 더 잘 용해되게 된다[9]. 고체분산체 제조는 사이클로덱스트린 복합체화와 달리 하이드록시프로필-β-사이클로덱스트린과 같은 고가의 부형제가 필수가 아니기 때문에 비용 효율적인 기술로 간주할 수 있다[10]. 고체분산체가 효과적으로 작동하기 위해서는 약물의 입자크기가 감소하여 표면적이 증가하고, 무정형 형태로 전환되는 것이 효과적이다. 무정형 형태를 안정화하기 위해 약물과 담체 사이에 수소결합과 같은 적절한 상호작용이 필요한 것으로 사료된다.

본 연구에서는 표면부착(SA) [11], 용매습윤(SW) [12], 용매증발(SE) [13] 세 가지 방법으로 제조한 고체분산체를 비교하기 위하여 PVA 그리고 다양한 용매를 사용하여 실로도신을 함유한 고체분산체를 제조하였다.

SA-SD는 용해된 담체가 분무건조 시 약물입자 표면에 부착된다. 용액 내 약물이 분산 상태이므로 약물의 고유 결정 형태가 남아 있을 수 있지만 약물표면의 담체에 의해 용해능은 향상될 수 있다. 대부분 용매로 물을 사용하기 때문에 제조 시 폭발의 위험성이 적고 무정형 고체분산체에 비하여 재결정화 위험이 감소하지만, 약물의 결정성이 잔존하므로 용해도 개선이 제한적이라는 단점을 가지고 있는 것으로 알려져 있다[11].

약물은 용해되고 담체는 용해되지 않는 유기용매를 사용하여 SW-SD를 제조한다. 이는 SA-SD와는 달리, 용해된 약물이 무정형 형태로 담체와 결합하게 된다. 이 시스템은 약물의 재결정화를 감소시키지만 SE-SD에 비해 약물용해도 향상이 상대적으로 낮을 수 있다[12].

SE-SD는 용매에 약물과 담체를 모두 용해시켜 무정형 고체분산체를 제조함으로써 약물용해도를 크게 향상시키는 장점을 가지고 있다. 그러나 SE-SD에서 약물이 무정형에서 결정형으로 변환될 가능성을 내재하고 있다[13].

주사전자 현미경(SEM)과 분말 X-선 회절 분석기(PXRD), 푸리에-변환 적외선 분광기(FT-IR)를 이용하여 세 가지 상이한 방법으로 제조한 고체분산체의 물리적 특성을 확인하고 포화용해도 및 동적 용해도를 확인하여 결정성을 지닌 실로도신과 비교하였다. 또한 SA, SW 및 SE 제조방법의 차이로 인하여 제조된 각 고체분산체는 입자의 형태 및 크기 등 특성에 차이를 가지게 된다. 연구를 통해 이러한 차이에 대해 확인하고, 특성 차이에서 기인한 용해도 향상 정도의 차이를 알아보았다.

2. Experimental

2.1. 시약 및 기기

실로도신 및 Na-alginate, HPMC 2910 P-603, HPMC 2910 P-645, PVP K30, Gelatin은 한미약품 (Hwasung, South Korea)에서 제공받아 사용하였다. Parteck SRP 80 (폴리비닐알코올, PVA)은 Merck (Darmstadt, Germany)에서 구매하여 사용하였다. Dextran은 한양대학교(Seoul, South Korea)에서 제공받아 사용하였다. HPC-L은 코스맥스(Seongnam, South Korea)에서 제공받아 사용하였다. Na-CMC는 덕산약품(Ansan, South Korea)에서 구매하여 사용하였다. β-Cyclodextrin은 Ashland (Delaware, USA)에서 구매하여 사용하였다. Carbopol 934 및 Carbopol 941은 3V sigma (Bergamo, Italia)에서 구매하여 사용하였다. Kollidon VA64는 보령제약(Seoul, South Korea)에서 제공받아 사용하였다. 아세토니트릴, 아세톤, 에탄올 및 제2인산칼륨(K_2HPO_4)는 대정화금(Siheung, South Korea)에서 구매하여 사용하였다. 기타 용매 및 시약은 모두 시판 시약급을 사용하였다.

HPLC 분석 장비는 Agilent 1260 Infinity HPLC system (Agilent Technologies, Santa Clara, CA, USA)를 사용하였으며, 검출기는 Chemstation software, G1311C 1260 Quat Pump, G1314 1260 VWD를 사용하였다. 실로도신의 최대 흡광 파장 확인은 자외선-가시선 분광 광도계(UV-1800, Shimadzu, Japan)를 이용해 확인했으며, HPLC 분석 시 컬럼은 VDSpher 100 C18 M-E (VDS optilab, Berlin, Germany), 4.6 mm x 150 mm, 5 μm particle size를 선정하여 사용하였다. 포화용해도 및 동적 용해도 평가를 위한 진탕 항온수조는 대한랩테크사의 LSB-045S (Namyangju, South Korea)를 사용하였다. 원심분리기는 Micro Centrifuge 1730R (Gyrozen, Gimpo, South Korea)을 사용하였다. 고체분산체 제조를 위한 분무건조기는 실험실 규모의 미니 분무건조기 Model - ADL311 Spray dryer (Yamato, Tokyo, Japan)을 사용하였다.

2.2. 실로도신을 함유한 세 가지 고체분산체 제조

고체분산체를 제조할 고분자 선정을 위해 1 % (w/v) 고분자용액

을 사용하였다. 10 % 또는 20 %와 같은 고농도 고분자 용액의 경우 점도가 증가하여 약물의 용해도 확인에 영향을 미칠 가능성을 고려하였다. 또한 저농도의 고분자 용액에서는 고분자의 침전이 약물의 용해도를 왜곡할 가능성을 감소 시킬 수 있을 뿐 아니라, 1 %와 같은 저농도에서 용해도 평가를 시작하면 기준 값의 설정이 가능하기 때문에 고농도에서 추가 실험을 수행하여 농도 의존적 효과의 관찰이 가능하다고 판단하여 이와 같이 실험을 설계하였다.

1 % (w/v) 고분자 용액 1 mL가 들어있는 e-tube에 실로도신 약 10 mg을 넣은 후 혼합액을 37 ± 0.5 ˚C의 진탕 항온수조에서 5일간 보관하며 볼텍스 믹서(Vortex-Genie 2, Scientific Industries, Inc., USA)로 섞어주며 과포화 시켰다. 이 후 각 e-tube를 원심분리기를 사용하여 37 ˚C, 13,500 g조건에서 15분 동안 원심분리 하여 얻어진 상등액을 0.45 μm 주사기 필터로 여과해 얻어진 맑은 용액을 이동상으로 10배 또는 100배 희석하여[14, 15], 상기의 HPLC 시스템을 이용하여 분석하였다. 이동상은 아세토니트릴과, 50 mM 제2인산칼륨을 인산으로 pH가 6.0이 되도록 조정한 용액을 35 : 65부피비로 혼합하여 사용하였다. 유속은 1.0 mL/min, 컬럼온도는 40 ˚C, 주입 부피는 20 μL로 분석하였다[16]. 메탄올 용액으로 500 μg/mL실로도신 원액을 제조 후 계대 희석하여 1, 2.5, 5, 10, 25, 50 μg/mL 시험액을 제조한다. 이를 자외선-가시선 분광광도계로 최대흡수부가 210 nm인 것을 확인하여, 흡수파장은 210 nm로 설정하여 분석하였다.

1 % (w/v) 고분자용액의 용해도 결과를 바탕으로 선택된 PVA와 약물, 서로 다른 용매로 구성된 고체분산체 제조용 용액을 분무건조기를 사용하여 고체분산체를 제조하였다. PVA를 정제수에 완전히 용해시킨 후 실로도신을 현탁 시킨 후 분무건조기의 주입구 온도 110 ℃, 배출구 온도 62 ~ 63 ℃, 공급 유속은 2 mL/min이 되도록 설정하여 표면부착 고체분산체(SA-SD)를 제조하였다. 용매습윤 고체분산체(SW-SD) 제조를 위하여 실로도신을 에탄올에 완전히 용해시키고 PVA를 이 용액에 현탁 시켰다. 분무건조기의 주입구 온도 80 ˚C, 배출구 온도 50 ˚C, 공급 유속은 4 mL/min이 되도록 설정한 후 분무건조 하였다. 용매증발 고체분산체(SE-SD)의 경우, 실로도신을 아세톤에 완전히 용해시키고 PVA는 정제수에 완전히 용해시킨다. 이 후 두 solution을 혼합하여 분무건조기의 조건을 주입구 온도 90 ˚C, 배출구 온도 55 ˚C, 공급 유속은 2 mL/min이 되도록 설정 후 분무건조하여 제조하였다. 분무 공기 압력은 0.1 MPa로 세 조건 모두 동일하며, 실로도신과 PVA 및 용매의 비율은 Table 2와 같다.

2.3. 실로도신을 함유한 세 가지 고체분산체의 물리화학적 특성 분석

표면 형태학적 특성 - 실로도신 약물 분말과 PVA, 표면부착(SA), 용매 습윤(SW) 및 용매증발(SE)방법으로 제조된 고체분산체의 형태 및 표면 특성을 방사형 주사 전자 현미경(FE-SEM, Tescan-MIRA3, Kohoutovice, Czech)을 사용하여 확인하였다. 샘플을 고정하기 위해 이중 접착 탄소 테이프를 디스크에 붙인 후 테이프 부착면에 샘플을 붙였다. 샘플은 EmiTech Sputter Coater (K575X)를 사용하여 7 × 10^{-3} mbar의 압력, 25 mA 전류에서 6 nm/min의 속도로 4분간 백금 코팅을 진행 후 확인하였다.

결정성 – 실로도신 약물 분말과 PVA, 표면부착, 용매 습윤 및 용매증발 방법으로 제조된 고체분산체의 결정 상태를 확인하기 위해 miniflex goniometer와 Cu Kα1 단색 방사선 소스가 장착되어 있는 Rigaku X-Ray Diffracto meter(D/MAX-2500 PC, RIgaku Corporation, Tokyo, Japan)을 이용하여 결정상태를 평가하였다. 상온에서 40mA와 40kv 조건, 5°≤2θ≤60°에서 초당 0.02°의 증가속도로 측정하였다.

분자간 상호작용 – 단독 원료와 고체분산체 3종류를 FT-IR (Spectrum Two Pharmaceutical System, PerkinElmer, USA)을 사용하여 분석하였다. 파장범위는 400 ~ 4000 cm^{-1}으로 설정하였으며, 검출기는 고직선성 실온 검출기를 사용하였다.

약물함량 시험 – 실로도신 10 mg을 정확하게 칭량하여 정제수와 에탄올을 50:50 (v/v)로 제조한 용매에 완전히 용해 시킨다. 0.45 μm 주사기 필터를 사용해 여과하여 표준액으로 하였다. 각 고체분산체는 20 mg(실로도신 함량 10 mg 해당량)을 정밀히 칭량하여 표준액과 같은 용매로 용해시킨 후 상기와 같이 0.45 μm 주사기 필터를 사용해 여과하여 검액으로 하였다. 모든 실험은 3번 반복하였다.

포화용해도 시험 – pH 6.8 용액 및 정제수에서의 용해도를 평가하기 위해 실로도신 약물 및 실로도신을 함유한 고체분산체를 실로도신으로서 10 mg해당량이 되도록 정밀히 칭량하여 e-tube에 넣은 후 각 시험액을 1 mL씩 넣는다. 혼합액을 37 ˚C의 진탕 항온수조에서 5일간 보관하며 볼텍스 믹서로 섞어주며 포화 시켰다. 이 후 각 e-tube를 원심분리기를 사용하여 13,500 g에서 15분 동안 원심 분리하여 얻어진 상등액을 0.45 μm 주사기 필터를 통해 얻어진 맑은 용액을 이동상으로 희석하여, 상기의 HPLC 시스템과 조건으로 분석하였다. 모든 실험은 3번 반복하였다.

동적 용해도 시험 – 세 종류의 실로도신 함유 고체분산체 각각의 동적 용해도를 평가하기 위하여 포화용해도 시험과 마찬가지로 pH 6.8 용액 및 정제수를 시험액으로 하여 확인하였다. 고체분산체(실로도신으로서 10 mg해당량)를 시험액 30 mL가 들어있는 Conical tube에 넣고, 진탕 항온수조를 37 ˚C, 100 rpm 조건으로 설정하였다. 이를 교반 하면서 10, 20, 30, 60, 120, 180 및 240분에서 1 mL씩 샘플링 하여 0.45 μm 주사기 필터를 이용해 여과하

Table 2. Formulation of silodosin-loaded solid dispersion.

Formulation	SA-SD	SW-SD	SE-SD
Silodosin	8 mg	8 mg	8 mg
PVA	8 mg	8 mg	8 mg
(Water)	600 g	-	400 g
(Acetone)	-	-	200 g
(Ethanol)	-	600 g	-
Assay (%)	105.6	68.6	95.9

여 샘플을 얻었다[17]. 샘플을 이동상으로 10배 희석하여 포화용해도와 같은 조건으로 HPLC 분석을 진행하였다. 모든 실험은 3번 반복하였다.

3. Results and Discussion

3.1. 부형제 선정 및 고체분산체의 제조

본 연구에서는 실로도신 용해도를 향상시키기 위한 방법으로 약물과 고분자가 균질하게 혼합되어 있는 고체분산체 제조기술을 사용하였다. 실로도신의 용해도를 개선시킬 수 있는 고분자를 선정하기 위하여 다양한 고분자 용액에서의 실로도신 용해도를 확인하였다. 평가에 사용된 친수성 고분자 1 % 용액 중 PVA용액에서 실로도신의 용해도가(264.1 ± 0.6 μg/mL vs 1063.7 ± 16.6 μg/mL)가 가장 크게 증가한 것을 알 수 있었다(Table 1, Fig. 2). PVA는 수용성 특성이 있는 합성 고분자로 친수성인 하이드록실 그룹과 소수성인 아세틸 그룹을 모두 가지는 독특한 특성을 가지고 있으며, pH에 비의존적인 용해도 특성을 가진 비이온성 고분자이다[18]. 무독성, 발암 무해성, 우수한 상용성 및 인체조직과 체액에서 생분해성을 가지므로 의학/약학 분야에서 많이 사용되는 고분자 중 하나로 알려져 있다. 또한 물에는 쉽게 용해되지만, 일반 유기용매에서는 불용성인 특성을 가지고 있다[19]. 이러한 PVA의 특성을 고려하여 용매를 달리하여 각기 다른 특성을 가진 3가지 (SA, SW, SE) 고체분산체를 제조하기에 적절하다고 사료되어, PVA를 실로도신의 가용화를 위한 고분자 담체로 선정하였다. 용매의 특성을 고려하여 제조할 수 있는 다양한 고체분산체를 제조하기 위하여, 용매를 달

Table 1. Solubility results of silodosin in 1 %(w/v) Polymer solutions.

1 %(w/v) Polymer	Concentration.(μg/mL)	
	Mean	± SD
Water	264.1	0.6
Na-alginate	114.8	3.9
Dextran	180.2	12.4
HPC-L	214.2	12.9
Na-CMC	215.1	36.8
HPMC 2910 P-603	252.0	36.0
HPMC 2910 P-645	254.7	7.1
PVP K30	316.5	50.4
β -Cyclodextrin	496.1	13.3
Carbopol 934	576.4	42.9
Gelatin	605.0	5.7
Kollidon VA64	679.0	7.7
Carbopol 941	866.1	59.5
PVA	1063.7	16.6

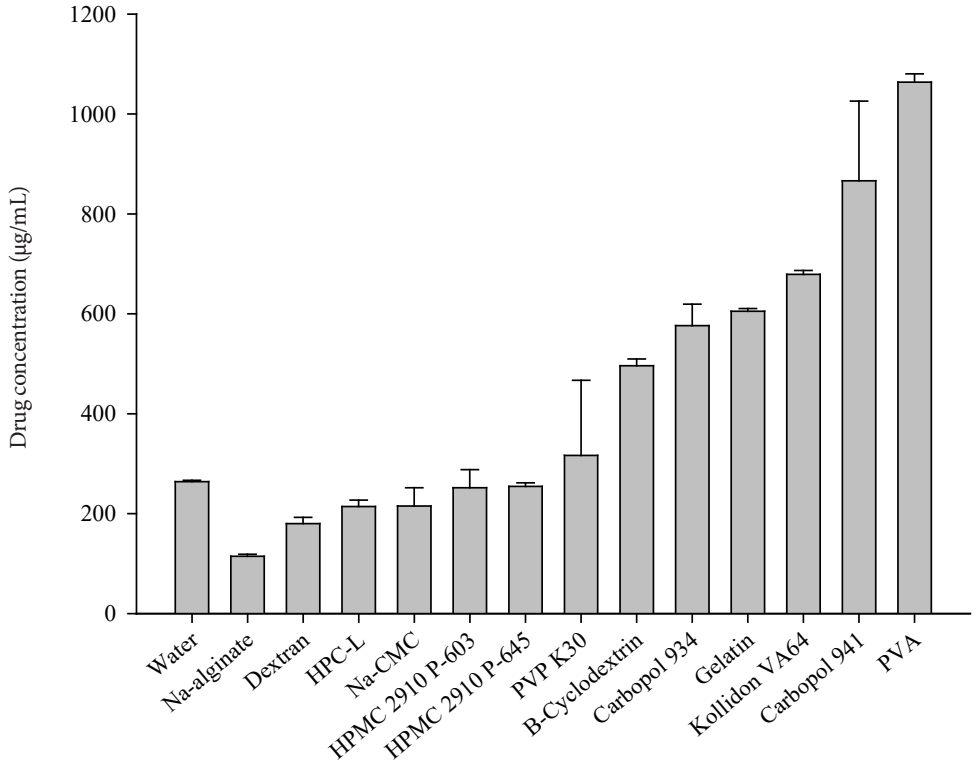

Fig. 2. Screening of polymer for enhancing silodosin solubility. Each value represents the mean ± S.D. (n=3).

리한 후 약물과 고분자 비율은 모두 1:1 (w/w)로 하여 3가지 형태(SA, SW, SE)의 고체분산체를 제조할 수 있었으며, 제조한 고체분산체는 Fig. 3과 같이 백색의 분말상으로 수득할 수 있었다.

3.2. 실로도신 고체분산체의 물리화학적 특성 평가

Table 2의 조성비로 제조된 3가지 고체분산체의 물리화학적 특성에 대해 평가를 진행하였다. 제조된 고체분산체의 함량을 분석한 결과 이론함량 대비하여 SA-SD는 105.6 %, SE-SD는 95.9 %로 고체분산체 조성에 비례한 실로도신 함량 값을 나타내었으나, SW-SD는 68.6 %로 SA, SE 고체분산체에 비해서는 낮은 실로도신 함량을 가진 것으로 확인되었다. 이는 SW-SD 제조 시 용매인 에탄올에 녹아 있는 실로도신이 용매에 녹지 않은 PVA에 비하여, 분말화로 수득 되지 못하고 상대적으로 많은 양이 용매와 함께 휘발되어 날아갔기 때문인 것으로 판단되었다.

Fig. 4는 주사 전자 현미경으로 실로도신과 그 고체분산체 및 PVA의 표면 형태학적 특성을 촬영한 결과이다. 실로도신 원료 약물은 약 5 μm 정도의 얇고 긴 바늘 모양의 결정형태를 가지고 있으며, 담체로 선정한 PVA는 50 μm이상의 입자부터 그보다 작은 입자들로 구성되며 불규칙한 모양으로 확인되었다.

SA-SD는 현탁 된 상태로 결정형을 유지한 실로도신에 정제수에 용해된 PVA가 분무건조 과정에서 실로도신 표면에 부착되어 실로도신 약물 분말의 원래 형태인 바늘에 코팅되어 있는 형태로 제조된 것으로 판단되었으며(Fig. 4, C, D), SW-SD의 경우 분무건조 과정에서 용해된 실로도신이 원래의 형태를 유지한 PVA의 표면에 부착되어 얇은 실처럼 가느다란 입자 형태로 부착되어 있는 것으로 확인되었다(Fig. 4, E, F). SE-SD의 경우는 실로도신과 PVA가 아세톤에/정제수 용액에 투명하게 용해된 후 분무건조되어 제조된 고체분산체이다. SE-SD의 형태를 SEM 촬영한 결과, 다른 두 고체분산체와 달리 구형에 가까운 형태로 제조되었다. 이는 침상의 결정형태인 실로도신이 PVA와 함께 용해된 상태인 용액을

Fig. 3. Appearance of silodosin-loaded solid dispersions: (A) silodosin, (B) surface-attached solid dispersion, (C) solvent-wetted solid dispersion, (D) solvent-evaporated solid dispersion.

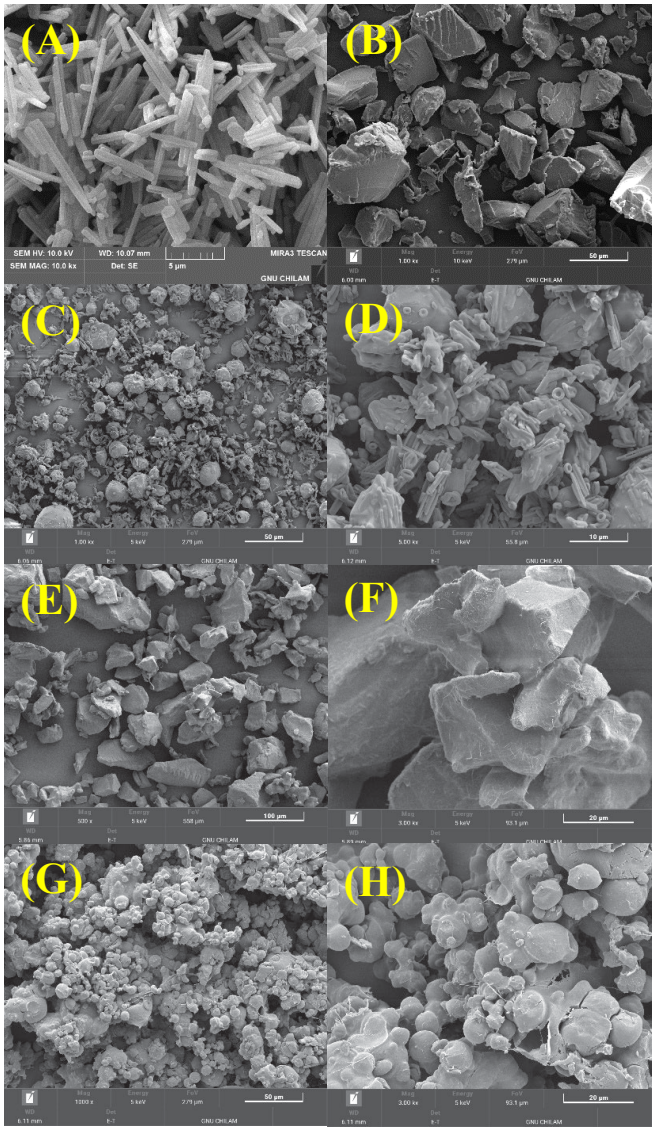

Fig. 4. Scanning electron microscope images: (A) silodosin-API (× 10,000), (B) polyvinyl alcohol (× 1,000), (C) surface-attached (× 1,000), (D) surface-attached (× 5,000), (E) solvent-wetted (× 500), (F) solvent wetted (× 3,000), (G) solvent-evaporated (× 1,000), (H) solvent-evaporated (× 3,000).

분무건조 함으로써 구형태의 미세액적에서 용매가 순간적으로 건조되어 제조된 형태인 것으로 사료되었다[20].

제조된 고체분산체들의 다형성(Polymorphism) 결정상태를 확인하기 위해 분말 X선 회절 패턴을 이용해 분석한 결과(Fig. 5), SEM촬영 시 실로도신의 결정 형태가 확인되었던 SA-SD의 경우 PXRD그래프에는 실로도신 약물이 가진 고유한 결정 피크를 유지하고 있는 것을 알 수 있었다. 실로도신의 형태가 완전히 사라진 SW-SD 및 구형태로 제조된 SE-SD의 PXRD그래프에서는 실로도신의 결정 특성을 나타내는 피크가 모두 사라진 것이 확인되었다. 이를 통해 이 두가지 고체분산체의 경우 실로도신이 무정형태로 만들어진 것으로 사료되었다.

실로도신과 PVA간의 분자간 상호작용을 확인하기 위해 FT-IR을 이용해 스펙트럼 변화를 분석하였다. 먼저 약물인 실로도신의 스펙트럼을 분석하였을 때 1655 cm^{-1}에서 C=O, 3340 cm-1에서 N-H stretching 및 3483m^{-1}에서 O-H stretching등의 주요 피크를 가지는 것으로 확인되었다(Fig. 6) [21]. 원료 약물이 가진 특정한 피크들은 고체분산체의 스펙트럼에서 3340 cm^{-1}의 N-H stretching, 3483m^{-1}의 O-H stretching피크가 완만해지는데, 이는 실로도신과 PVA 간의 수소 결합 상호작용에 따른 것으로 추측할 수 있었다. 무정형 고체분산체의 경우 발생하는 분자 간의 수소 결합이 결정성 약물 실로도신보다 더 강할 수 있으므로 N-H stretching, O-H stretching이 약화되어 PVA으로 추정되는 완만하고 넓은 피크가 나타난 것으로 사료되었다[22]. 제조된 고체분산체들은 모두 실로도신이 가진 특정 스펙트럼에 큰 변화를 나타내지는 않았지만, 결정형의 변화가 없었던 SA-SD가 약물인 실로도신과 가장 유사한 스펙트럼을 나타낸 것으로 사료되었다.

Fig. 7, Table 3의 실로도신 함유 고체분산체의 포화용해도 시험 결과와 Fig. 8의 동적 용해도 시험 결과에 따르면, 정제수에서의 포화용해도는 실로도신 약물(264.1 μg/mL)에 비하여 SA-SD(1099.6 μg/mL)는 약 4.2배, SW-SD(1593.4 μg/mL)는 약 6배, SE-SD(1975.4 μg/mL)는 약 7.5배 증가하였다. pH 6.8 용액의 경우에는 실로도신(1398.3 μg/mL)에 비하여 SA-SD(4181.8 μg/mL)는 약 3배, SW-SD(6537.8 μg/mL)는 4.7배, SE-SD(7246.9 μg/mL)는 약 5.2배 용해도가 증가하였다. 두 용액에서 모두 SA-SD, SW-SD, SE-SD순으로 SE-SD의 용해도가 가장 증가하였음을 알 수 있었다.

실로도신 원료약물 및 3종류의 고체분산체에 대한 동적 용해도 시험을 진행하였다. SA-SD는 정제수에서 실험 시 초기 10분 시점에 143.6 μg/mL으로 약물(9.7 μg/mL)대비 14.7배 상승되었으며, 60분에서 210.3 μg/mL 용해된 이후 용해도에 큰 변화를 보이지 않았다(Fig. 8A). pH 6.8용액에서는 더욱 천천히 용해가 되면서 초기 용해도는 실로도신 약물과 상당한 차이는 보이지 않았다. 120분에서 실로도신 약물 용해도 대비 1.8배(124.8 μg/mL vs 227.2 μg/mL) 향상되었으며 240분에서 271.0 μg/mL 용해되었다(Fig. 8B). 이는 SEM 결과와 PXRD결과로 확인 시, SA 고체분산체에는 약물의 결정형태를 유지하고 있기 때문에 상대적으로 천천히 용해되어 용해속도가 느릴 뿐만 아니라, 240분 시점에서도 다른 고체분산체보다 낮은 용해도를 보인 것으로 사료된다. SW-SD는 SE-SD와 상당히 동일한 용해도 증가 양상을 보였다. 정제수와 pH 6.8용액에서 모두 초반 10분에서 30분까지 급격하게 용해되다가 이후에는 서서히 용해도가 증가하는 현상을 관찰할 수 있었다. 정제수에서 SW-SD와 SE-SD는 120분까지 동일하게 용해되다가 180분에 SW-SD 301.6 μg/mL, SE-SD 328.6 μg/mL으로 SE-SD가 높아졌으며(Fig. 8A), pH 6.8 용액에서는 초반 10분부터 240분까지 모두 SW-SD보다 SE-SD가 더 개선된 용해능을 보인 것으로 사료되었다(Fig. 8B). 이는 SW-SD의 SEM과 PXRD결과로 확인했을 때 실

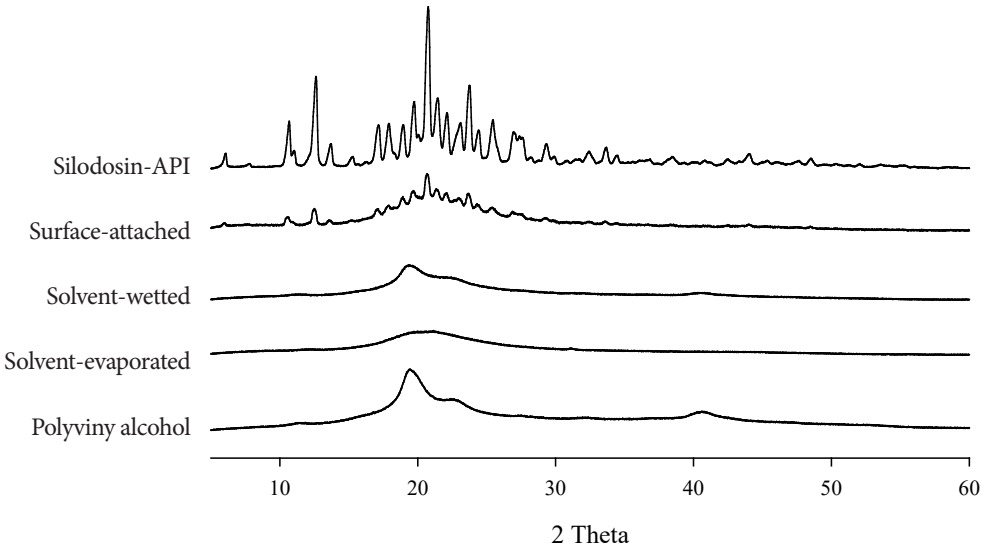

Fig. 5. Powder X-ray diffraction patterns of silodosin, solid dispersions and polyvinyl alcohol.

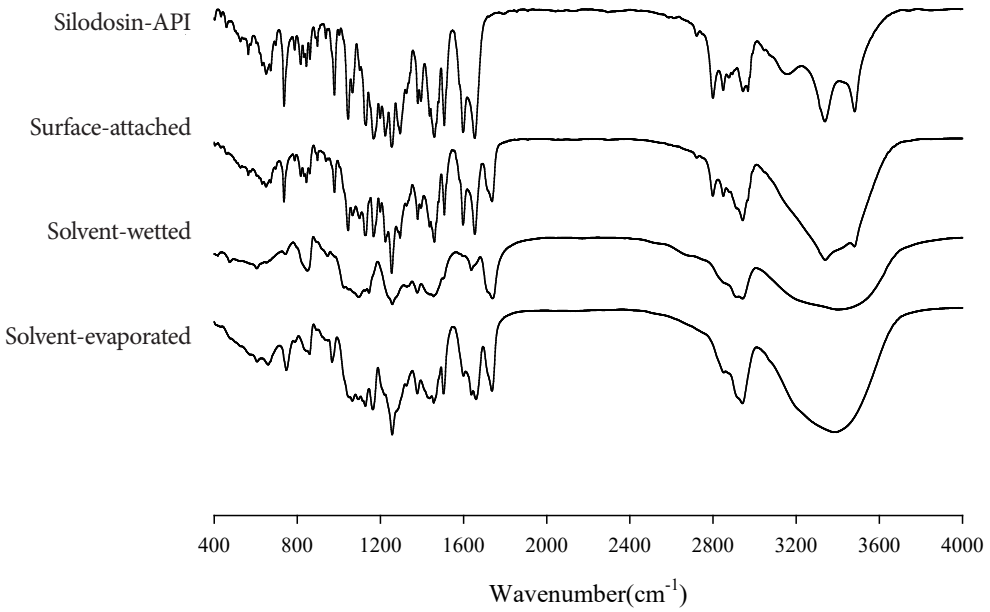

Fig. 6. Fourier transform infrared spectra of silodosin and solid dispersions.

로도신이 친수성 고분자 PVA표면에 실과 같은 가느다란 무정형으로 존재함으로써 원료에 비하여 용해도가 유의적으로 증가하였지만, SE-SD에 비하여 입자크기의 감소, 표면적 향상 및 용해도 향상을 위해 첨가한 고분자와 약물의 접촉면적이 적기 때문에 SE-SD보다 낮은 용해능을 가진 것으로 사료되었다. 최종시점인 240분 시점을 기준으로, 정제수에서 SA-SD는 226.4 μg/mL, SW-SD는 295.1 μg/mL, SE-SD는 325.1 μg/mL으로 실로도신 원료(108.8 μg/mL) 대비 2.1배, 2.7배, 3배 향상된 용해도를 보였으며 pH 6.8 용액에서는 SA-SD는 271.0 μg/mL, SW-SD 311.5 μg/mL, SE-SD 329.8 μg/mL으로 원료(134.7 μg/mL)와 비교하여 2배, 2.3배, 2.5배 향상됐으며, 정제수와 pH 6.8용액에서 모두 SE-SD, SW-SD, SA-SD 순으로 SE-SD가 가장 용해도가 개선되었다.

이와 같은 용해도 증가 현상은 FT-IR분석 결과 상, 실로도신과 PVA간의 수소 결합 상호작용과도 관련이 있을 것으로 사료되었다. FT-IR 분석에서 N-H stretching과 O-H stretching 피크의 완만해짐은 실로도신과 PVA 간의 강력한 수소 결합 상호작용을 나타내며, 이는 약물의 결정 구조를 무정형으로 변화시키는 주요 요인으로 판단하였다. 무정형 상태의 약물은 결정성 약물보다 더

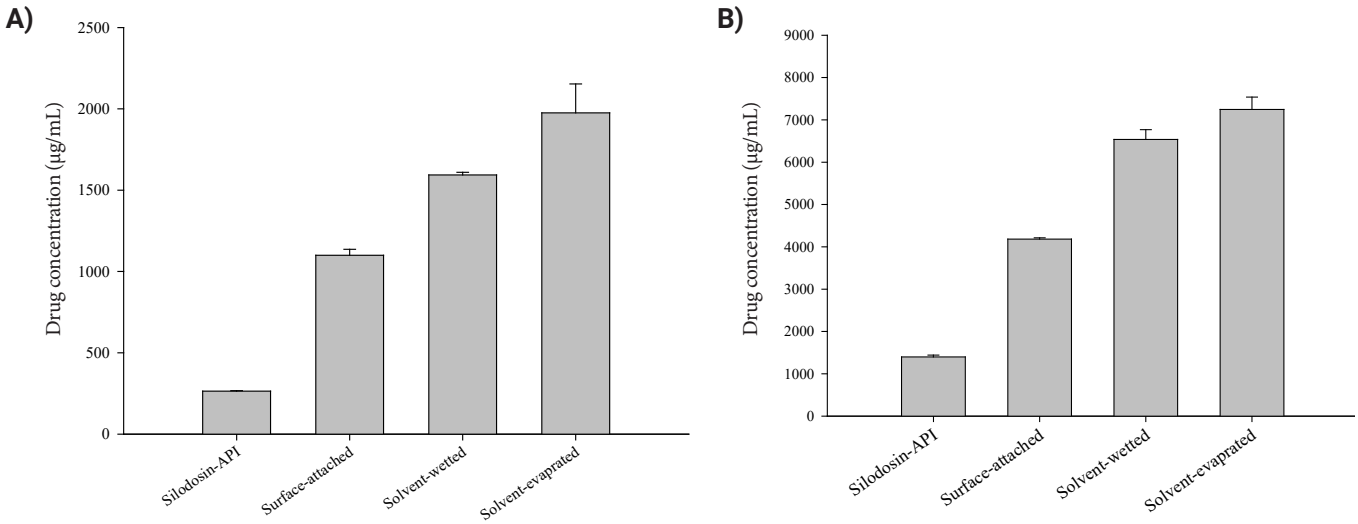

Fig. 7. Saturated solubility in (A) water and (B) pH 6.8 solution.

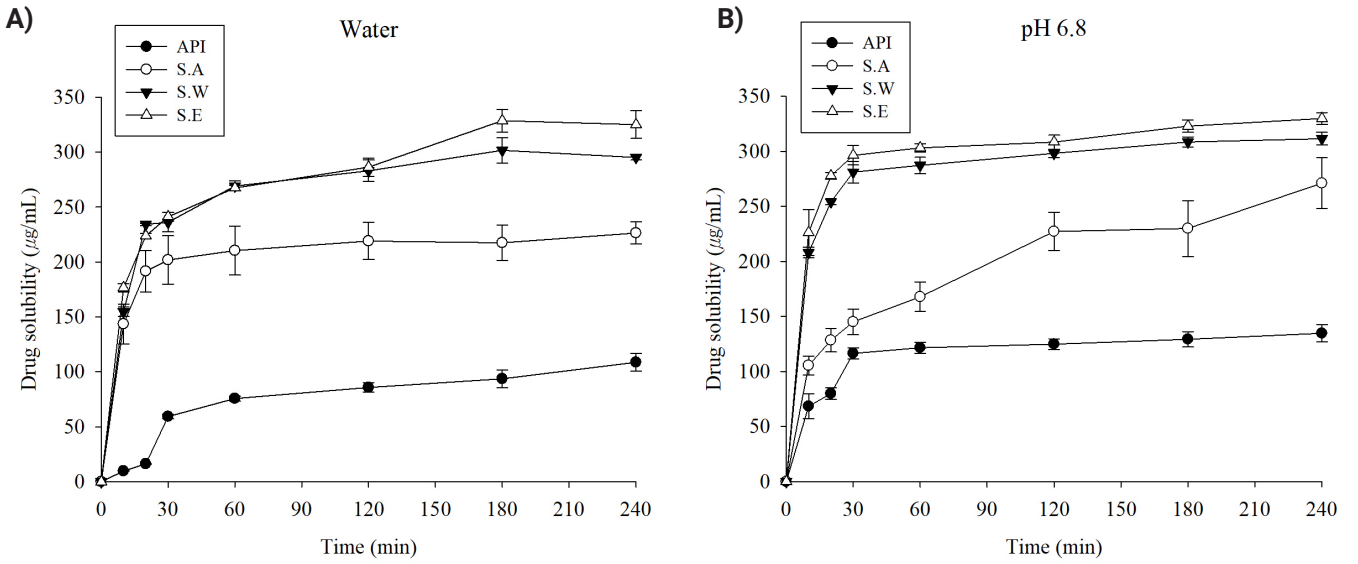

Fig. 8. Kinetic solubility in (A) water and (B) pH 6.8 solution.

Table 3. Solubility results in pH 6.8 solution and water.

	Concentration.(μg/mL)			
	Silodosin	SA-SD	SW-SD	SE-SD
	Mean ± SD	Mean ± SD	Mean ± SD	Mean ± SD
Water	264.1 ± 0.6	1099.6 ± 36.7	1593.4 ± 16.7	2059.9 ± 185.1
pH 6.8	1398.3 ± 42.7	4181.8 ± 32.2	6537.8 ± 230.7	7246.9 ± 292.2

높은 용해도를 가지므로, 이러한 구조 변화가 용해도 증가의 핵심으로 작용하였다. SW-SD와 SE-SD는 정제수와 pH 6.8 용액 모두에서 SA-SD보다 더 높은 용해도를 보였으며, 특히 SE-SD는 가장 높은 용해도를 나타냈다. 이는 FT-IR 분석에서 실로도신이 PVA와 강력한 수소 결합을 형성함으로 무정형 상태로 존재함을 시사하며, 무정형 상태로의 전이와 이에 따른 결정성 감소가 용해도 증가

에 크게 기여했음을 의미한다. 특히, SE-SD의 경우 입자 크기 감소와 표면적 증가로 인해 더 높은 용해도를 보였음으로 사료되었다.

4. Conclusion

본 연구에서는 다양한 고분자용액을 스크리닝하여 확인된 실로도신 용해도 향상능이 가장 우수한 고분자를 이용하여 세 가지 서로 다른 방법으로 제조한 실로도신 함유 고체분산체의 물리·화학적 특성 차이를 확인하여 보았다. 다양한 고분자 존재 하에 실로도신의 용해도 변화를 확인한 결과, 용해도 향상 값이 가장 우수한 PVA를 고분자로 선정하였으며, 실로도신과 PVA가 함유된 고체분산체를 분무건조기술을 이용하여 제조하였다. 표면부착(SA), 용매습윤(SW), 용매증발(SE)의 각기 다른 방법으로 제조된 고체분산체에 대하여 SEM을 통해 표면형태학적 특성을 확인했으며, PXRD를 통해 결정성을 확인하고, FT-IR을 이용해 제조된 고체분산체내 실로도신과 PVA 간 상호작용을 확인하였다. 최종적으로 포화용해도 시험 및 동적 용해도 시험을 진행하여 제조된 고체분산체의 용해도를 평가하였다. 제조된 고체분산체는 SE-SD, SW-SD, SA-SD 순으로 포화용해도가 향상되었으며, 동적 용해도 시험결과도 동일한 순서로 용해도 개선정도가 확인되었기 때문에, 세 가지 방법 중 용매증발(SE)법이 가장 우수한 가용화 기술임을 알 수 있었다. 따라서 이러한 고체분산체 제조방법을 이용한다면 공결정 형성, 염형성, 사이클로덱스트린 복합체화, SNEDDS 및 나노 파티클 방법보다 단순한 제조공정과 비용 효율적인 기술로서 실로도신 뿐만 아니라 다양한 난용성 약물의 생체이용률을 개선시킬 수 있을 것으로 판단되며, 이러한 가용화 기술이 환자의 복약 순응도가 개선된 경구 투여 제형의 개발에 활용될 수 있을 것으로 사료되었다.

Conflict of Interest Declaration

저자들은 이해상충관련 해당사항 없음을 선언합니다.

Author Information

이수만, 송다영: 학생, 김경수: 교수

Acknowledgement

이 연구는 2024년도 경상국립대학교 발전기금재단 재원으로 수행되었음.

References

[1] B. Chughtai, J. C. Forde, D. D. M. Thomas, L. Laor, T. Hossack, H. H. Woo, A. E. Te and S. A. Kaplan: Nat. Rev. Dis. Primers., **2** (2016) 1.
[2] M. Rossi and T. Roumeguère: Drug Des. Devel Ther., **4** (2010) 291.
[3] S. Dhiman, B. D. Kurmi and V. Asati: Sep. Sci. Plus, **6** (2023) 2200117.
[4] A. Alhayali, P. R. Vuddanda and S. Velaga: J. Drug Delivery Sci. Technol., **53** (2019) 101122.
[5] Y. N. Gavhane and A. V. Yadav: Saudi Pharm J., **20** (2012) 331.
[6] V. R. Vemula, V. Lagishetty and S. Lingala: Int. J. Pharm. Sci. Rev. Res., **5** (2010) 41.
[7] K. Sekiguchi and N. Obi: Chem. Pharm. Bull. (Tokyo), **9** (1961) 866.
[8] P. Pandi, R. Bulusu, N. Kommineni, W. Khan and M. Singh: Int. J. Pharm., **586** (2020) 119560.
[9] K. B. Mir and N. A. Khan: Int. J. Pharm. Sci. Res., **8** (2017) 2378.
[10] M. A. Alam, R. Ali, F.I. Al-Jenoobi and A. M. Al-Mohizea: Expert Opin. Drug Deliv., **9** (2012) 1419.
[11] Y.-J. Park, D.-H. Oh, Y.-D. Yan, Y.-G. Seo, S.-N. Lee, H.-G. Choi and C.-S. Yong: J. Pharm. Invest., **40** (2010) 97.
[12] E.-J. Kim, M.-K. Chun, J.-S. Jang, I.-H. Lee, K.-R. Lee and H.-K. Choi: Eur. J. Pharm. Biopharm., **64** (2006) 200.
[13] J.-S. Choi, S.-E. Lee, W.S. Jang, J.C. Byeon and J.-S. Park: Mater Sci Eng C., **90** (2018) 387.
[14] M.-J. Choi, M. R. Woo, K. Baek, J. H. Park, S. Joung, Y. S. Choi, H.-G. Choi and S. G. Jin: Mol. Pharmaceutics, **20** (2023) 4153.
[15] H. J. Choi and K. S. Kim: J. Life Sci., **31** (2021) 502.
[16] H.-J. Choi, J.-G. Lee and K.S. Kim: JKAIS, **22** (2021) 323.
[17] J.-G. Lee: Development of novel Enzalutamide tablet formulation With enhanced solubility and bioavailability, Graduate School of Gyeongsang National University, Jinju, (2022) 5.
[18] Y. Umemoto, S. Uchida, T. Yoshida, K. Shimada, H. Kojima, A. Takagi, S. Tanaka, Y. Kashiwagura and N. Namiki: J. Drug Delivery Sci. Technol., **55** (2020) 101401.
[19] R. Nagarkar and J. Patel: Acta Sci. Pharm. Sci., **3** (2019) 34.
[20] A. Paudel, Z. A. Worku, J. Meeus, S. Guns and G. Van den Mooter: Int. J. Pharm., **453** (2013) 253.
[21] B. Supriya, N. Babu, Padmavathi, Yenumula, B. Sai and G. Pavani: YMER, **21** (2021) 344.
[22] V. Tantishaiyakul, N. Kaewnopparat and S. Ingkataowornwong: Int. J. Pharm., **181** (1999) 143.

학 회 소 식

2024년도 학회 행사(2024.4.20. ~ 2024.6.19.)

2024년도 제3차 편집위원회 회의
일　　시 : 2024년 6월 11일(화) 오후 3시
장　　소 : 온라인
회의내용 : 분말재료학회지 발간의 건

2024년도 제3차 회장단 회의
일　　시 : 2024년 6월 13일(목) 오후 1시
장　　소 : 과학기술회관 중회의실5
회의내용 : ISNNM-2024 및 추계 준비의 건

2024년도 제3차 이사회의
일　　시 : 2024년 6월 13일(목) 오후 4시 30분
장　　소 : 과학기술회관 중회의실5
회의내용 : ISNNM-2024 및 추계 준비의 건

– 학회동정 –

◆ 한국분말재료학회지는 한국연구재단의 등재학술지입니다. (사)한국분말재료학회에서는 항상 회원님들의 논문을 투고받고 있사오니 많은 참여 바랍니다.
◆ (사)한국분말재료학회 홈페이지에서는 한국분말재료학회지 원문 서비스를 시행하고 있습니다. 로그인 후 한국분말재료학회지를 열람하실 수 있사오니 많은 이용 바랍니다.
◆ (사)한국분말재료학회 회원가입과 한국분말재료학회지에 논문을 투고하시는 것은 학회 홈페이지를 통해 이용 가능합니다.
◆ (사)한국분말재료학회 홈페이지(http://www.kpmi.or.kr/)의 많은 이용 바랍니다. 기타 문의사항은 이메일(kpmi@kpmi.or.kr) 또는 전화(☎02-539-4603)로 연락바랍니다.

특 / 별 / 회 / 원

K회원

신한다이아몬드공업㈜
(21635) 인천광역시 남동구 남동동로 375 (남동인더스파크 36B-10L)
Tel (032) 814-2211 / Fax (032) 814-1190
http://www.shinhandia.co.kr
E-mail : webmaster@shinhan.co.kr

다이아몬드공구제조

㈜창성
(21628) 인천광역시 남동구 승기천로 320 남동공단 11-9
Tel (032) 420-8700 / Fax (032) 812-8779
http://www.changsung.com
E-mail : cscsale@changsung.com
Metal Powders (금속분말), Clad Metal (클래드메탈)
Magnetic Powder Core (분말자성코아),
Conductive Paste (도전성페이스트)

㈜풍산홀딩스 창원사업장
(51544) 경남 창원시 성산구 공단로 670(성주동)
Tel (055) 239-0700 / Fax (055) 239-0800
http://www.poongsanhc.co.kr
E-mail: Webmaster@poongsan.co.kr
동제품 외

㈜아스플로
(16648) 경기도 수원시 권선구 산업로156번길 7
아스플로 기술연구소
Tel (031) 352-2301 / Fax (031) 352-2309
http://www.asflow.com
반도체 배관 부품, 가스제어시스템

용인전자(주)
(17015) 경기 용인시 기흥구 동백중앙로 16번길 16-4,
에이스동백타워 1동 1101호
TEL: (031) 332-4402

전장용 자성체류

P회원

대구텍㈜
(42936) 대구광역시 달성군 가창면 가창로 1040
Tel (053) 760-7114 / Fax (053) 768-8055
http://www.taegutec.co.kr
E-mail : ct_d_sales@taegutec.co.kr
텅스텐, 중합금제품, 세라믹 제품

대신강업주식회사
(44252) 울산광역시 북구 책골길 45
Tel (052) 287-6162~4 / Fax (052)287- 6165
http://www.dsgu.co.kr
E-mail : nabormj@hanmail.net
자동차용 각종 플랜지류 및 너트류 생산
공구강 및 특수강 판매 대리점

대한소결금속㈜
(42983) 대구광역시 달성군 논공읍 논공로87길 43
Tel (053) 610-0700 / Fax (053) 610-0701
http://www.iksm.co.kr
E-mail : master@iksm.co.kr
철계 소결 기계부품

케이제이알로이㈜
(40046) 경상북도 성주군 선남면 명관로 337-7
Tel (054) 933-5578 / Fax (054) 933-5523
http://www.kjalloy.com
E-mail : kjalloy@kjalloy.com
정밀금형소재, 단조/분말금형, 절삭공구소재

특 / 별 / 회 / 원

(주)코스글로벌
(52057) 경상남도 함안군 법수면 윤외공단길 68
Tel (055) 570-8500 / Fax (055) 570-8599
http://http://www.koswire.com

스테인레스 와이어, 스테인레스 와이어로프, 금속분말

하나에이엠티㈜
(28126) 충북 청주시 청원군 오창읍 각리 1길 75
TEL: (043) 211-0046
http://www.hanaamt.com
E-mail : davidkim@hanaamt.com

가스아토마이징 금속분말, 3D프린팅, Mg, Al, SUS, Ti

신생금속공업(주)
(15078)경기도 시흥시 마유로 238번길 113
TEL: (031) 499-3671~8 / FAX: (031) 499-3680
http://www.shinsaeng.co.kr
E-mail : sales@shinsoeny.co.kr

귀금속 전기접점, 저온 특수 용접봉, Flux

웰드인덕션
(22108) 인천광역시 남구 염전로 165번길 38-38 (도화동)
TEL: (032) 572-6100 / FAX: (032) 572-6101
https://induction.uriweb.kr/index
E-mail : worldhft@daum.net

고주파 산업 응용장치, 아토마이져, 진공 챔버, 합금제조 등

㈜씨이피테크
(07228) 서울특별시 영등포구 영신로 220,
케이엔케이디지털타워 208호
TEL: (02) 749-9346 / FAX: (02) 749-9347
http://www.ceptech.co.kr/

3D프린터, 3D 스캐너, 소프트웨어 등

(주)엠티아이지
(06058) 서울시 강남구 논현동 106-7 (언주로 712),
영진빌딩 5층 MTIG
TEL: (02) 540-3617 / FAX: (02) 540-3616

타이타늄, 플랜트(신소재)

아이에스시
(13217) 경기도 성남시 중원구 갈마치로 215, B동 6층
TEL: (031) 777-7675 / FAX : (031) 777-7699
https://kor.isc21.kr

반도체 테스트 솔루션

(주)코나솔
(31806) 충청남도 당진시 면천면 산업단지길 17-60
TEL : (041) 359-6600
http://www.millroll.com

분말야금 제품, 기계부품, 압연롤

(주)이엠엘
(16229) 경기도 수원시 영통구 창룡대로256번길 77, 4층 409호
(이의동, 에이스 광교타워3)
TEL : (031) 5186-6282 / FAX : (0504) 265-8507
http://www.eloiml.co.kr/

금속 분말, 증착용 타겟

이지캐스텍
(13595) 경기도 성남시 분당구 황새울로 224 청구블루빌 619호
TEL : (031) 726-2242
https://www.ezcastech.com

주조(열유동) 및 구조 해석

아토메탈테크코리아㈜
(10049) 경기도 김포시 양촌읍 황금4로 82
TEL : (031) 986-9988 / FAX : (031) 996-2456
http://www.attometal.com/
비정질 합금 파우더

(주)버추얼랩
(04773) 서울특별시 성동구 왕십리로 38, 홍성빌딩 6층
TEL : (02) 3293-0204
https://www.virtuallab.co.kr/

디지털 소재 연구개발 플랫폼

특 / 별 / 회 / 원

특 별 회 원

M회원

㈜강앤박메디컬
(28160) 충청북도 청주시 청원구 오창읍 중심상업2로 48(양청리) 중소기업청 T-팩토리 사무동 204호
Tel (070) 7702-9983
http://www.knpmedical.com

의료용 TiNi계 형상기억 소재

경원산업㈜
(15084) 경기도 시흥시 정왕동 희망공원로 241 (시화공단 2나 205호)
Tel (031) 498-3982 / Fax (031) 498-3987
http://www.kwfi.co.kr
E-mail : kwfi@kwfi.co.kr
K/SENSOR, 마그네트

로얄초경
(21690) 인천광역시 남동구 남동동로123번길 33 (공단95블럭 3롯트)
Tel (032) 814-3612 / Fax (032) 814-3616
http://www.royaltc.co.kr
E-mail : royaltc@royaltc.co.kr

초경합금, Heavy Alloy, W-Cu Alloy, 밀링인서트

㈜삼한
(51560) 경상남도 창원시 성산구 연덕로 84
Tel (055) 285-0041 / Fax (055) 282-0144
http://www.samhanltd.co.kr
E-mail : samhan@samhan.biz

자동차부품, Stainless 계열, 연자성 계열, 고강도 부품

알란텀㈜
(13229) 경기도 성남시 중원구 둔촌대로 400 (상대원동, 스타우드 프라자 8층)
Tel (031) 737-0991 / Fax (031) 737-0980
http://www.alantum.com/kr
E-mail : info@alantum.com
배기가스 후처리 기술, 화학 촉매 기술, 산업용 특수 제품

㈜에이피엠
(43013) 대구광역시 달성군 구지면 달성2차3로 60 (달성2차 산업단지 25B-3L)
Tel (053) 611-3101 / Fax (053) 611-3117
http://www.apmworld.co.kr
E-mail : administrator@apmworld.co.kr
오일리스베어링, 소결 기계 부품 , 금형

㈜엔젤
(46988) 부산광역시 사상구 새벽시장로 74 (감전동)
Tel (051) 326-3004 / Fax 051-322-7004
http://angel-juicer.com
E-mail : angeljuicer.web@gmail.com
전기녹즙기, 액추에이터, 모터

㈜유승
(50566) 경남 양산시 상북면 소토4길 34-1
Tel (055) 375-8856 / Fax (055) 375-8858
http://www.ysbiz.co.kr
E-mail : yuseung@ysbiz.co.kr
분말야금공정(자동화공정, 전자공정), 파이프공정

㈜이엔에프테크놀로지
(17084) 경기 용인시 기흥구 탑실로 35번길 14(공세동)
TEL: (031) 881-8200 / FAX: (031) 282-6855
http://www.enftech.com

Etchant, Stripper

이화다이아몬드공업㈜
(18145) 경기도 오산시 남부대로 374
Tel (031) 370-9000 / Fax (031) 370-9229
www.ehwadia.co.kr

다이아몬드공구제조

지멘스㈜
(37668) 경상북도 포항시 남구 지곡로 394 포항테크노파크 벤처3동 PLM XDCR
Tel (054) 223-2629
http://www.siemens.co.kr
E-mail : adscs.kr@siemens.com
의료기기, 터빈, 산업용 소프트웨어

㈜펨토바이오메드
(37673) 경상북도 포항시 남구 지곡동 청암로 77 포스텍 융합연구동 C5, 716
Tel (054) 221-6200 / Fax (054) 221-6209
http://www.smartdrop.co.kr
E-mail : office@femtobiomed.com
접촉각 측정기(Smart Drop)

특 / 별 / 회 / 원

한국분말야금㈜
(31435) 충청남도 아산시 인주면 인주산단로 111번지
Tel (041) 538-3800 / Fax (041) 538-3815
http://www.korpm.co.kr
E-mail : technical@korpm.co.kr
자동자 부품, 가전기기부품, 산업 기계용 부품 제조

한국야금㈜
(28589) 충청북도 청주시 흥덕구 산단로 55
Tel (043) 262-0141 / Fax (043) 262-0146
http://www.korloy.co.kr
E-mail : korloy@korloy.com
초경합금절삭공구(코팅, 써메트, 초경 등)

한국회가내스㈜
(06654) 서울특별시 서초구 서초중앙로 41 대성빌딩 13층
Tel (02) 511-4344 / Fax (02) 548-2592
http://www.hoganas.com/korea
E-mail : korea@hoganas.com

각종 분말야금용 철분말 등

존슨일렉트릭오퍼레이션스㈜
(28122) 충청북도 청주시 청원구 오창읍 과학산업5로 101
Tel (043) 241-7114 / Fax (043) 241-7119
http://www.hallastackpole.co.kr
E-mail : bkmoon@hallastackpole.co.kr
분말야금제품, 자동차부품

㈜KAMI
(08502) 서울특별시 금천구 가산디지털1로 196, 1005호
(가산동, 에이스테크노타워10차)
Tel (02) 6670-4114 / Fax (02) 6670-4110
http://kami.biz/kami/
E-mail : info@kami.biz
부품 개발 및 생산, 기술용역, 세라믹가공기, 다이아몬드 분말

KB오토시스㈜
(31443) 충남 아산시 음봉면 아산온천로 528-24
Tel (041) 537-5358 / Fax (041) 537-5110
https://www.kbautosys.com
E-mail : webmaster@kbautosys.com

자동차 브레이크 마찰재

승림전기(주)
(14569)경기도 부천시 조마루로385번길 72
Tel (031) 616-6336 / Fax (031) 616-6337
http://www.seunglimelec.com/
E-mail : sales@seunglimelec.com
전기차단기부품(전기접점) 제조, 전기회로 개폐, 보호 및 접속 장치

(주)MS가스
(18525) 경기도 화성시 비봉면 푸른들판로1010번길
127-32 (청요리428-39)
Tel (031) 8047-5051~3 / Fax (031) 8047-5055
http://www.msgas.co.kr
E-mail : inquiries@msgas.co.kr
고압가스 및 가스공급설비

에스엠비코퍼레이션
(10049) 경기도 김포시 양촌읍 학운산단2로 14
TEL : (031) 983-9030 / FAX : (031) 983-9031
http://www.smbcorp.co.kr

특수금속분야, 분말

㈜엠케이
(17794) 경기도 평택시 청북읍 고렴1길, 41-50
TEL : (031) 686-5490 / FAX : (031) 696-5490
https://www.mkmetal.co.kr

금속분말(분말야금용, 적층제조용, 기타)

(주)부강특수산업
(38899) 경상북도 영천시 본촌공단길 42
Tel : (054) 335-9996
http://www.bkcoalloy.co.kr/
내열/내마모/내부식 특수합금

(주)비에스지머티리얼즈
(14521) 경기도 부천시 옥산로214번길 21, 4층
Tel : (070)7537-2527

전기자동차 2차전지용 음극 활물질

Code of Ethics for the Journal of Powder

Journal of Powder Materials

Established: 2007. 10. 23

Full Text

First published in April 1994, with the purpose for the revitalization of technical exchange between Academics & Industry in Powder Metallurgy related advanced studies. Journal of Powder Materials is currently published on a bi-monthly basis.

The Korean Powder Metallurgy & Materials Institute has prepared a code of ethics for a qualitative improvement to its journal. We can therefore secure the ethics required for scientific research through this code of ethics; and we intend to raise the value of our journal through the addition of originality and integrity to our journal. Therefore, all authors of theses, review committee members and editorial committee members shall observe this code of ethics in order to reject any dishonesty in the publication of theses and secure the integrity of any research.

Chapter 1. Matters to be observed by the author of thesis

1. The criteria of the authorship

The Author of academic paper means a person who meets all of the following criteria for authorship (based on the criteria of International Committee of Medical Journal Editors). Those who are not satisfied with any of the following criteria shall be divided into “contributor”.

A. Substantial contributions to the conception or design of the work; or the acquisition, analysis, or interpretation of data for the work.

B. Drafting the work or revising it critically for important intellectual content.

C. Final approval of the version to be published.

D. Agreement to be accountable for all aspects of the work in ensuring that questions related to the accuracy or integrity of any part of the work are appropriately investigated and resolved.

2. The duty of the author

The author of thesis shall explain the results and discussions of the research which the author has performed in a concise and accurate manner. When submitting the research results to the Journal of Powder Materials, an author of a thesis shall observe the code of ethics of this institute and conform to the honesty, accuracy and integrity of the research result submitted as such.

A. When submitting a thesis to the Journal of Powder Materials, the author of a thesis shall abide to the code of ethics as outlined by the Journal of Powder Materials

B. The author of a thesis shall reject any fabrication or falsification of the results for conducting all activities including the proposal, planning and execution of the research activities.

C. Submittal or publishing the same result to more than one journal simultaneously shall be regarded as an act of cheating and as such shall be eradicated.

D. The author of a thesis shall not submit and publish research results which were already published to this Journal.

E. An act of submitting another researcher's results under his/her own name shall be deemed as unethical and unacceptable.

F. An author who has submitted a thesis shall obtain proper consent from all existing co-authors and shall not include any inappropriate authors to the thesis. Co-authors shall contribute to the research academically and share the responsibility and achievements for the results altogether, and in the case of administrative and financial support for research, such shall be advised to state details through an "Acknowledgement".

G. An author of thesis shall obtain approval from the person concerned in advance with regards to submission if required, and confirm that there will be no future disputes of agreements and ownership.

H. The author of the thesis shall observe the regulations as provided in relevant laws, norms and as stated in the code of ethics; and to internationally accepted principles of the entire process of research and submission. Also, the author of such thesis shall also secure universality including the respect of human rights, the observation of bioethics, and the preservation of biological diversity and protection

for environments.

I. In the case of an error discovered in a submitted thesis during the publication process, the author of such thesis shall be obligated to correct any mistakes or withdraw the thesis altogether.

Chapter 2. Matters to be observed by the reviewer

The journal reviewer shall review a submitted thesis in compliance with this code of ethics and provide advice in regards to the publication of such thesis to the editorial committee members.

A. The journal reviewer shall review a submitted thesis fairly and objectively under consistent standards regardless of ethnicity, gender, religion, educational environment or acquaintance of the author of thesis.

B. The journal reviewer shall be obligated to review a thesis requested for review faithfully within the set period as determined in the review regulations.

C. The journal reviewer shall not disclose the information of the research results acquired through the review process to any third party or misuse such information.

D. The journal reviewer shall respect the personality of the author of the thesis and value the independence of intellectual ability. The journal reviewer shall prepare an amicable and supplementary written opinion without making subjective evaluations and shall avoid hostile expressions.

E. The journal reviewer shall request the author of the thesis to modify any inappropriate quoted contents and lead the author to quote references correctly. Also, the journal reviewer shall strictly review the thesis to determine is such has any similarity with previous published manuscripts that were presented in other publications.

F. The journal reviewer shall be obligated to reject review in the case of having any connection with the submitted thesis. The journal reviewer shall promptly notify such fact to the editorial committee members to appoint another journal reviewer.

Chapter 3. Matters to be observed by the editorial committee member

The editorial committee member shall retain full responsibility and authority to carry out the procedures to approve or reject a submitted thesis for publication in the journal. Each editorial committee member shall cooperate with the journal reviewer and other editorial committee members shall observe and carry out the following items.

A. The editorial committee member shall fairly evaluate the intellectual level of a thesis as submitted by the author regardless of ethnicity, gender, religion, educational environment or acquaintance of the author of a thesis.

B. The editorial committee member shall not delay the screening of a submitted thesis intentionally and shall perform prompt measures accordingly.

C. The editorial committee member shall screen the submitted thesis objective based on consistent standards, and the editorial committee member shall assume full responsibility and obligation for the required procedures.

D. The editorial committee member shall not release information regarding the submitted thesis to the public and shall not use such information for his/her own research purposes.

E. The editorial committee member shall be obligated to supervise any unethical behavior in a thesis submitted to the journal, and take any necessary measures for any wrongful acts. In the case of an appeal for wrongful acts, the editorial committee member and the review committee shall be obligated to investigate such matters.

F. The editorial committee member shall be obligated to reject screening in the case where editorial committee has written the thesis, or such has any connection with the submitted thesis. Another editing committee member shall be appointed for the screening process.

Chapter 4. Activities of the review committee

A. Clarifying integrity and responsibility of the research results – In the case where cheating has occurred, including plagiarism, duplicated submission or inappropriate citation is suspected, an investigation shall be carried out based on the editorial committee members recommendation The author of such thesis shall be responsible for any cheating including plagiarism, fabrication and falsification and duplicated presentation of the result.

B. In the case where any cheating is suspected in the process of a thesis submission and review, the editorial committee member shall submit such to the review committee and

request the review committee to investigate such in private. The review committee shall then carry out an inspection in compliance with the following guidelines to ensure that no victim shall suffer in good faith.

1. The review committee shall observe "the principle of presumption of innocence" until such is proven to be a wrongful act.
2. The review committee shall begin and perform such inspection fairly and without discrimination in private circumstances.
3. The review committee shall prepare, arrange and store documents in regards to the investigation.
4. The review committee shall suspend all process in regards to the thesis publication.
5. The review committee shall carry out an investigation promptly to reduce any damages due to delay.

C. The review committee shall carry out an investigation promptly and fairly at the editorial committee member's request. The investigation shall notify, carry out and finish based on the following guidelines.

1. The review committee shall notify any beginning of an investigation to the person or organization concerned that is questionable for cheating and also inform such as to any postponing of the publication of such thesis until the investigation is complete.
2. The review committee shall provide an opportunity for explanation to the person or organization subject to investigation within 30 days of written notice.
3. The review committee shall acquire and investigate any internal records or other publications related with cheating.
4. In the case of unintended mistakes or errors, the review committee shall finish the investigation promptly.
5. In the case where cheating is discovered, the review committee shall supervise measures for such cheating. The review committee shall return the submitted thesis to the author, notify the Institute's guideline to the author, remove or publish the withdrawal of the thesis in the case where such was already published, and restrict the author's thesis publication for 3 years afterwards.
6. In the case of a duplicated submission and publication with a joint publisher, such actions shall be notified to the relevant publisher and handled in conjunction with the relevant publisher.
7. All cases and investigations carried out by the review committee shall be documented and stored. In cases where cheating is not apparent, the relevant document shall be sealed.

Supplementary Provision

1. This code of ethics shall be in effect from October 23, 2007.
2. This Revised code of ethics shall be in effect from March 6, 2020.
3. This Revised code of ethics shall be in effect from February 10, 2022.

Journal of Powder Materials Research Misconduct-Related Regulations

Journal of Powder Materials

Enacted: June 17, 2016

Chapter 1 General Provisions

1. Purpose

The purpose of this guide is to strengthen research ethics by setting the standards, operation, and discipline of research

2. Ethics Committee

① The ethics committee of The Korean Powder Metallurgy & Materials Institute will be formed to deliberate and decide on the regulations.

② The chair of the Research Ethics Committee shall be the Editor-in-chief of The Korean Powder Metallurgy & Materials Institute Committee. The chair convenes and presides over the Research Ethics Committee when the Editorial Committee proposes an issue as regards research misconduct.

③ The Research Ethics Committee shall consist of no more than five members. The committee members are appointed by the president of the society after the recommendation of the Editorial Committee.

Chapter 2 Research Misconduct

3. Subject of Research Misconduct

Research misconduct is directed to articles, documents, and data submitted or published to the Journal of Powder Materials.

4. Simultaneous Submission

Submitted papers may not be submitted to other domestic or foreign academic journals simultaneously, or as a duplicate, regardless of whether it is submitted beforehand or afterwards.

5. Duplicated Publication

① Dissertations published in other domestic or foreign academic journals may not be duplicated.

② When submitting a research report or a part of a doctoral or a master's thesis as it is, or if it is corrected or supplemented, the correct description must be clearly stated.

6. Plagiarism

① Plagiarism is the act of deliberate description of the content of academic ideas, opinions, expressions, and research results already published through all written media, including domestic or foreign journals, academic papers, research reports, master's or doctoral dissertations, books, magazines, and the internet without reference to the source.

② Plagiarism also applies when the researcher is the same as the author of the paper already published (self-plagiarism). However, it is not considered plagiarism if it describes widely used academic knowledge or research results without citation./td >

Forgery and Falsification Forgery or falsification involves the act of intentionally expressing, among others, numerical values and photographs of the data or results used in the research differently from the truth.

1. Forgery is the act of untruthful creation of false data or research results that do not exist.
2. Falsification refers to the act of artificial manipulation of research materials, equipment, processes, or distorting research contents or results by modifying or deleting data arbitrarily.

Chapter 3 Deliberation and Resolution Procedures

8. Judgment of Research Misconduct

① If there is a report on research misconduct within or outside the institute, the chair of the Editorial Committee must convene the committee to collect relevant data and confirm the credibility of the report.

② When the chair of the Editorial Committee confirms the authenticity of the report, he/she will submit the document of issue to the Research Ethics Committee.

③ The chair of the Research Ethics Committee gives the researcher an opportunity to document the proposed issues within two weeks in advance of the hearing..

④ The Research Ethics Committee shall make a unanimous

decision on whether there has been a case of research misconduct. If there is a disagreement between the two parties, it shall be decided by a vote of 3/5 of the attending committee members.

9. Discipline and Result Processing

① A person who violates research ethics shall be subject to and notified of a disciplinary action through the following measures:

1. Member expulsion
2. Prohibition of contributing to the Journal of Powder Metallurgy
3. If the article is published, the article will be deleted. Papers that are scheduled to be published cannot be published.
4. Relevant organizations will be notified of ethics violations.
5. Other disciplinary actions that are deemed necessary

② The content of the violated research ethics shall be posted on the homepage after a two-week protest period.

③ The contents of the disciplinary action in Items 2, 3, and 5 of Clause 1 shall be notified in the name of the editor-in-chief after the decision of the Research Ethics Committee. The contents of disciplinary action in Items

10. Objection

① A researcher who is judged for a research misconduct may file an objection only once within one month from the date of notification, if the decision of the Research Ethics Committee or the reason for misconduct is unreasonable.

② The Research Ethics Committee can review or revise the contents of the resolution by deliberating the validity of the objection.

Supplement

1. Amendment, Opening, and Closing of Regulations

This regulation may be amended, opened, or closed through the resolution of the Board of Directors.

2. Effective Date

1. This regulation shall be effective beginning on the date of the Board of Directors' approval (June 17, 2016).
2. This Revised code of ethics shall be in effect from February 10, 2022.

Written Oath of Observance of Research Ethics

Journal of Powder Materials

Article title: _____

_____

Author name: _____

To Editor-in-chief of the Journal of Powder Materials

I, as a contributor to the Journal of Powder Materials, hereby declare that I have abided by the following Code of Research Ethics of The Korean Powder Metallurgy & Materials Institute while writing this article.

1. I swear that I shall observe The Korean Powder Metallurgy & Materials Institute's Research Ethics Code and regulations related to research misconduct, and have written this article through honest and rigorous research.
2. I swear that I have not published this article elsewhere and have no plan to submit this article in other journals until the deliberation is over.
3. I swear that I have not committed any research misconducts that can be defined as a violation of Research Ethics, such as forgery (falsification), alteration, plagiarism, duplicate publication, etc., that compromises academic integrity.
4. I swear that I acknowledge the legitimate efforts of participating researchers and did not make unreasonable authorship of those who have not contributed to the research.
5. I swear that I shall take full responsibility for all problems and disadvantages that may arise from noncompliance with the Research Ethics if found guilty of any of the above-mentioned research misconducts.

All authors must sign this Written Oath of Observance of Research Ethics, but in case of necessity, the correspondent author can obtain the consent of other authors and replace them.

All Authors:

_____ _____

Signature Date Signature Date

_____ _____

Signature Date Signature Date

One author on behalf of all co-authors:
"I warrant that I am authorized to execute this copyright on behalf of all the authors of the article referred to above."

Instructions for authors

Journal of Powder Materials

The Korean Powder Metallurgy & Materials Institute, founded in 1994, is a research journal that primarily aims to publish original research papers on a bi-monthly basis.

1. Forms and contents of publication

- Original Papers: This form of publication represents original research articles on various aspects of powder metallurgy, namely fabrication, characterization, and forming of metal powders for advanced industrial applications.
- Letters or Rapid Communications: Short reports of original researches are accepted for publication.
- Critical Reviews or Reports : Invited or submitted review papers and technical reports are accepted.

The journal overall serves as a much-desired international platform for publications of wide researches in materials science. The emphasis, however, has been given on originality and quality of the paper rather than quantitative research. Short reports on material development, novel process or properties are also welcome. The following list of topics is of particular interest to the journal: (1) Powder fabrication techniques, (2) Characterization, (3) Compaction and sintering methods, (4) Heat treatment processes in powder metallurgy, (5) Industrial application of powders, (6) Powder process control, (7) Particle modification, (8) Particle motion and rheology, and (9) Particle growth.

2. Submission of papers

1) Manuscript should be submitted online at the KPMI homepage (http://www.kpmi.or.kr) or e-mail to the KPMI (journal@kpmi.or.kr)
2) File type: MS Word files according to instructions below. Pictures and photos should be submitted in JPG or TIFF format (300 dpi).
3) Prior to publications: Submitted manuscript must not previously been published in a journal and it is not being simultaneously considered for publication elsewhere.

3. Preparation of manuscripts

1) All papers should be written in English and SI units should be used throughout. Abbreviations should be defined the first time they occur in manuscript. Manuscripts should be typed on a paper of A4 format with 2.5 cm margins (right, left, top, bottom), and double-spaced, using Times Roman 11 font.

2) Structure of the manuscript:
The Title : The tile should be carefully chosen to indicate as clearly as possible the subject of the manuscript. The first letter of each word should begin with a capital letter except for articles, conjunctions, and preparations. The first word after a hyphen should also be capitalized such as "Variation of Magnetic Properties of Nd-Fe-B Sintered Magnets with Compaction Conditions".

Bylines should include all those who have made substantial contributions to the work. The first author should be the major contributor of the work. All authors' names should be written in full. At least one author should be designated with a sign as the corresponding author.

Affiliations should include the following information in the order of Institute, Department, City, Zip Code, and Country.

Abstract and Keywords : Each paper should include 120~200 words abstract and five key words for use in indexing.

3) Text: Description headings should be used to divide the paper into its component parts as below.

1. Introduction
2. Experimental
3. Results & Discussions
4. Conclusions

Acknowledgement (This is author's option.)
References
List of Table and Figure captions
Tables and Figures

4) References:
References should be indicated in the text by consecutive numbers in square parentheses, e.g. [1, 2, 5-7], as a part of the text, the full reference being cited at the end of the text. References should contain all the names of the authors together with their initials, the title of the journal, volume number (Bold type), year and the first page number as below. References to books should contain the names of the authors, the title (the names of

editors), the publisher name, location and year as below.

[1] J. D. James, B. Wilshire and D. Cleaver: Powder Metall., 33 (1990) 247.
[2] I. H. Moon: J. Korean Powder Metall. Inst., 1 (1991) 66.
[3] H. E. Exner and G. Petzow: Sintering and Catalysis, G. C. Kuczynski (Ed.), Plenum Press, New York (1976) 279.
[4] D. R. Dank and D. A. Koss: High Temperature Ordered Intermetallic Alloys, C. T. Liu (Ed.), MRS Symp. Proc. Vol. 133, Pittsburg, PA (1989) 561.
[5] Daido Steel: USA, US 5,193,607 (1993).
[6] M.G.Kim and J.H.Kim: Korea, KR 0041070 (2010).
[7] Germany: DIN EN ISO 11876N, Hardmetals.
[8] ASTM B213:03, Standard Test Method for Flow Rate of Metal Powders.
[9] J. C. Kim: M.S. Thesis, Title of Dissertation, Daehan University, Seoul (2011) 123.
[10] J. C. Kim: Ph. D. Dissertation, Title of Dissertation, Hankook University, Seoul (2011) 123.

5) Tables and Figures
Tables: type each table on the separate page, number consecutively in Arabic numerals and supply a heading. Figures for best results submit illustrations in the actual size (300 dpi) at which they should be published. The line drawings and the photographs should be originals and sharp images, with somewhat more contrast than is required in the printed version. Each figure should be typed on a separate page. The figure captions must be included.

6) Equations
Equations are placed must be clearly printed and numbered sequentially with Arabic numbers enclosed with round parentheses at the right-hand margin.

$$Ex)f = f\infty + (f0 - f\infty)\exp(-\gamma r/\gamma \tilde{} r) \quad (1)$$

4. Peer-review

All manuscripts are treated as confidential. They are peer-reviewed by at least 3 anonymous reviewers selected by the editor. Letters to the editor are reviewed and published on the decision of the editor. The corresponding author is notified as soon as possible of the editor's decision to accept, reject, or request revision of manuscripts. When the final revised manuscript is completely acceptable according to the KPMI format and criteria, it is scheduled for publication in the next available issue. Rejected papers will not be peer-reviewed again.

5. The accepted manuscript

1) Copyright:
Upon acceptance of a paper, the author(s) will be asked to transfer the copyright of the paper to the publisher, The Korean Powder Metallurgy & Materials Institute. This transfer will ensure the widest possible dissemination of the information.

2) Proofs:
Proofs will be sent to the corresponding author for checking before publication and will not be returned to the author, unless requested otherwise. Only typographical errors may be corrected. Any substantial alterations other than these may be charged to the author. All joint communications must indicate the name and full address of the author to whom proofs should be sent.

3) Reprints:
The authors are entitled to 50 reprints or a PDF file of the article without additional charge, but are charged for additional reprints exceeding 50 in addition to the nominal publication charge.

4) Publication charge:
The publication fee is US$200 up to 6 pages, and US$30 per additional page regardless of a member or a non-member. Additional fee for acknoledgement is US $100. For color printings, US$100 per color page is charged to authors regardless of the membership.

6. Code of ethics

We can secure the ethics required for scientific research through this code of ethics; and we intend to raise the value of our journal through the addition of originality and integrity to our journal. Therefore, all authors of theses, review committee members and editorial committee members shall observe this code of ethics in order to reject any dishonesty in the publication of theses and secure the integrity of any research. For the policies on the research and publication ethics not stated in this instructions, International standards for editors and authors (http://publicationethics.org/international-standards-editors-and-authors) can be applied.

Copyright transfer agreement

Journal of Powder Materials

Article No: _____

Article Title: _____

_____

By: _____

It is hereby agreed that the copyright of the above article is transferred to The Korean Powder Metallurgy & Materials Institute. However, the author(s) reserves the following:

1. All proprietary rights other than copyright, such as patent rights.
2. The right to reuse all or part of this article in other works.
3. The right to use the article for the author's personal use provided the copies are not offered for sale.

All Authors:

_____ _____

Signature Date Signature Date

_____ _____

Signature Date Signature Date

One author on behalf of all co-authors:

"I warrant that I am authorized to execute this copyright on behalf of all the authors of the article referred to above."

signaturedate signaturedate

_____ _____

Signature Date Signature Date

This document must be signed by author(s) and be received by the production office before the article can be processed for publication. Please mail this document to the following address:

The Korean Powder Metallurgy & Materials Institute

Unit 706, (635-4, Yeoksam-Dong) 22, 7Gil,Teheran-Ro, Gangnam-Gu, 135-703 Seoul, Korea

Checklist

Journal of
Powder Materials

☐ 제목과 저자명, 저자 소속을 정확하게 확인하였습니다.

☐ 교신저자를 기호로 구분되어 표기하였으며, E-mail 주소와 연락처를 정확하게 표기하였습니다.

☐ Keyword는 학회지에 규정한 Keyword list에서 선정하여 정확하게 확인하였습니다.

☐ 그림과 그림설명이 잘 매치 되었는지 정확하게 확인하였습니다.

☐ 참고문헌은 한국분말재료학회지 작성 규정에 따라 정확하게 작성되었습니다.

☐ The paper title, authors' names, and authors' affiliations have been confirmed to be accurate.

☐ The corresponding author has been distinguished using symbol(s), and e-mail address(es) and contact number(s) have been indicated accurately.

☐ The keywords have been selected from the keyword list determined by the Journal and confirmed to be accurate.

☐ The figures and their captions have been confirmed to be matched accurately.

☐ The reference materials have been drawn up accurately according to the paper guidelines of the Journal of Powder Materials.

2024년도 임원명단

Journal of Powder Materials

직 위	성 명	소 속
회장	김택수	한국생산기술연구원
수석부회장	김진천	울산대학교
대외협력부회장	이기안	인하대학교
학술부회장	이정구	한국재료연구원
기술부회장	홍순직	공주대학교
산업체부회장	이병윤	㈜창성
감사	김정곤	인천대학교
	장시영	한국항공대학교
편집위원장	김경태	한국재료연구원
편집이사	김정한	한밭대학교
	박귀일	경북대학교
	양민호	단국대학교
	이석재	전북대학교
	최현주	국민대학교
편집간사	강정신	서울대학교
	김정준	고등기술연구원
	박정민	한국재료연구원
	박태주	한양대학교
	배재웅	국립부경대학교
	변종민	서울과학기술대학교
	손석수	고려대학교
	신세은	순천대학교
	안창의	한국세라믹기술원
	양승민	한국생산기술연구원
	이 빈	경희대학교
	이동주	충북대학교
	조승기	한국재료연구원
	최병준	서울과학기술대학교
학술이사	강석훈	한국원자력연구원
	공만식	고등기술연구원
	노기민	한국지질자원연구원
	류호진	KAIST
	백연경	한국재료연구원
	이재범	충남대학교
	임효령	국립부경대학교
	채홍준	고등기술연구원
학술간사	김용주	국민대학교
	이지운	공주대학교
	정다운	한국생산기술연구원
	주수현	단국대학교

직 위	성 명	소 속
국제위원장	이창규	한국원자력연구원
국제이사	김범성	한국생산기술연구원
	류성수	한국세라믹기술원
	안병민	아주대학교
	이근재	단국대학교
	이정구	울산대학교
국제간사	성효경	국민대학교
기술이사	김세훈	한국자동차연구원
	김영무	국방과학연구소
	박지환	엠티아이지
	윤중열	한국재료연구원
	이성희	목포대학교
	최한신	지아이텍
	황병철	서울과학기술대학교
기술간사	김연철	이화다이아몬드공업㈜
	김지원	고등기술연구원
	김충수	한국생산기술연구원
	정효연	한국생산기술연구원
	차희령	한국재료연구원
대외협력이사	강민철	3D프린팅연구조합
	박만호	㈜아스플로
	박진경	LG이노텍
	송인혁	한국재료연구원
	이찬기	고등기술연구원
	천영범	한국원자력연구원
	홍현선	성신여자대학교
대외협력간사	김영균	한국재료연구원
	이동근	순천대학교
	한준희	한국생산기술연구원
지역이사 (지부장)	권세훈	경상지부장 : 부산대학교
	김경훈	강원지부장 : 한국생산기술연구원
	오익현	호남지부장 : 전남테크노파크
	이진규	충청지부장 : 공주대학교
	현승균	경인지부장 : 인하대학교
지역간사	고원석	경인지부 : 인하대학교
	김태훈	호남지부 : 전남대학교
	양승민	강원지부 : 한국생산기술연구원
	엄두승	제주지부 : 제주대학교
총무이사	박경태	한국생산기술연구원
	이영인	서울과학기술대학교
총무간사	김태훈	한국재료연구원
	이 빈	경희대학교
	최상훈	고등기술연구원
	최현주	국민대학교
재무이사	변종민	서울과학기술대학교
	양상선	한국재료연구원
재무간사	송명석	한국생산기술연구원
	정재원	한국재료연구원

제 16 대 평의원 명단

성 명	소 속	성 명	소 속	성 명	소 속
강 철	한라스택폴㈜	박귀일	경북대학교	이규수	MS가스
강두홍	(주)아스플로	박기봉	㈜엠케이	이근재	단국대학교
강민철	3D프린팅연구조합	박동규	경상대학교	이기안	인하대학교
강석중	KAIST	박만호	㈜아스플로	이동주	충북대학교
강석훈	한국원자력연구원	박성진	포스코홀딩스	이민하	한국생산기술연구원
고원석	인하대학교	박원욱	인제대학교	이민호	버추얼랩
공만식	고등기술연구원	박은수	서울대학교	이병윤	(주)창성
구용모	㈜창성	박은수	㈜이엠엘	이상관	한국재료연구원
권세훈	부산대학교	박정민	한국재료연구원	이석재	전북대학교
권영순	울산대학교	박정환	대광소결금속	이선영	한양대학교
권영태	한국재료연구원	박정효	국방과학연구소	이성모	HD현대중공업
김 폴	코오롱 미래기술원	박종관	㈜삼한	이성희	국립목포대학교
김경태	한국재료연구원	박지환	MTIG	이영인	서울과학기술대학교
김경훈	한국생산기술연구원	박진경	LG이노텍	이완재	한양대학교
김기범	세종대학교	박희동	이화다이아몬드공업㈜	이원식	한국생산기술연구원
김기한	용인전자(주)	백연경	한국재료연구원	이재범	충남대학교
김대현	(주)풍산홀딩스	백운형	한국전자재료	이재성	한양대학교
김덕주	하나테크	변종민	서울과학기술대학교	이정구	한국재료연구원
김동환	(주)성림첨단산업	석명진	강원대학교	이정구	울산대학교
김득중	성균관대학교	설재복	경상국립대학교	이지운	공주대학교
김범성	한국생산기술연구원	성효경	국민대학교	이진규	공주대학교
김병기	자화전자	손석수	고려대학교	이찬기	고등기술연구원
김상훈	산업연구원	손인진	전북대학교	이창규	한국원자력연구원
김세훈	한국자동차연구원	손현택	한국생산기술연구원	이학성	동아대학교
김신경	신한다이아몬드공업㈜	송광호	한국분말야금㈜	임경묵	한국생산기술연구원
김양도	부산대학교	송승철	한국회가내스㈜	임중경	대신강업주식회사
김영도	한양대학교	송용설	(주)아모그린텍	임효령	국립부경대학교
김영립	KAMI㈜	송인혁	한국재료연구원	장시영	한국항공대학교
김영무	국방과학연구소	신 훈	㈜아이피티	장태석	선문대학교
김용진	한국재료연구원	신광섭	일진다이아몬드공업㈜	정영근	부산대학교
김우종	(주)대건테크	신세은	순천대학교	정임두	울산과학기술원
김정곤	인천대학교	안동길	대구텍㈜	정재원	한국재료연구원
김정기	경상국립대학교	안병민	아주대학교	정형식	아주대학교
김정한	한밭대학교	안상호	포항산업과학연구원	조권구	경상국립대학교
김종렬	한양대학교	안인섭	경상국립대학교	조승기	한국재료연구원
김주용	리프로텍	안중호	안동대학교	조영철	현대자동차
김지순	울산대학교	안창의	한국세라믹기술원	좌용호	한양대학교
김진천	울산대학교	양동열	한국재료연구원	채홍준	고등기술연구원
김충수	한국생산기술연구원	양민호	단국대학교	천병선	충남대학교
김태규	한국원자력연구원	양상선	한국재료연구원	천영범	한국원자력연구원
김태훈	한국재료연구원	양승민	한국생산기술연구원	최병준	서울과학기술대학교

성 명	소 속	성 명	소 속	성 명	소 속
김택수	한국생산기술연구원	오승탁	서울과학기술대학교	최준필	한국기계연구원
김형섭	포항공과대학교	오왕근	(주)양우메탈	최한신	지아이텍
김홍물	하나에이엠티	오익현	전남테크노파크	최현규	현대제철
김효섭	한국생산기술연구원	유봉영	한양대학교	최현주	국민대학교
김휘준	한국생산기술연구원	유지훈	한국재료연구원	한유동	한국재료연구원
김희수	월드인덕션	윤덕용	KAIST	현승균	인하대학교
노기민	한국지질자원연구원	윤준철	현대제철	홍순직	공주대학교
류성수	한국세라믹기술원	윤중열	한국재료연구원	홍순형	KAIST
류시완	㈜풍산홀딩스	윤태식	대신강업㈜	홍현선	성신여자대학교
류호진	KAIST	은광용	㈜기술과가치	황득규	현대모비스㈜
박 준	제이피씨㈜	이 빈	경희대학교	황병철	서울과학기술대학교
박경태	한국생산기술연구원	이 성	국방과학연구소 민군협력진흥원		

본 학회지는 한국연구재단의 평가결과 등재학술지로 선정되었습니다.

"본 사업은 기획재정부의 복권기금 및 과학기술정보통신부의 과학기술진흥기금으로 추진되어 사회적 가치 실현과 국가 과학기술 발전에 기여합니다."